MODELLING AND CONTROL OF FEED DRIVES

by

KENNETH NG

B. A. Sc. (Engineering Physics)

University of British Columbia, Canada

A THESIS SUMBITTED IN PARTIAL FULFILLMENT OF

THE REQUIREMENTS FOR THE DEGREE OF

MASTER OF APPLIED SCIENCE

in

The Faculty of Graduate Studies

(Mechanical Engineering)

THE UNIVERSITY OF BRITISH COLUMBIA

(Vancouver)

August 2011

Abstract

Feed drives are used in positioning of machine tools. The drives are actuated either by linear or rotary servo motors. The ball screw drives are driven by rotary motors; hence they have flexibility and added friction due to nut interface. Direct drives are driven by linear motors which have more mechanical stiffness, but less disturbance rejection due to missing load reduction mechanism. This thesis presents the modelling and control of drives with rigid and flexible structures.

A single degree of freedom flexible oscillator is mounted on a high speed, rigid feed drive table for experimental illustration of system identification and the active control method proposed in the thesis. The rigid feed drive dynamics include the mechanical component of the rigid body mass and viscous damping, and the electrical component of the power amplifier and motor. The flexible component is modelled by springs, mass and damping elements. Both rigid and flexible dynamics of the system are identified experimentally through unbiased least square, sine sweep and impact model tests. The vibration of the single degree of freedom system is actively damped by an acceleration feedback inserted in the velocity loop. A Kalman filter is used to minimize the drift and noise on the acceleration measurements. The position loop is closed with a proportional controller.

It is experimentally demonstrated that the vibrations of the flexible structure can be well damped. However, the acceleration feedback used at the resonance frequency greatly minimizes the bandwidth close to the vibration frequency. Further methods need to be used to expand the bandwidth beyond the natural frequency of the flexible structure by coping with the anti-resonant effect of the acceleration feedback.

Table of Contents

List of Tables

List of Figures

Nomenclature

List of Symbols

A State Space Model Dynamics Matrix

B State Space Model Input Matrix

b Viscous Damping

C State Space Model Output Matrix

CE System Characteristic Equation

D Feed Through Matrix

d_f Disturbance Force Converted to Voltage Equivalent (V)

E Expected Value Computation

F_c Cutting Force (N)

F_d Disturbance Force (N)

F_t Motor Force (N)

I Identity Matrix

K Pole Placement Controller Parameters

K_1 First Gain Parameter to be Identified through NLS Optimization

K_2 Second Gain Parameters to be Identified through NLS Optimization

K_t Motor Force Constant (N/A) or Motor Torque Constant (Nm/A)

K_a Amplifier Gain Constant (A/V)

K_i Integral Gain

K_u Gain Scaling in Unbiased LS Optimization

K_v Motor Gain per Motor Mass in Continuous Time Domain

K_{vd}	Motor Gain per Motor Mass in Discrete Time Domain
k	Discrete Time Step
k_2	Oscillator Stiffness (N/m)
m_a	Oscillator Mass (kg)
m_t	Motor Mass (kg)
N	Number of Measurements
N_r	Reference Gain
NV	Negative Velocity Function
O	Observerability Matrix
$OS\%$	Percentage of Overshoot
PV	Positive Velocity Function
Q	Process Noise Covariance
p	Motor Pole
P_v	Viscous Friction per Motor Mass in Continuous Time Domain
P_{vd}	Viscous Friction per Motor Mass in Discrete Time Domain
s	Laplace/Continuous Time Domain Transfer Function
T_{peak}	Peak Time (sec)
T_s	Sample Time (sec)
T_{set}	Settling Time (sec)
V_{in}	Voltage Input (V)
X	State Vector
X_1	Motor State Vector
x_1	Motor Position (m)

x_2	Oscillator Position (m)
$\ddot{x}_2$	Oscillator Acceleration (m/sec^2)
R	Measurement Noise Covariance
R_w	Process Noise Matrix
R_v	Measurement Noise Matrix
r	Reference Input
u	Control Input
V	Cost Function in ULS Optimization
Y	Output Vector in ULS Optimization
y	State Space Model Output
z	Discrete Time Transfer Function
α	Equation Coefficient
ζ	Damping Ratio
σ	Sigma Function
θ	Parameters to be Identified in ULS Optimization
μ	Coulomb Friction
μ_k	Coulomb Friction Average
Φ	Regressor Matrix in ULS Optimization
ω_0	Resonant Frequency
ω_n	Natural Frequency

List of Scripts

1	Motor Parameters
2	Oscillator Parameters
d	Parameters to be Identified through NLS Optimization
i	Integral State
$k+1|k$	a prori state
$k|k$	a posteri state
m	Measurement Update Process
n	New Parameters (MS)
s	System Parameters (SS)
s	Laplace/Continuous Time Domain (MS)
sd	Desired System
ss	Steady State
T	Matrix Transpose Operation
t	Time Update Process
o	Observer
o	Desired Observer
z	Discrete Time Domain State (MS)

List of Notation

//	Parallel Configuration
+	Positive Direction
-	Negative Direction
^	Estimated State
~	Error State

List of Abbreviations

611U   Siemens SIMODRIVE 611 Universal Module, Control Motor Driver

CEL   Control Engineering Laboratory

CNC   Computer Numerical Control

FRF   Frequency Response Function

DS1103   dSPACE DS1103 Single Board Hardware PPC Controller Board

DC   Direct Current

LHS   Left Hand Side

LS   Least Square

MAL   Manufacturing Automation Laboratory

MS   Matrix State

MU   Measurement Update

NLS   Nonlinear Least Square

NLT   Negative Loop Transmission

PC   Personal Computer

RHS   Right Hand Side

SDOF   Single Degree of Freedom

SS   Scalar State

TF   Transfer Function

TU   Time Update

Acknowledgments

I wish to express my sincere gratitude to my research supervisors Dr. Yusuf Altintas and Dr. Ryozo Nagamune for their valuable instruction, guidance and support which they have provided throughout my research and coursework. I truly appreciate the great opportunity that they have offered me with. Working on this research project is a valuable experience. I am able to make practical uses of the knowledge that I have learned in class and further strengthen my understanding in the subject.

I also like to thank all members of the Manufacturing Automation Lab, especially to Ehsan Azadi Yazdi, Shixun Fan, Xiaoliang Jin, Anthony Siu and Bernhard Nimmervoll. They made their help available and provided me with many technical advices throughout my research work. Their contributions made the completion of this research work successful.

Finally, I want to acknowledge Natural Science and Engineering Research Council of Canadian Network for Research and Innovation in Machining Technology (NSERC CANRIMT) for sponsoring this research work.

Chapter 1.   Introduction

Precision positioning of tables in machine tools and other servo driven machines is essential for accurate production of parts or measurement of objects using computer control technology. When the mechanical structure of the drive is excited due to high accelerations and disturbance forces, it vibrates, leaving poor surface finish or incorrect measurements. This thesis presents modelling and position control of feed drives with rigid and flexible structures. The application of the proposed methods are rather wide, and can be found in machine tools, material handling, printing and assembly operations.

The thesis covers the system modelling, parameter identification, positioning control techniques of a feed drive and active vibration control on a flexible feed drive. The flowchart shown in Figure 1.1 provides an overview of the implementation work. In Chapter 2, a literature survey of past researches on vibration control is presented. Chapter 3 provides the overview of the real time control system implementation and instrumentation, and the experimental setup. A theoretical model and transfer functions of a flexible feed drive system are presented in Chapter 4. Different approaches including an ad-hoc technique, unbiased linear least square technique, impact modal technique, and sine sweep technique with NLS optimization are applied to identify the system parameters in order to select a most suitable model to represent the actual system. Chapter 5 explains the approach to design a position controller through the pole placement technique and a vibration control strategy to suppress the vibrations on the flexible drive. This thesis is concluded in Chapter 6 with a summary of work implemented and recommended future work.

Chapter 3: Experimental Setup

Chapter 4.2: System Modelling

Chapter 4.3: Parameters Identification

Chapter 5.2: Positioning Controller Design

Chapter 5.3: Active Vibration Controller Design
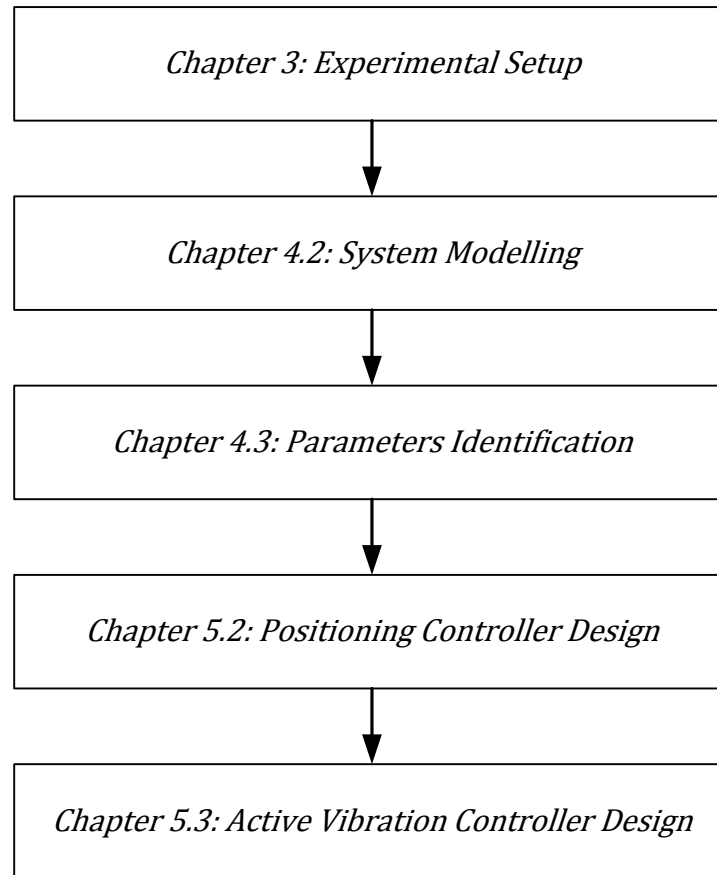
Figure 1.1: Implementation Work Flowchart

Chapter 2.   Literature Survey

2.1   Chapter Overview

The focus of this chapter is to review some of the past work by other researchers, which bear the relevance to the areas addressed in this thesis. Section 2.2 reviews the modelling and identification of flexible feed drives, which includes the components of the motor drive and the flexible structure. The detailed technical explanations of the modelling and identification methods published in the literature are presented in Chapter 4. In Section 2.3, the literature on various vibration control strategies are presented.

2.2   Identification of Drive Dynamics

Under the increasing demand for more accurate high performance motion systems, numerous system identification techniques appropriate for control purpose of mechanical systems have been proposed in the literatures. Erkorkmaz et al. [2] proposed the use of unbiased estimation of inertia and viscous friction in feed drives. This approach uses the least squares estimation method, and takes account for the presence of Coulomb friction in its formulation. The results from this estimation process are the estimated values for the combined inertia, viscous friction, and dynamic Coulomb friction of the system. In comparison to the simple least square technique, the unbiased least square technique should be more accurate.

The other useful dynamics identification approaches suggested by Altintas [1] include the sine sweep and impact modal testing techniques. The sine sweep technique is conducted to excite the system by commanding the open loop feed drive with a sinusoidal input over a wide frequency band containing the system natural modes. The ratio of the structure displacement/acceleration and the exerted force magnitudes, and the phase of the structure displacement/acceleration relative to the force are measured at each frequency. Then the measurements are processed through a parametric fit

algorithm for modal analysis. While sine sweep technique can deliver excitation force at desired frequency and amplitude, this approach is more time consuming to set up. Alternatively, an impact hammer can be used in exciting the system structure. The impact hammer for modal testing is much easier and quicker to set up, but at the expense of the possible less accurate excitation of the system structure at the desired frequency [1]. For the impact modal testing, the impact force delivered by the hammer can excite a wide frequency range, which contains the system natural modes. The hammer excitation force and resulting vibrations are measured in time domain. Then the measurements are transformed into Fourier domain for modal analysis which is commonly done in modal analysis software. For a comprehensive analysis of the system, all the discussed system identification techniques are applied. The detailed experimental procedures of the different techniques are explained and demonstrated in Chapter 4.

2.3   Vibration Control

There are many different vibration control approaches available in the literatures. Vibration control can be broadly divided into two general streams, reference command shaping and active control. Command shaping is a control technique in CNC machines which works by creating a command signal that avoids exciting the system structure natural frequency in order to minimize the vibrations or creates a command signal that cancels its own vibration.

Kataoka et al. [15][16] proposed a notch filter to remove the system natural frequency component in the command input to avoid exciting the structure. Most notch filters are known to cause unwanted phase delays. Whereas, the proposed notch filter minimizes the phase delay in the command input with an additional phase compensator gain as shown in Figure 2.1. This approach is a feed forward controller which does not ensure stability of the system.
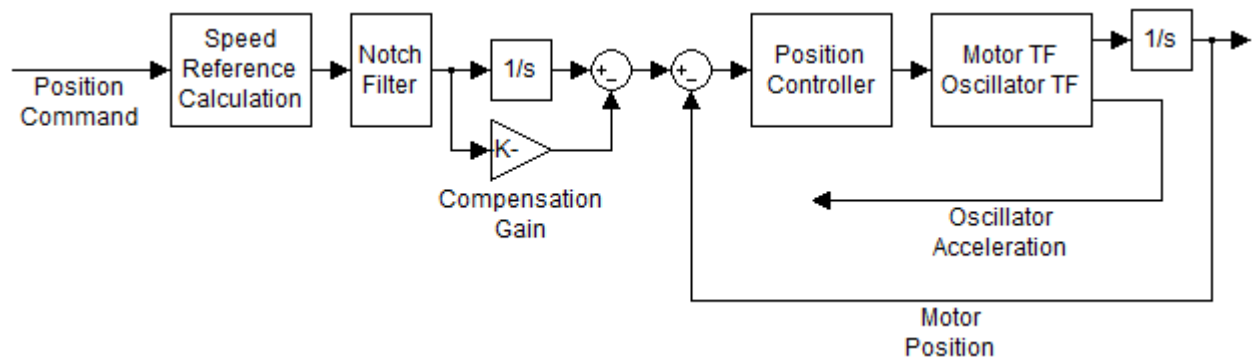
Figure 2.1: Commanding Shaping Vibration Controller with Notch Filter

The common shortcoming of the command shaping method is its vulnerability to reject any disturbance excitation since the control input is designed to only suppress vibrations caused by its reference command. Also, it is very sensitive to the uncertainties in the system model, such as the natural frequency. In comparison, the active vibration control works as a feedback control system, in which the feedback can generate an appropriate compensational control effort to suppress any vibration. Thus, the active vibration control is considered to be more reliable than reference command shaping in vibration control.

For active vibration control design, Mahmood et al. [17] has proposed the use of a resonant controller at the flexible structure feedback loop. The control scheme consists of two negative feedback loops as shown in Figure 2.2. The inner loop is designed to increase the damping of the flexible structure and the outer loop provides precise positioning. The proposed approach is designed to suppress vibrations for multimode systems. However, the use of a resonant controller can be insufficient for active vibration control. The system dynamics, specifically the system natural frequency, varies along the feed drive position. A single resonant frequency is selected in the resonant controller to correspond with one vibration mode. Thus, as the system natural frequency varies, the resonant controller cannot ensure high stability robustness. A poor selection of the resonant controller for active control can easily drive the system with more violent vibrations than the system without active control. Moreover, another disadvantage for this proposed control scheme is that leads to a much higher order system due to the resonant controller at the inner loop. Hence, the resulting high order system becomes more difficult to tune at the outer loop.
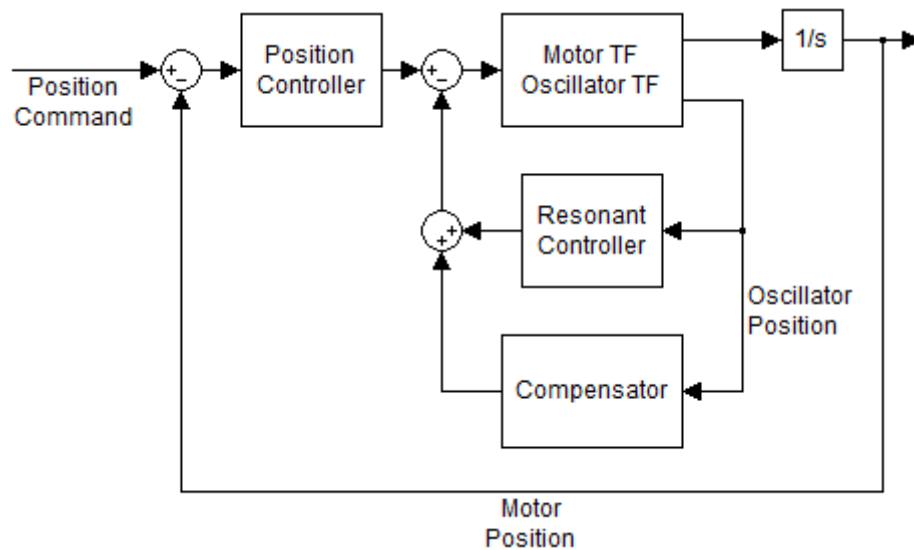
Figure 2.2: Active Vibration Controller with Resonant Controller Design

A different active vibration control approach proposed by Verscheure et al. [10] where H_∞ controller is used. This control scheme provides the system with good stability robustness and performance robustness. It combines vibration and motion control in a high and low authority control structure as shown in Figure 2.3. The high authority motion controller is built around the system with a low authority vibration controller. The purpose of the vibration controller is to assure that the acceleration of the flexible structure tracks the reference acceleration, which is taken to be zero. The motion controller is a simple controller used to control the position of the motor and to track a reference position. However, the proposed weighting function for the H_∞ controller appears to be quite specific to their experimental setup, and is not suitable for other systems.
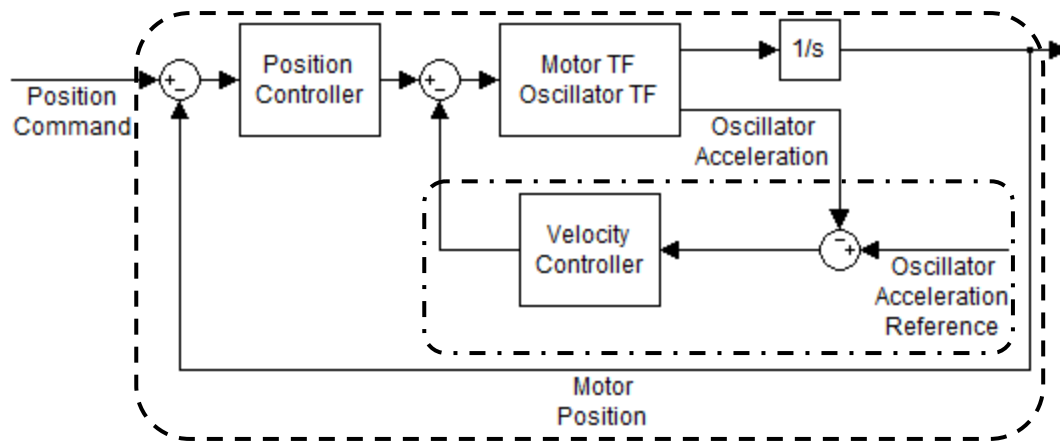
Figure 2.3: Active Vibration Controller with H_∞ Controller Design

Low Authority Controller (Dash Dot)

High Authority Controller (Dash)

Dietmair et al. [19] proposed the use of a phase compensator to form a damping network at the flexible drive velocity loop as shown in Figure 2.4. This approach is quite similar to other proposed active vibration controller designs, which consists of two control loop. The inner loop is designed for compensating the flexible structure phase delay at the resonant frequency, which effectively adds damping to the flexible structure. The outer loop is designed to track the position reference command. This proposed control strategy is favoured for its simplicity, and can be easily applied to any flexible systems. Therefore, this active phase compensator strategy is further investigated.
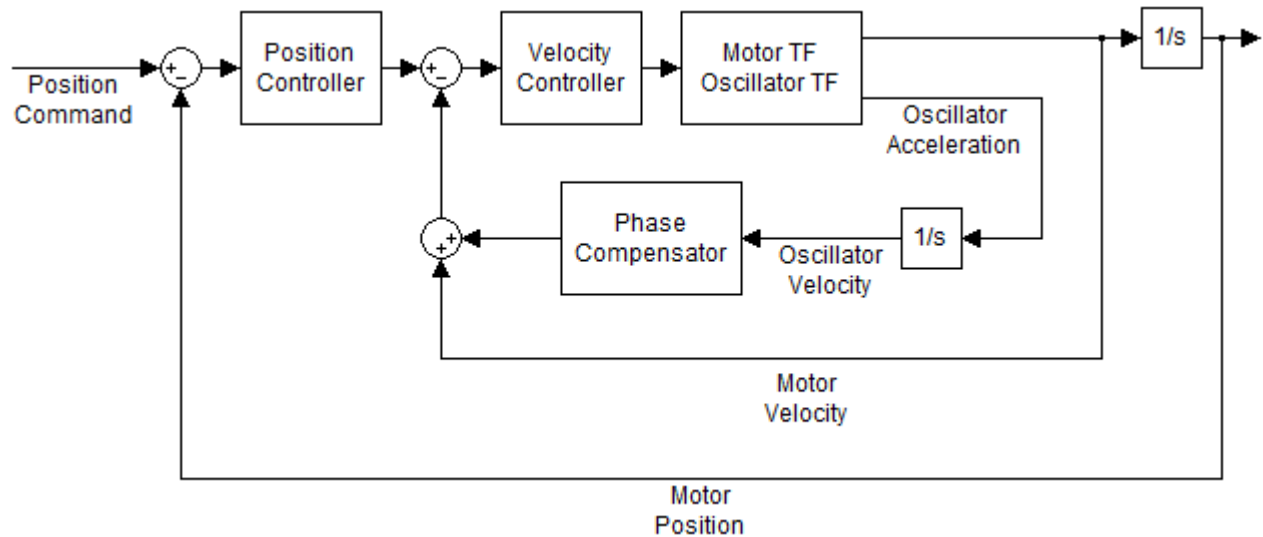
Figure 2.4: Active Vibration Controller with Phase Compensator Design

Chapter 3.   Experimental Setup

3.1   Chapter Overview

This chapter presents the experimental setup used in the thesis. An overview of the real time control system implementation and instrumentation are given in Section 3.2. In Section 3.3, the details on hardware components and its setup, including the linear motor drive and oscillator, for replicating the machine tool vibration, and the use of available sensors measuring the system performance are given.

3.2   Control System Setup

This section provides an overview of the real time controlled system in the experimental setup. An external PC is set up for controller design and provides access to dSPACE DS1103 controller board through ControlDesk software. The Siemens SIMODRIVE 611U board, a control motor driver, can be operated in either the velocity or torque operating mode as it commands its power module to send in the appropriate amount of current to operate the motor drive. When operating in the velocity mode as shown in Figure 3.1, the reference command is sent through the DS1103 controller board to the SIMODRIVE 611U drive module. The system is controlled by the SIMODRIVE 611U onboard velocity controller to ensure a constant motor velocity output which is measured by the embedded motor encoder. For custom design positioning and active vibration controller implementation through the DS1103, the SIMODRIVE 611U board should be operating in torque mode. It is because the SIMODRIVE 611U onboard current controller regulates a constant torque (force) output from the motor. The linear encoder measurement signal is used as a feedback to the custom design controller on the DS1103 controller board to form a closed control loop as shown in Figure 3.2. The experimental setup was prepared by a former M.Eng. candidate in MAL and the details can be found in his M.Eng. project report [21].
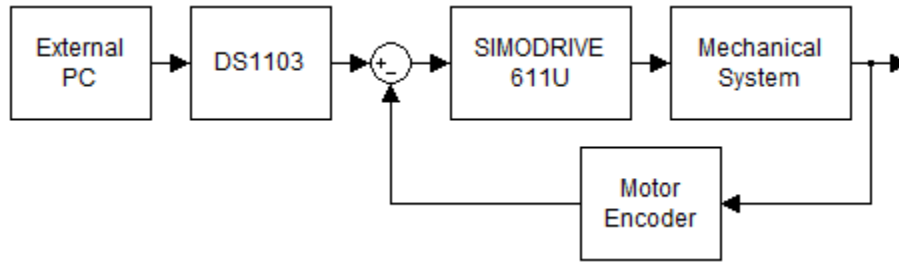
Figure 3.1: SIMODRIVE 611U in Velocity Mode Block Diagram
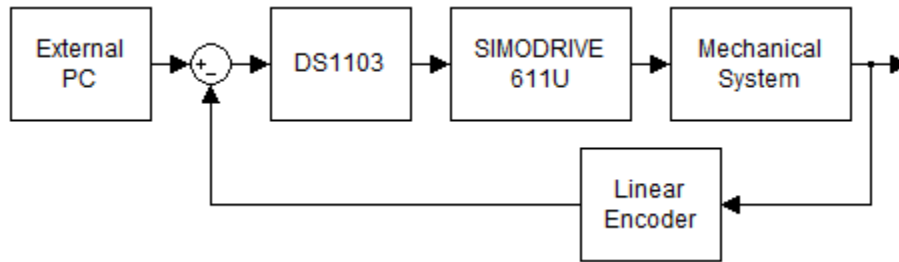
Figure 3.2: SIMODRIVE 611U in Torque Mode Block Diagram with Position Control

3.3   System Hardware Setup

3.3.1   Linear Motor

A linear electric motor has its stator and rotor lay out in parallel so the motor can produce a linear force along its length. A linear motor drive has fewer moving components than conventional linear actuator; hence it can achieve high speeds and accelerations with minimal backlash and friction. However, the absence of gear reduction between the linear motor and the table makes linear drives sensitive to the applied load, such as carrying load, cutting force or disturbance force on the motor.

The singled-sided Siemens 1FN1 series linear motor mounted on the Siemens linear table setup is used in this experimental setup. Siemens 1FN1 linear motor is a permanent magnet motor which is capable of maximum thrust of 1720 N, maximum acceleration of 2 g (19.6 m/s^2) and correspondingly a maximum free load velocity of 200 m/min. This linear motor is considered as a high force motor at the industrial standard.

To ensure safety and protection of the movable part, several rubber dampers are installed at both ends of the linear guide rail.

Temperature monitoring circuits are integrated in the motor for protecting the system against impermissible high thermal load. During operation, water of 20°C temperature at 4 L/min flow is directed into the cooling system to remove the heat generated by the motor. Under the rated conditions, the cooling system can remove up to 90% of the generated heat.

Another safety feature installed on this linear motor setup is the Balluff proximity sensor limit switch pair. At each end of the guide rail, a limit switch is installed to detect the motor. Once the motor is detected by the limit switch at the end of the guide rail, this normally closed limit switch immediately sends a signal to the SIMODRIVE 611U board deactivating the linear motor drive. This can avoid the motor from launching to the end of the guide rail and damaging the linear motor and its supporting structure.

Figure 3.3: Siemens Linear Motor and the SIMODRIVE 611U

3.3.2 Linear Encoder

The Heidenhain LIDA 18 exposed linear encoder is used to measure the displacement of the linear motor. The linear encoder consists of a scale tape and a scanning head that operate without mechanical contact. The output of the encoder is a pair of 1 V peak-to-peak sinusoidal analog signals which are 90 deg out of phase from each other. The measured signal is digitized into discrete format which can be used in the DS1103 control module. The linear encoder feedback signal is further enhanced through the use of a Heidenhain IBV606 interpolation box. The resolution of the linear encoder with the quadrature reading after interpolation is 5 micron [21].
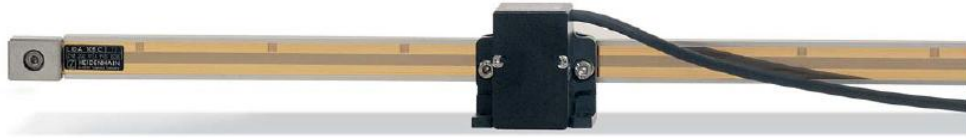
Figure 3.4: Heidenhain LIDA18 Linear Encoder

3.3.3 Single Degree Oscillator

The machine tool on a milling machine together behaves like a flexible feed drive system. As the motor position moves, it induces a force to the machine tool which the machine tool vibrates. To model and illustrate the active damping of the flexible feed drive system, a thin bar is used as a single degree of freedom (SDOF) oscillator and it is mounted on the linear motor moving platform. The thin bar structure as a SDOF oscillator is selected to ensure the structure flexibility only along the motor drive axis. Using a thin bar structure would also guarantee that its resonance is at low frequency region and the structure has a low mechanical damping property. For demonstration purpose, the oscillation and the damping of the oscillation can be easily observed. The thin bar SDOF oscillator is secured on the linear motor moving platform with a set of

custom designed brackets. As the motor moves, the thin bar should experience noticeable vibrations along the motor drive axis.

Height (mm)	Width (mm)	Thickness (mm)	Natural Frequency (Hz)
328.5	14.7	1.6	8.8

Table 3.1: Dimensions of the Aluminium SDOF Oscillator in the Experimental Setup

3.3.4   Accelerometer Sensor

Kistler 8702B500 Accelerometer has a measureable range of ±500 g (4900 m/s^2). For measuring the acceleration of the SDOF oscillator, the accelerometer is bolted on at the top end of flexible structure as shown in Figure 3.5. The accelerometer output signal is amplified through the signal amplifier before it is fed into the DS1103 control module. The accelerometer has been calibrated with a calibration exciter, Bruel & Kjaer Type 4294, so that the amplifier transducer sensitivity conversion is set to 14.4 mV/g for this experimental setup. In industrial machine tools, either Ferrari sensor [1] is used for direct measurement or double derivative of encoder signals are used for indirect measurement of acceleration of the drives.
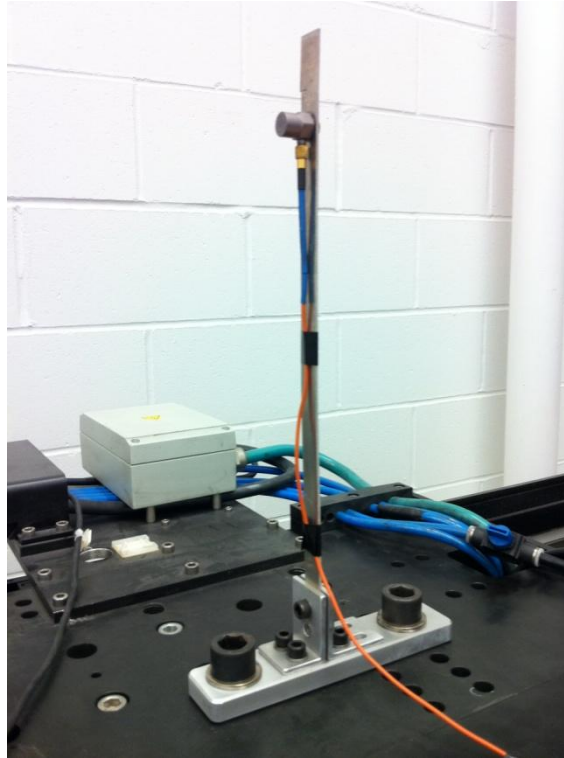
Figure 3.5: SDOF Oscillator with Accelerometer Sensor on the Linear Table

3.4   Summary

This section summarised the work discussed throughout the chapter. In Section 3.2, the control system overview, including the velocity and torque operating mode, is explained. In Section 3.3, the system hardware including the linear motor, linear encoder, SDOF oscillator and accelerometer sensor are described in detail. The Siemens linear motor is configured through the SIMODRIVE 611U module. The control command is processed through the DS1103 control board. A customised designed SDOF oscillator is mounted on the linear motor to replicate a flexible feed drive system. The linear encoder is used for measuring the motor position and the accelerometer is used for measuring the SDOF oscillator acceleration. The hardware configuration overview is provided in Figure 3.6.
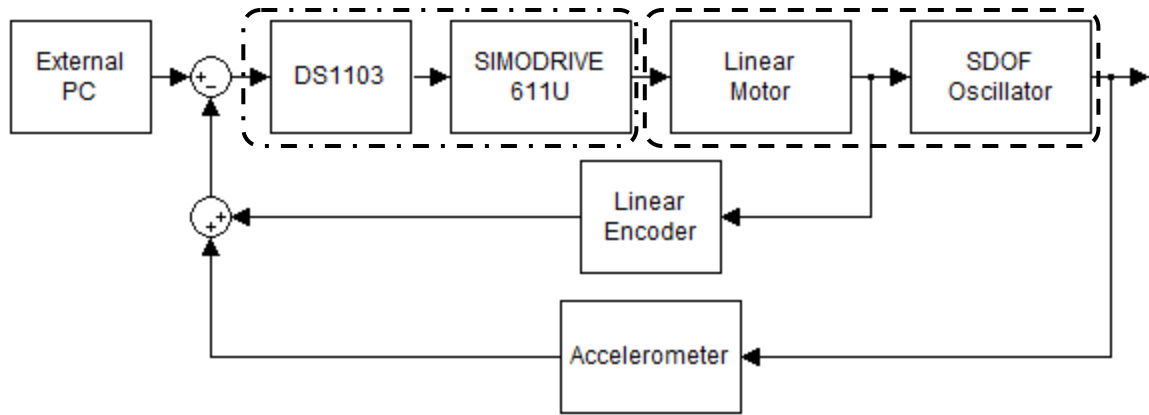
Figure 3.6: Hardware Configuration Overview

Controller (Dash Dot)

Flexible Feed Drive System (Dash)

Chapter 4. Identification of Feed Drive Dynamics

4.1 Chapter Overview

The focus of Chapter 4 is on the system characteristic. The theoretical system model transfer function for a flexible motor drive is derived in Section 4.2. In Section 4.3, experimental procedures of the different parameter identification techniques are discussed. The discussion is provided in Section 4.3.5 to compare these identification techniques. The most suitable identified model is applied to represent the actual system for controller design.

4.2 System Model

The mechanical system of a single axis flexible drive is commonly modelled as a two degree of freedom mass, spring and damper system. In this section, the theoretical model is derived to obtain the two system transfer functions of interest. The first transfer function is between voltage input, V_{in}, and motor position, x_1. The second transfer function is between voltage signal, V_{in}, and oscillator acceleration, $\ddot{x}_2$. This is because the motor position and oscillator acceleration are measurable quantities through the linear encoder and accelerometer, respectively. Then the experimentally measured system frequency responses can be compared directly with the derived transfer functions.
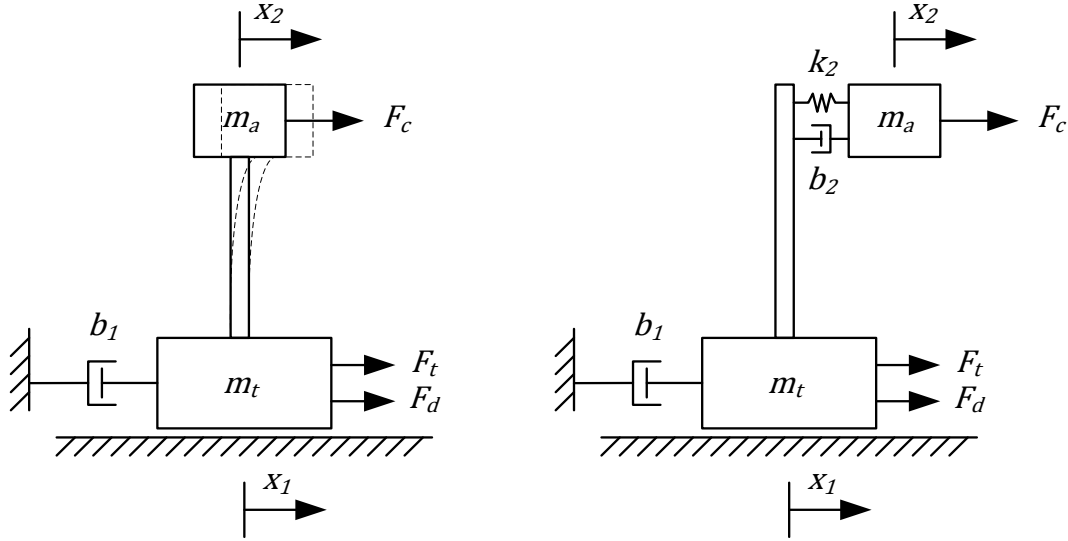
Figure 4.1: Single Degree Flexible Drive System Free Body Diagram

x_1: Motor Position

x_2: Oscillator Position

F_t: Motor Force

Consider the two degree of freedom mass, spring and damper mechanical system as shown in Figure 4.1. The driving motor force, F_t, is moving the motor mass, m_t, against the viscous friction force which is represented as a damper, b_1, on the motor. The motor mass, m_t, is also subjected to disturbance force, F_d. The SDOF oscillator is attached on the motor mass. The mechanical properties of SDOF oscillator is lumped to the top which includes the oscillator mass, m_a, damper, b_2, and stiffness, k_2. The SDOF oscillator is also under disturbance force, F_c, which may be considered as the cutting force on the machine tool during machining. To simplify the model analysis, the motor disturbance force, F_d, and oscillator disturbance force, F_c, are assumed to be zero.

The system transfer functions of interest can be derived by Laplace domain equivalent stiffness model. First obtain the time domain system stiffness model and then transform the model to Laplace domain. Each stiffness element in the Laplace domain model can

be treated as a spring element in the time domain. The following table provides the time domain and Laplace domain equivalent stiffness presentation for each element.

	Time Domain	Laplace Domain
Motor Mass	m_t	$m_t \cdot s^2$
Motor Damper	b_1	$b_1 \cdot s$
Oscillator Mass	m_a	$m_a \cdot s^2$
Oscillator Damper	b_2	$b_2 \cdot s$
Oscillator Stiffness	k_2	k_2

Table 4.1: Time and Laplace Domain Equivalent Stiffness
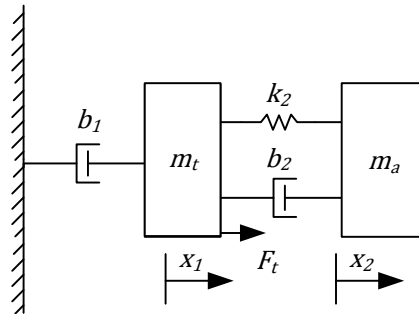
Figure 4.2: Time Domain Flexible Drive Model

The mass component in the model is considered to be attached to ground by a spring with a magnitude of its respective mass magnitude. Then the time domain stiffness is replaced with the Laplace domain equivalent stiffness as shown in Figure 4.3.
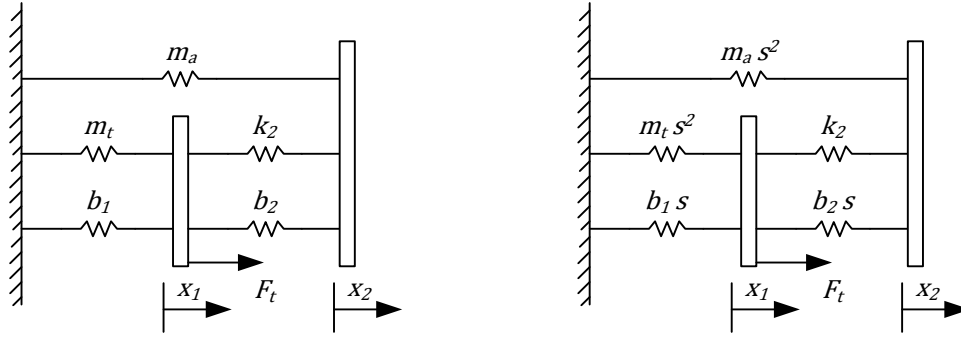
Figure 4.3: Time Domain (Left) and Laplace Domain (Right) Equivalent Stiffness Model 1

The motor mass, m_t, is in parallel with the motor damping, b_1. The oscillator stiffness, k_2, is in parallel with the oscillator damping, b_2. The parallel arrangement of the stiffness is the sum of each stiffness component. Then the result of this summation is shown in Figure 4.4.
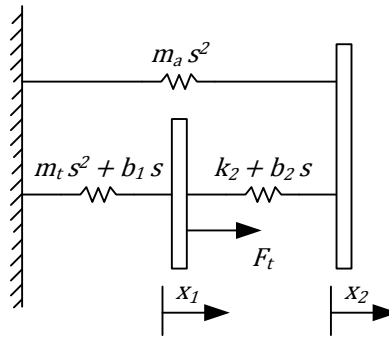
Figure 4.4: Laplace Domain Equivalent Stiffness Model 2

The model in Figure 4.4 can be illustrated differently as shown in Figure 4.5, where the motor position, x_1, is switched with the oscillator position, x_2, such that obtaining the transfer functions between the motor force, F_t, and the motor position , x_1, becomes more obvious. Now, the stiffness model becomes the longer spring at the top and it is at parallel with the two shorter springs arranged in series. Then the motor force is applied at the end.
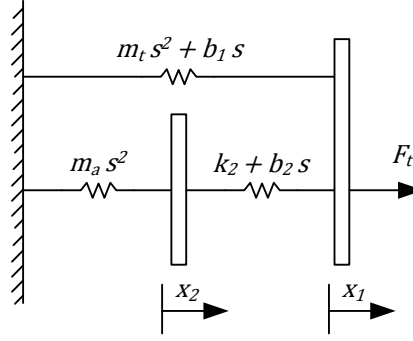
Figure 4.5: Laplace Domain Equivalent Stiffness Model 3

The transfer function between the motor force and the motor position has the following form as shown in Eq.(4.1).

$$\frac{x_1}{F_t} = \frac{m_a \cdot s^2 + b_2 \cdot s + k_2}{(m_a \cdot s^2 + b_2 \cdot s + k_2) \cdot (m_t \cdot s^2 + b_1 \cdot s) + (m_a \cdot s^2) \cdot (k_2 + b_2 \cdot s)} \tag{4.1}$$

Since the Laplace domain equivalent stiffness of the oscillator mass, m_a, and damping, b_2, magnitudes are expected to be relatively small compared to the stiffness magnitude, k_2, within the frequency of interest between 1 Hz to 35 Hz, the stiffness magnitude, k_2, should be the dominating term. This transfer function can be further simplified as shown in Eq.(4.2).

$$|k_2| \gg |m_a \cdot s^2|$$

$$|k_2| \gg |b_2 \cdot s|$$

$$\frac{x_1}{F_t} = \frac{k_2}{(k_2) \cdot (m_t \cdot s^2 + b_1 \cdot s)} = \frac{1}{m_t \cdot s^2 + b_1 \cdot s} \tag{4.2}$$

The transfer function between the motor force, F_t, and the oscillator position, x_2, can be obtained by rewriting the motor position, x_1, term with respect to the oscillator position, x_2, in Eq.(4.3).

$$x_1 = \frac{m_a \cdot s^2 + b_2 \cdot s + k_2}{b_2 \cdot s + k_2} \cdot x_2 \qquad (4.3)$$

The relationship between oscillator position and the motor position is expressed in the following form as shown in Eq.(4.4).

$$\frac{x_2}{x_1} = \frac{b_2 \cdot s + k_2}{m_a \cdot s^2 + b_2 \cdot s + k_2} \qquad (4.4)$$

Since the magnitude of the oscillator damping coefficient, b_2, is considered to be much smaller than its stiffness magnitude, k_2, the numerator of Eq.(4.4) can be considered as a constant gain at the low frequency region of interested.

$$|k_2| \gg |b_2 \cdot s|$$

$$\frac{x_2}{x_1} = \frac{k_2}{m_a \cdot s^2 + b_2 \cdot s + k_2} \qquad (4.5)$$

Then the transfer function between the motor force and oscillator position is given by Eq.(4.6).

$$\frac{x_2}{F_t} = \frac{x_1}{F_t} \cdot \frac{x_2}{x_1} = \frac{1}{m_t \cdot s^2 + b_1 \cdot s} \cdot \frac{k_2}{m_a \cdot s^2 + b_2 \cdot s + k_2} \tag{4.6}$$

Recall that the transfer function of interest is between the motor force and the oscillator acceleration. Then this is rewritten as in Eq.(4.7).

$$\frac{\ddot{x}_2}{F_t} = \frac{x_1}{F_t} \cdot \frac{x_2 \cdot s^2}{x_1} = \frac{k_2 \cdot s^2}{(m_t \cdot s^2 + b_1 \cdot s) \cdot (m_a \cdot s^2 + b_2 \cdot s + k_2)} \tag{4.7}$$

Now, the dynamics of a flexible feed drive, including the electrical and mechanical system, can be represented as shown in Figure 4.6.
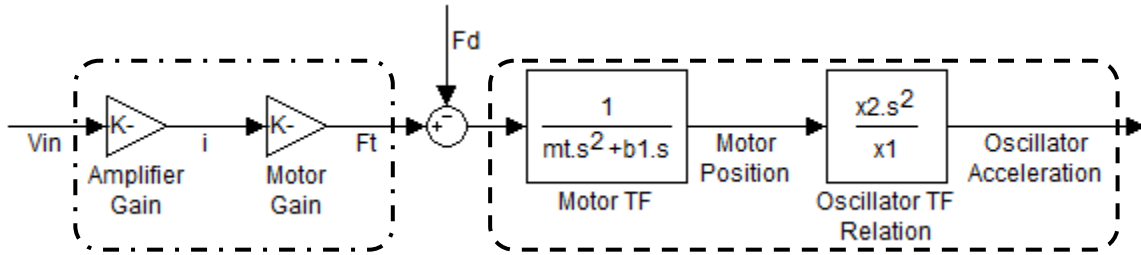
Figure 4.6: Flexible Drive Dynamics

Electrical System (Dash Dot)

Mechanical System (Dash)

V_{in} (V) is the voltage input applied to the current amplifier, denoted with the gain, K_a (A/V). The amplifier produces the current i (A) in the motor armature, resulting in the motor force F_t (N). The motor force is directly proportional to the current i (A) and motor force constant, K_t (N/A). In addition to the force produced by the current running through the armature, the motor is also subject to a disturbance force, F_d (N), which may include Coulomb friction from the guide rail or external applied force.

It should be noted that the electrical system has a much higher bandwidth than the mechanical system. The high amplifier bandwidth implies that at low frequencies, which is the mechanical system operating range, the electrical system can be approximated by the constant amplifier gain, K_a.

K_a Amplifier Gain Constant (A/V)	K_t Motor Force Gain Constant (N/A)
1.1121	142.00

Table 4.2: Amplifier and Motor Gain Constant

The system can be now rewritten as transfer functions between the input voltage, V_{in}, and the motor position, x_1, and the oscillator acceleration, $\ddot{x}_2$.

$$F_t = K_t \cdot K_a \cdot V_{in}$$

$$\frac{x_1}{V_{in}} = \frac{K_t \cdot K_a}{m_t \cdot s^2 + b_1 \cdot s} \tag{4.8}$$

$$\frac{\ddot{x}_2}{V_{in}} = \frac{K_t \cdot K_a}{m_t \cdot s^2 + b_1 \cdot s} \cdot \frac{k_2 \cdot s^2}{m_a \cdot s^2 + b_2 \cdot s + k_2} \tag{4.9}$$

4.3   Parameter Identification

Through the theoretical model, the motor position and oscillator acceleration transfer function structure are obtained. Now experimental identification is required to extract these transfer function parameters. This section presents the procedures of three techniques for identifying the Coulomb friction, viscous friction and motor mass, and two techniques for identifying the SDOF oscillator parameters.

There are many types of frictional forces that arise between contacting surfaces, the linear type being Coulomb and viscous friction, and nonlinear type such as the Stricbeck effect and static friction [2]. Here, only the linear frictions are considered in the identification process.
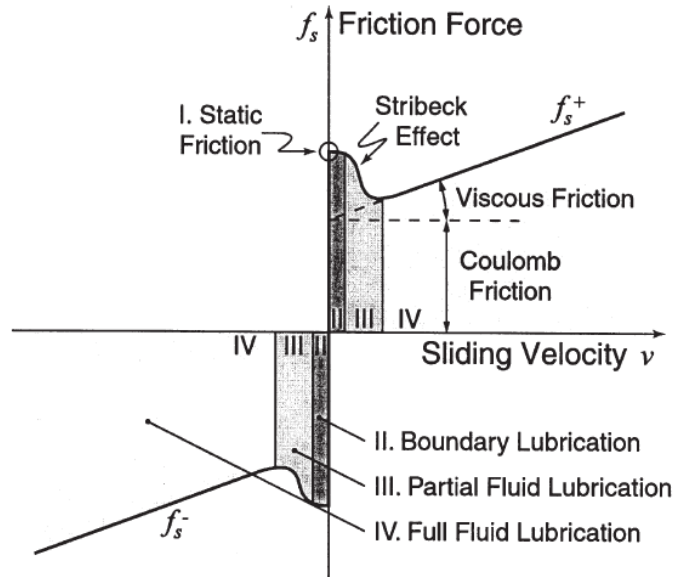
Figure 4.7: Friction Model [2]

Coulomb friction force needs to be overcome to get an object moving initially and is constant regardless the speed of the moving object. Viscous friction, on the other hand, is proportional to the speed of the moving object. The Coulomb and the viscous friction constants have to be identified for both positive and negative direction of the linear motor. The results from the different identification techniques will be compared and the most suitable model is selected for controller design.

4.3.1   Identification of Motor Dynamics by Ad-Hoc Technique

An ad-hoc technique is applied to identify the motor system parameters. This technique is favourable for its simplicity and it can generally provide good estimates of the motor mass, viscous and Coulomb friction parameters. Consider the motor drive equation of motion, Eq.(4.10), derived from Figure 4.6.

$$m_t \cdot \ddot{x}_1(t) = -b_1 \cdot \dot{x}_1(t) + K_a \cdot K_t \cdot V_{in}(t) - \mu_k \qquad (4.10)$$

m_t: Motor Mass (kg)

$\ddot{x}_1$: Motor Acceleration (m/s^2)

b_1: Viscous Friction (N·m/s)

$\dot{x}_1$: Motor Velocity (m/s)

K_a: Amplifier Gain Constant (A/V)

K_t: Motor Torque Gain Constant (N/A)

V_{in}: Voltage Input (V)

μ_k: Coulomb Friction (N)

When the motor drive is moving at a constant velocity, the motor acceleration is zero. Then the left hand side (LHS) of the equation of motion becomes zero. Since only the linear viscous friction is considered, then different voltage inputs correspond to different motor velocity outputs, and the Coulomb friction is only a force offset. Then the viscous friction is identified by jogging the motor back and forth at constant velocities. The corresponding motor current required to generate the force to move the table is recorded. The results are plotted as a motor force versus speed graph and fitted with a linear function. The linear function slope constant is interpreted as the viscous

friction coefficient. By interpolation, the fitted linear function Y-intercept corresponds to the friction at zero velocity, which it is interpreted as the Coulomb friction, μ_k.

To ensure the motor travelling at constant velocities, the SIMODRIVE 611U is selected to operate in the velocity mode. In this parameter identification analysis, only the mean values of the steady state motor current and velocity are processed. This avoids the nonlinear friction effect in the transit measurements coupled into the analyzed data. The friction identification analyzed data fitted with a linear function result is presented in Figure 4.8 and Table 4.3.
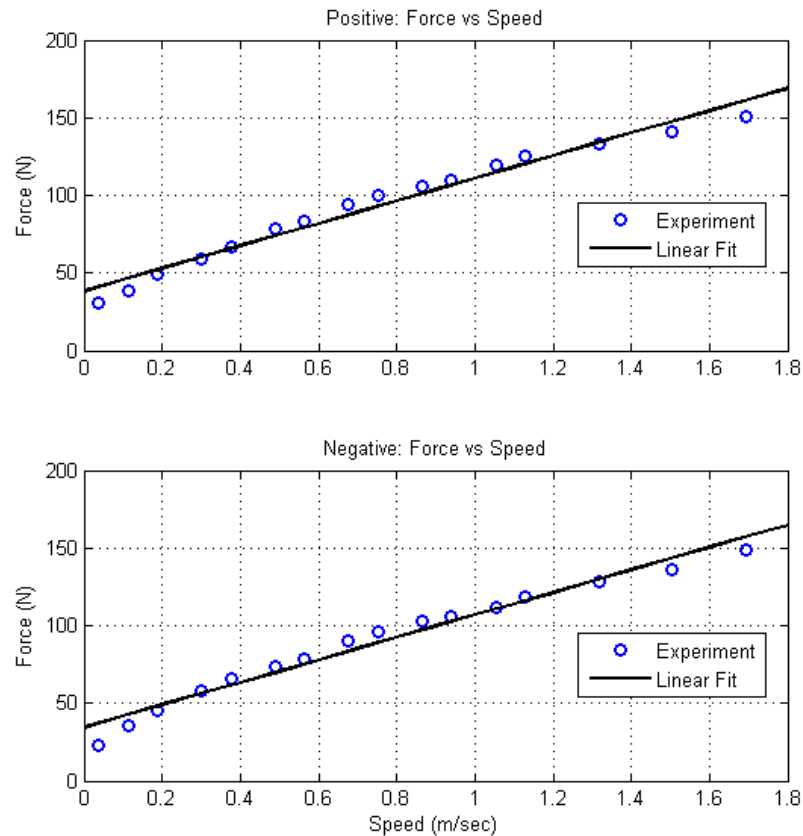
Figure 4.8: Motor Force Verses Speed Experimental Result

Direction	Slope: Viscous Friction (N·s/m)	Y-Intercept: Coulomb Friction (N)
Positive	72.6540	38.5
Negative	72.4609	34.4

Table 4.3: Viscous and Coulomb Friction Identification Results

With the Coulomb and the viscous friction identified, the motor mass, m_t, is the only remaining unknown in the motor drive equation of motion. To identify the motor mass, the motor is driven in open loop with a series of square wave commands at different amplitudes while the velocity is measured by the linear encoder. The measured velocity and corresponding voltage input signal are known variables on right hand side (RHS) of the motor drive equation of motion in. The motor acceleration on left hand side (LHS) of the motor drive equation of motion can be obtained by taking the differentiation of the corresponding velocity measurement. The LHS and RHS of the motor drive equation of motion are graphed. The motor mass, m_t, parameter is adjusted until the LHS coincides with the RHS of the motor drive equation of motion.
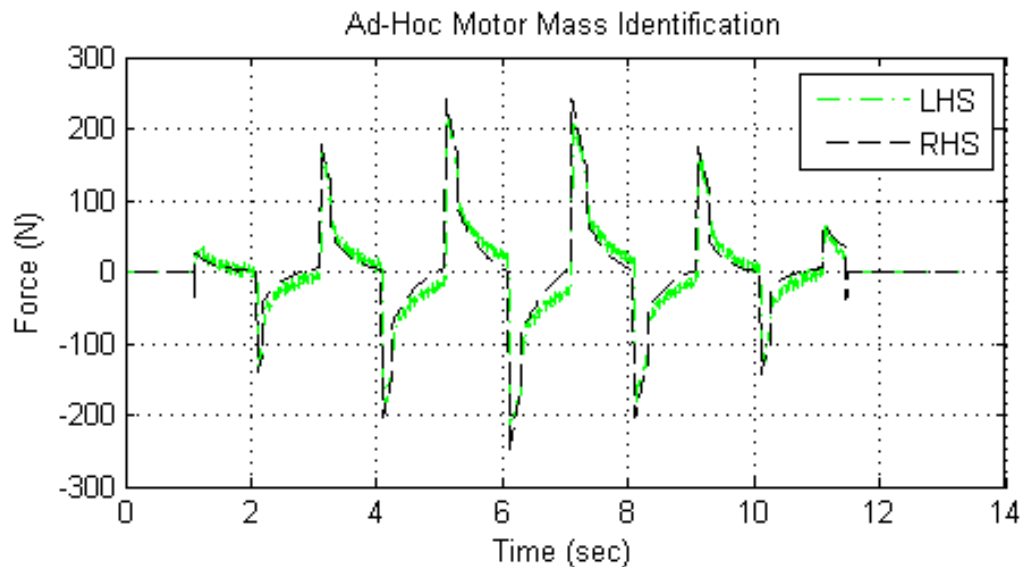
Figure 4.9: Ad-Hoc Motor Mass Identification

Motor Mass, m_t (kg)	30.5
Motor Viscous Friction Coefficient, b_1 (N·s/m)	72.6
Positive Coulomb Friction, μ_+ (N)	38.5
Negative Coulomb Friction, μ_- (N)	34.4
Average Coulomb Friction, μ_k (N)	36.4

Table 4.4: Motor Mass and Friction Identification Results by Ad-Hoc Technique

The identified result of the motor position frequency response by the ad-hoc technique is plotted against the sine sweep experimental result as shown in Figure 4.10.
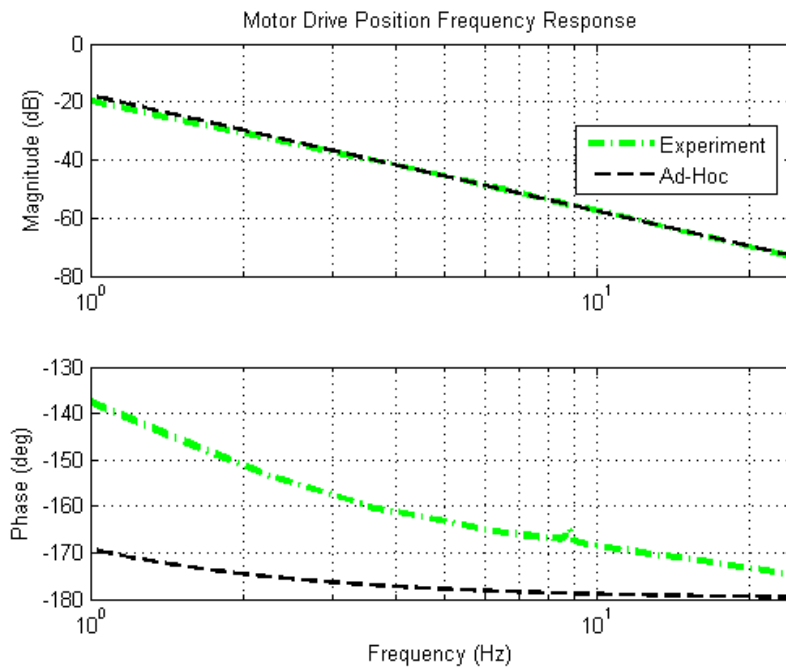
Figure 4.10: Motor Position Frequency Response by Ad-Hoc Technique

4.3.2 Identification of Motor Dynamics by Unbiased Least Square Technique

The unbiased least square (ULS) technique presented by Erkorkmaz et al. [2] is a mathematical approach for identifying the system parameters which includes the motor mass, viscous and Coulomb friction. This approach works similar to a simple least square method which the identified parameters have the sum of the square of the errors minimized but also takes account for the presence of Coulomb friction in its formulation. Recall the motor drive position transfer function and convert it to Laplace domain.

$$m_t \cdot x_1(s) \cdot s^2 = -b_1 \cdot x_1(s) \cdot s + K_a \cdot K_t \cdot V_{in}(t) - \mu_k \quad (4.11)$$

$$x_1(s) = \frac{K_t \cdot K_a \cdot V_{in}(s) - \mu_k(s)}{m_t \cdot s^2 + b_1 \cdot s} \quad (4.12)$$

To facilitate a disturbance estimation, Coulomb friction is assumed as an act of the input signal disturbance, d_f, as shown in Eq.(4.13).

$$\mu_k(s) = K_t \cdot K_a \cdot d_f \quad (4.13)$$

Now, the motor position transfer function can be expressed in terms of the voltage input with disturbance input as shown in Eq.(4.14),

$$x_1(s) = \frac{K_t \cdot K_a}{m_t \cdot s^2 + b_1 \cdot s} \cdot \left(V_{in}(s) - d_f(s)\right) \quad (4.14)$$

$$x_1(s) = \frac{K_t \cdot K_a}{m_t \cdot s^2 + b_1 \cdot s} \cdot u(s) \tag{4.15}$$

and the motor velocity transfer function as shown in Eq.(4.16).

$$\dot{x}_1(s) = \frac{K_t \cdot K_a}{m_t \cdot s + b_1} \cdot u(s) \tag{4.16}$$

The voltage input command is processed through an analog to digital converter, and hence the velocity expression in Eq.(4.16) should be transformed into discrete time domain with a zero order hold at the input stage as shown in Eq.(4.17). The details of the derivations are given in Appendix A.

$$\dot{x}_1(z) = \frac{K_{vd}}{z - P_{vd}} \cdot u(z) \tag{4.17}$$

$$K_{vd} = \frac{K_v}{-P_v} \cdot (1 - e^{P_v \cdot T_s}) \quad P_{vd} = e^{P_v \cdot T_s}$$

$$\dot{x}_1(z+1) = P_{vd} \dot{x}_1(z) + K_{vd} \cdot u(z) \tag{4.18}$$

z is replaced by $k \cdot T_s$ for each sampling instance. For simplicity, $k \cdot T_s$ is written as k.

$$\dot{x}_1(k+1) = P_{vd} \cdot \dot{x}_1(k) + K_{vd} \cdot u(k) \tag{4.19}$$

$$\dot{x}_1(k+1) = P_{vd} \cdot \dot{x}_1(k) + K_{vd} \cdot V_{in}(k) - K_{vd} \cdot d_f \tag{4.19}$$

Since Coulomb friction is the only disturbance considered in this model, the disturbance, d_f, is a function of the motor velocity, $\dot{x}_1$. This can be represented by the equation as shown in Eq.(4.20).

$$d_f(\omega(k)) = PV(\dot{x}_1(k)) \cdot d_f{}^+ + NV(\dot{x}_1(k)) \cdot d_f{}^- \tag{4.20}$$

$$PV = \frac{1}{2}\sigma(\dot{x}_1(k)) \cdot \left(1 + \sigma(\dot{x}_1(k))\right) \tag{4.21}$$

$$NV = -\frac{1}{2}\sigma(\dot{x}_1(k)) \cdot \left(1 - \sigma(\dot{x}_1(k))\right) \tag{4.22}$$

$$\sigma = \begin{cases} 0 & if \ \dot{x}_1(k) = 0 \\ 1 & if \ \dot{x}_1(k) > 0 \\ -1 & if \ \dot{x}_1(k) < 0 \end{cases} \tag{4.23}$$

Now, all output is a function of the previous states. Then all N measurement samples are presented in a matrix form as shown in Eq.(4.24).

$$Y = \Phi\theta \tag{4.24}$$

$$Y = \begin{bmatrix} \dot{x}_1(2) \\ \dot{x}_1(3) \\ \vdots \\ \dot{x}_1(N) \end{bmatrix} \quad \theta = \begin{bmatrix} P_{vd} \\ K_{vd} \\ K_{vd}\,d_f{}^+ \\ K_{vd}\,d_f{}^- \end{bmatrix}$$

$$\Phi = \begin{bmatrix} \dot{x}_1(1) & V_{in}(1) & -PV(1) & -NV(1) \\ \dot{x}_1(2) & V_{in}(2) & -PV(2) & -NV(2) \\ \vdots & \vdots & \vdots & \vdots \\ \dot{x}_1(N-1) & V_{in}(N-1) & -PV(N-1) & -NV(N-1) \end{bmatrix}$$

where Y is the output vector. Φ is the regressor matrix. θ is the parameter vector to be estimated.

The objective in the parameter estimation process is to find the parameter estimate vector, $\hat{\theta}$, that minimizes the cost function, Eq.(4.25).

$$V(\hat{\theta}) = \frac{1}{2}(Y - \Phi\hat{\theta})^T (Y - \Phi\hat{\theta}) \tag{4.25}$$

The optimal parameter estimate vector to minimize $V(\hat{\theta})$ is given in Eq.(4.26).

$$\hat{\theta} = (\Phi^T\Phi)^{-1}\Phi Y \tag{4.26}$$

$$\hat{P}_{vd} = \hat{\theta}(1) \quad \hat{K}_{vd} = \hat{\theta}(2) \quad \hat{d}_f^{\,+} = \frac{\hat{\theta}(3)}{\hat{K}_{vd}} \quad \hat{d}_f^{\,-} = \frac{\hat{\theta}(4)}{\hat{K}_{vd}}$$

The parameter estimate vector for extracting the estimate motor mass, viscous friction and both positive and negative Coulomb friction are shown as the following equations accordingly.

$$\hat{m}_t = \frac{(\hat{P}_{vd} - 1) \cdot K_t \cdot K_a \cdot T_s}{\hat{K}_{vd} \cdot \ln(\hat{P}_{vd})} \tag{4.27}$$

$$\hat{b}_1 = \frac{\left(1 - \hat{P}_{vd}\right) \cdot K_t \cdot K_a}{\hat{K}_{vd}} \tag{4.28}$$

$$\hat{\mu}_+ = K_t \cdot K_a \cdot \hat{d}_f{}^+ \tag{4.29}$$

$$\hat{\mu}_- = K_t \cdot K_a \cdot \hat{d}_f{}^- \tag{4.30}$$

To identify the parameters, the amplitude of the input signal has been scaled with different gain factors, K_u, such that different velocity ranges are measured. Then the parameters, $\hat{m}_t$, $\hat{b}_1$, $\hat{d}_f{}^+$ and $\hat{d}_f{}^-$ are estimated for the cases where sufficient excitation is achieved to overcome the static friction.
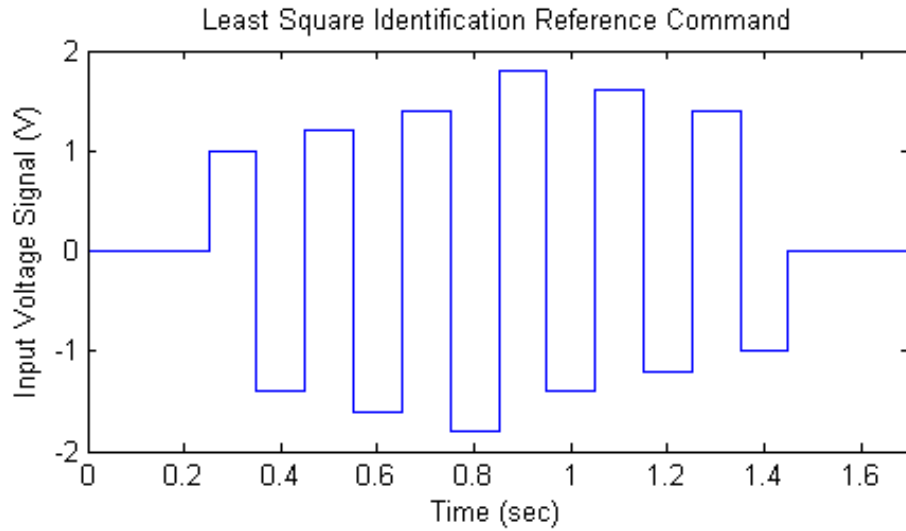
Figure 4.11: Typical Voltage Input Signal Command for ULS Technique
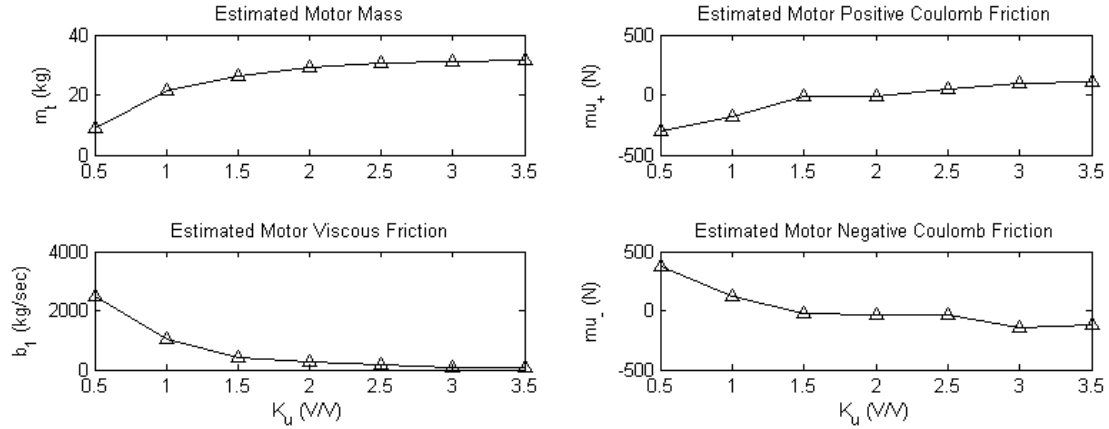
Figure 4.12: Estimated Parameters by ULS Technique

By increasing the scaling factor, K_u, the estimated parameters converge as shown in Figure 4.12. Thus, the converged values are chosen to be the identified system parameters which are listed in Table 4.5.

Motor Mass, m_t (kg)	30.7
Motor Viscous Friction Coefficient, b_1 (N·s/m)	156.1
Positive Coulomb Friction, μ_+ (N)	45.1
Negative Coulomb Friction, μ_- (N)	-41.7
Average Coulomb Friction, μ_k (N)	43.4

Table 4.5: Motor Mass and Friction Identification Results by ULS Technique

The identified result of the motor position frequency response by ULS technique is plotted against the sine sweep experimental result as shown in Figure 4.13.
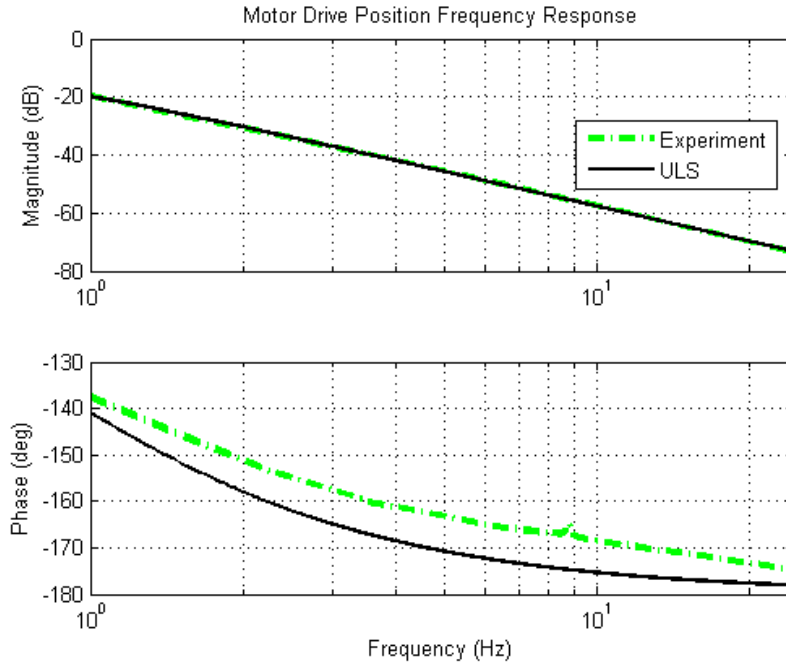
Figure 4.13: Motor Position Frequency Response by ULS Technique

4.3.3   Identification of Structural Flexibility by Impact Modal Test

The parameter identification test for the SDOF oscillator is conducted by an impact modal test. An ideal impact to a structure is a perfect impulse, which has an infinitely small duration, creating a constant amplitude input in frequency domain. This would result in all modes of the system to be excited with equal energy. Thus, the impact by the hammer is intended to reproduce such impulse input. During the identification, the test hammer is required to strike the SDOF oscillator as quickly as possible since the excited frequency range is inversely proportional to the contact time between the test hammer and the SDOF oscillator [1]. The PCB Piezotronics 086C80 impulse hammer with the calibrated sensitivity of 22.2 mV/N is used to exert the impact force. The load cell on the impulse hammer obtains a recording of the impact force and the accelerometer sensor on the SDOF oscillator captures the structure acceleration response. CUTPRO 9.0 software from MAL is used to process the acquired data and conduct the modal analysis

for estimating the SDOF oscillator modal parameters. The identified modal parameters are listed in Table 4.6.

Oscillator Mass, m_a (kg)	0.0116
Oscillator Damping Coefficient, b_2 (N·s/m)	0.0041
Oscillator Stiffness, k_2 (N/m)	35.5

Table 4.6: Oscillator Identification Results by Impact Modal Test

Recall the oscillator acceleration transfer function in Eq.(4.31) which is between the voltage input and oscillator acceleration. The sine sweep experimental measurement is also taken from the voltage input to oscillator acceleration.

$$\frac{\ddot{x}_2}{V_{in}} = \frac{K_t \cdot K_a}{m_t \cdot s^2 + b_1 \cdot s} \cdot \frac{k_2 \cdot s^2}{m_a \cdot s^2 + b_2 \cdot s + k_2} \qquad (4.31)$$

In order to compare the SDOF oscillator impact modal test result with the sine sweep experimental result, the dynamics of the motor must also be included. As for now, the ULS identified parameters are used with the impact modal test identified parameters to form the oscillator acceleration transfer function. This oscillator acceleration transfer function by impact modal test is plotted against the sine sweep experiment result as shown in Figure 4.14.
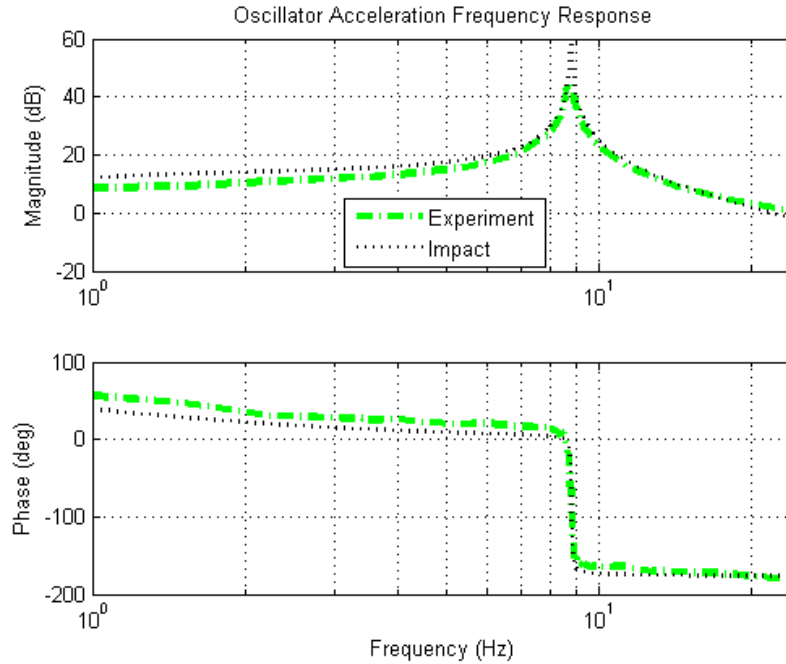
Figure 4.14: Oscillator Acceleration Frequency Response by Impact Modal Test

4.3.4 Identification of System Dynamics by Sine Sweep Technique with Nonlinear Least-Square Optimization

Sine sweep technique with nonlinear least square (NLS) optimization is conducted by commanding the motor drive in open loop with a sinusoidal command input over a frequency range containing the system natural modes. During the experiments, the voltage input, motor position and oscillator acceleration are recorded to construct the motor position and oscillator acceleration frequency response Bode plot. The NLS optimization modal identification algorithm provided by the UBC Control Engineering Laboratory is applied to fit the experimental data and extract the system parameters. The advantage of this optimization algorithm is to ensure the identified parameters to have a real physical interpretation by restricting the parameters to be within a set that is determined by a priori knowledge. In this experimental setup, for instance, the parameters such as natural frequency and damping ratio must be positive and less than unity, respectively. Recall the structure of transfer functions derived in Section 4.2.

$$\frac{x_1}{V_{in}} = \frac{K_t \cdot K_a}{m_t \cdot s^2 + b_1 \cdot s} \tag{4.32}$$

$$\frac{\ddot{x}_2}{V_{in}} = \frac{K_t \cdot K_a \cdot s^2}{m_t \cdot s^2 + b_1 \cdot s} \cdot \frac{k_2}{m_a \cdot s^2 + b_2 \cdot s + k_2} \tag{4.33}$$

To process the optimization algorithm, the transfer functions are required to be rewritten into a different presentation form with the elements presented in a series of vibration modes as shown in Eq. (4.34) and Eq.(4.35). Therefore, there are five parameters, K_1, K_2, p, ζ_d, and ω_d, to be identified at these transfer functions. The identified parameters are listed in Table 4.7.

$$\frac{x_1}{V_{in}} = \frac{K_1}{s \cdot (s + p_d)} \tag{4.34}$$

$$\frac{\ddot{x}_2}{V_{in}} = \frac{K_2 \cdot s^2}{s \cdot (s + p_d) \cdot (s^2 + 2 \cdot \zeta_d \cdot \omega_d \cdot s + \omega_d{}^2)} \tag{4.35}$$

K_1	5.3394
K_2	12689
p_d	10.7555
ζ_d	0.0089
ω_d	55.2283

Table 4.7: Motor and Oscillator Identification Results by Sine Sweep Technique with NLS Optimization

The identified results of the motor position and oscillator acceleration frequency response by sine sweep technique with NLS optimization are plotted against the sine sweep experiment result as shown in Figure 4.15 and Figure 4.16, respectively.
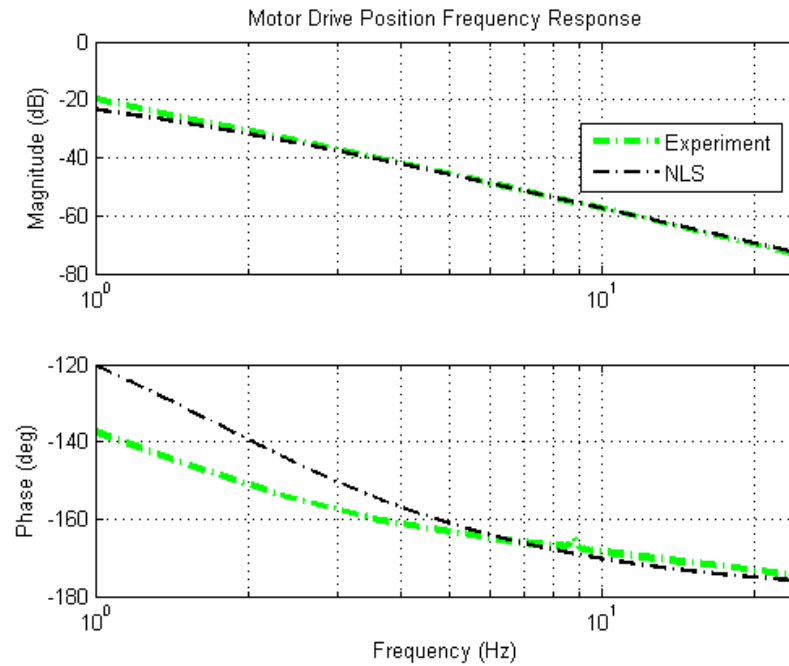
Figure 4.15: Motor Position Frequency Response by Sine Sweep Technique with NLS Optimization
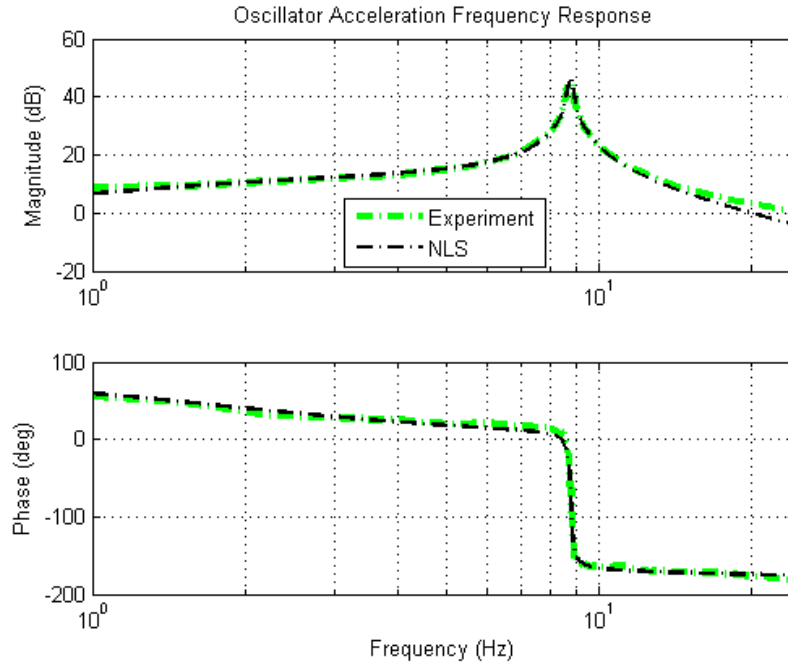
Figure 4.16: Oscillator Acceleration Frequency Response by Sine Sweep Technique with NLS Optimization

4.3.5 Discussion

Different techniques have been applied to identify the motor and oscillator parameters. In this section, the advantages and disadvantages, and challenges involved in conducting each identification technique are discussed. The most suitable identified model is selected for controller design.

In Section 4.3.1, the presented ad-hoc technique is a simple identification method that is easy to apply for estimating the motor drive parameters. However, it has a crucial limitation in estimating the motor mass. The motor mass estimation is highly dependent on the user's interpretation of the experimental data because matching the force graph of the LHS plot and RHS plot is done manually by the user. Thus, the accuracy of the motor mass estimate is limited. By inspection, the motor mass matching variation is not noticeable within ± 0.5 kg from the experiment result.

In Section 4.3.2, the presented ULS technique is a mathematical approach for identifying the motor drive parameters. This technique does not rely on the user's interpretation of the experimental result as opposed to the ad-hoc technique. During the identification process, the greatest challenge is the preparation of an appropriate voltage input signal command waveform as shown in Figure 4.11. Without a proper input command waveform, it is difficult to have the estimate parameters converged by increasing the scaling factor of the voltage input signal. If the time duration of each command waveform step is set too long, the high voltage input command would send the motor to the end of the guide rail. When the motor reaches the end of the guide rail, the motor triggers the limit switch which disables the amplifier and motor drive. Then the identification process is terminated. If the time duration of each command waveform step is set too short, that is same as sending in a high frequency input, then the estimated parameters become unreliable due to high phase delay in the motor drive.

In Section 4.3.3, the impact modal test is applied to identify the SDOF oscillator system parameters. The modal parameter estimations were taken from the average of ten separate measurements. However, it is difficult to strike the impact hammer at the same small area on the oscillator during each measurement. Thus, the impact location variation may deteriorate the accuracy of the estimated parameters. Another drawback with this identification approach is that the impact excitation force is preferably applied at the motor moving platform to replicate the motor force. Instead, the excitation force is applied at the oscillator. It is because when the impact excitation force is applied at the motor moving platform, the test result shows a vibration mode occurring at 3 Hz as well. It seems like the impact force excited parts of the motor which it did not with the sine sweep excitation. Then the identified oscillator dynamics must be coupled with a previously identified motor dynamics in order to form the oscillator acceleration transfer function. Hence, the accuracy of the identified oscillator acceleration transfer function is also depended on the accuracy of the identified motor dynamics.

In Section 4.3.4, the implementation of the sine sweep technique with NLS optimization is discussed. This is a practical system identification approach in determining all system

parameters in an efficient manner. Both the motor and oscillator parameters are acquired simultaneously. However, there are two minor drawbacks. The first drawback is that only finite input frequencies are selected in the sine sweep process. It is rare that the exact natural frequency point is selected to capture the maximum resonance response. This also leads to the second drawback. More frequency points are usually selected at the proximately of the structure resonant frequency. This causes the NLS optimization algorithm to weight in much heavily at that frequency range for experimental data fitting. Thus, the optimization algorithm identified result matches well mostly at the resonance frequency range and shows higher discrepancy outside that frequency range as shown in Figure 4.15. To improve the identified result, data points should be taken evenly across the frequency of interest to avoid the issue with heavy weight in result in the frequency with more data points.

All the motor position and oscillator acceleration identified frequency responses are plotted and compared against the sine sweep experimental result in Figure 4.17 and Figure 4.18, respectively.

For the motor dynamics identification, the experimentally measured motor position frequency response magnitude matches well against all the identified magnitude responses. The deviations between the experimentally measured motor position frequency response phase and the identified phase responses are more noticeable. Among the three implemented techniques, the NLS optimized and ULS result display a better match to the experimental result. The NLS optimized result shows a better fit near resonance frequency. However, it has a higher phase mismatch at lower frequency in comparison with the ULS identified result. The ULS identified result matches well against the experimental result only with a small constant phase offset which should provide a more conservative model for controller design. Therefore, the ULS identified model is selected to represent the actual motor dynamics for controller design.

It should be noted that this phase offset may due to a number of reasons. One reason may be the effect of the nonlinear friction along the guide way. Another reason for this constant phase offset can be the phase delay introduced by the measuring process.

Nonetheless, for modelling and controller design simplicity, the small constant phase offset in the motor position frequency response should be acceptable.
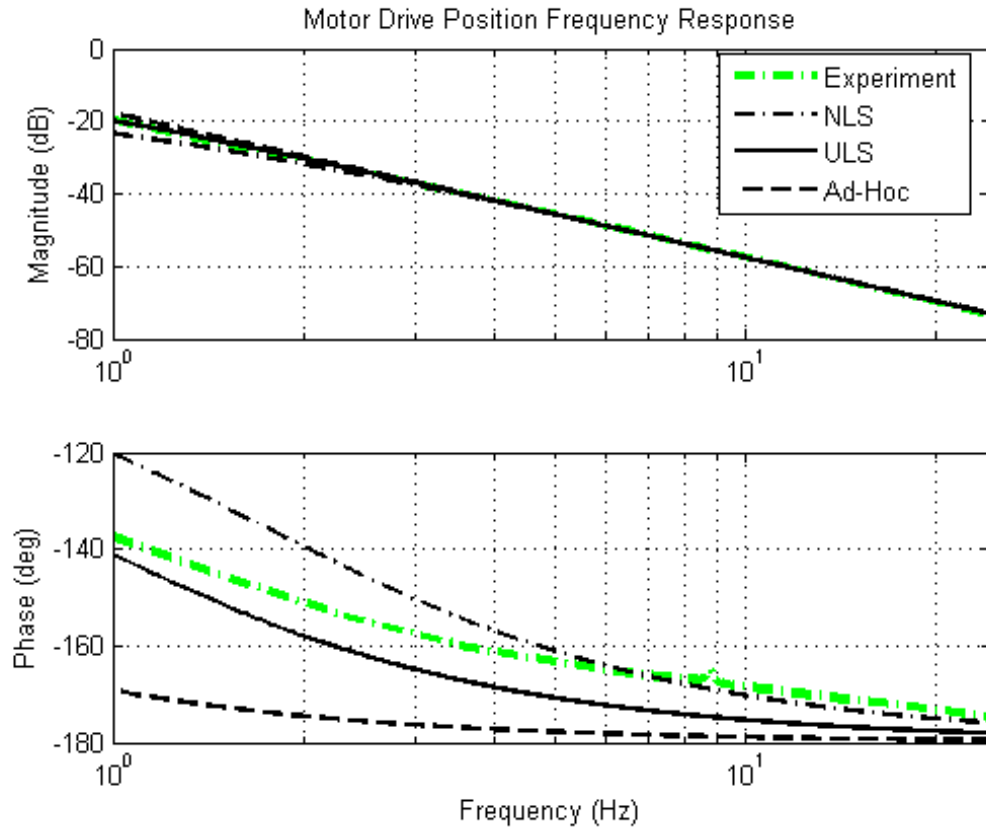
Figure 4.17: Motor Position Frequency Response Comparison

The maximum deviations between the experimental and identified frequency responses are obtained by inspection. The detail results are listed in Table 4.8.

Implemented Technique	Magnitude (dB)	Phase (deg)
Ad-Hoc	+1.9 at 1 Hz	-31.7 at 1 Hz
ULS	-0.2 at 1 Hz	-7.3 at 6 Hz
NLS Optimization	-3.6 at 1 Hz	+17.2 at 1 Hz

Table 4.8: Motor Position Frequency Response Maximum Deviation

For the oscillator acceleration dynamics identification, the sine sweep experimentally measured oscillator acceleration frequency response matches well against the NLS optimized and impact modal test result.

Ideally, the impact modal test is capable of capturing a better frequency response of the SDOF oscillator at resonant since the impact force is capable of exciting the full frequency spectrum across the natural frequency range. However, an ideal impact is difficult to achieve. Also, the accuracy of the oscillator acceleration identified result is also limited by the identified motor dynamics that coupled with. As previously discussed, the identified motor dynamics is not exact. Of the two identified oscillator acceleration frequency responses, the frequency response obtained by the NLS optimized result is chosen for controller design because this identified frequency response shows a consistent match to the experimental result throughout the frequency range of interest.
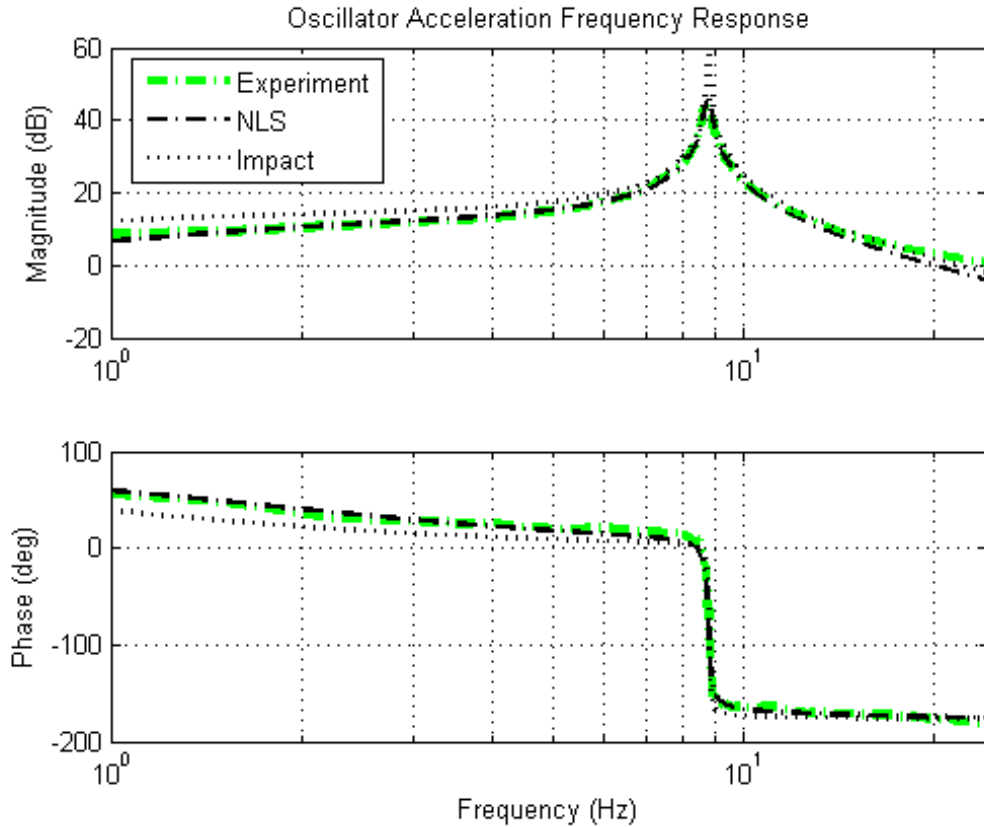
Figure 4.18: Oscillator Acceleration Frequency Response Comparison

Extended work is conducted to validate the assumption that the oscillator stiffness magnitude is much greater than the magnitude of its mass and damping coefficient. With this assumption, the transfer functions are possible for system order reduction simplification as presented in Section 4.2. The motor position and oscillator acceleration transfer function without simplification are processed through the NLS optimization modal identification algorithm. The NLS optimized transfer function with and without simplification results are compared in Figure 4.19 and Figure 4.20. The results show that the assumption for the system order reduction simplification is valid because the system with simplification matches well against the system without simplification. Between the two results, the magnitude difference is no more than half decibel and the phase difference is no more than 2 deg.
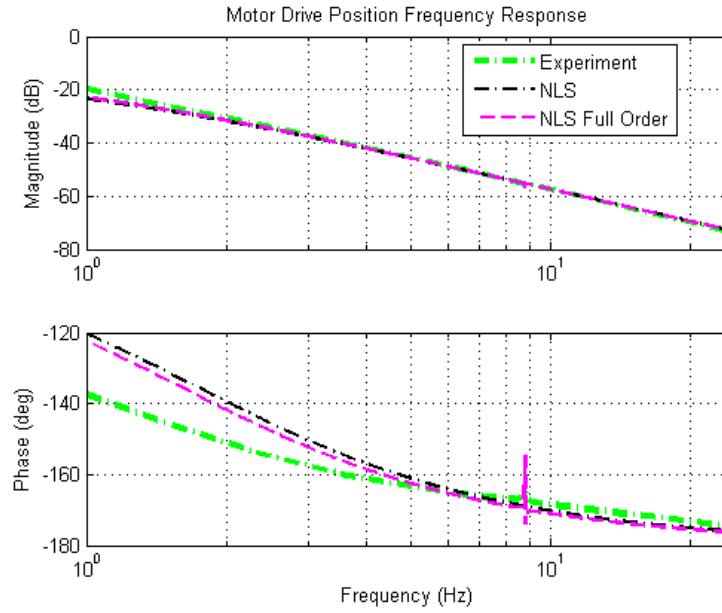
Figure 4.19: Motor Position Frequency Response by Sine Sweep Technique with NLS

Optimization with and without Order Reduction
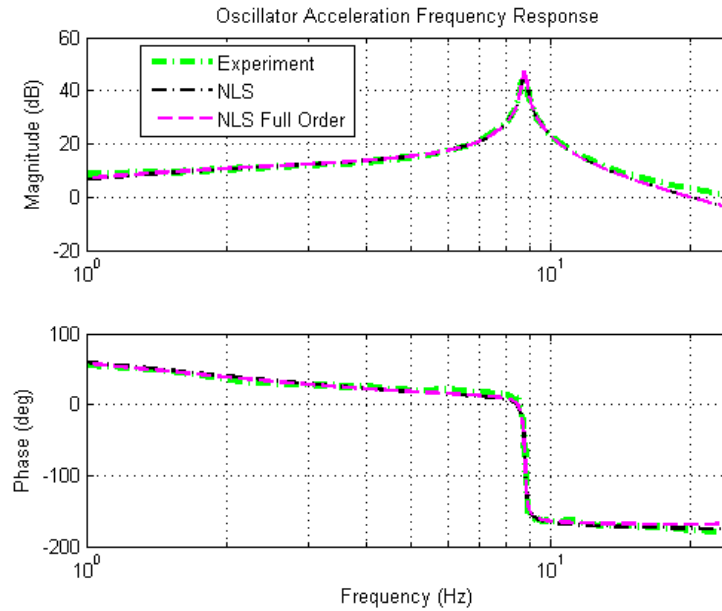
Figure 4.20: Oscillator Acceleration Frequency Response by Sine Sweep Technique with

NLS Optimization with and without Order Reduction

4.4   Summary

This section recaps the work discussed throughout the chapter. In Section 4.2, the flexible drive system is modelled as a theoretical two degree of freedom mass, spring and damper system. Through the theoretical model, the structure of the two transfer functions of interest is obtained. The first transfer function is between the voltage input to the motor position. The second transfer function is between the voltage input to the SDOF oscillator acceleration. In Section 4.3, different system identification techniques are presented. The identified frequency responses are analyzed and compared against the experimental results. The motor position frequency response model by ULS technique and the SDOF oscillator acceleration frequency response model by NLS optimization are selected for controller design. The results of the identified motor position and oscillator acceleration frequency response are shown in Figure 4.21 and Figure 4.22, respectively.
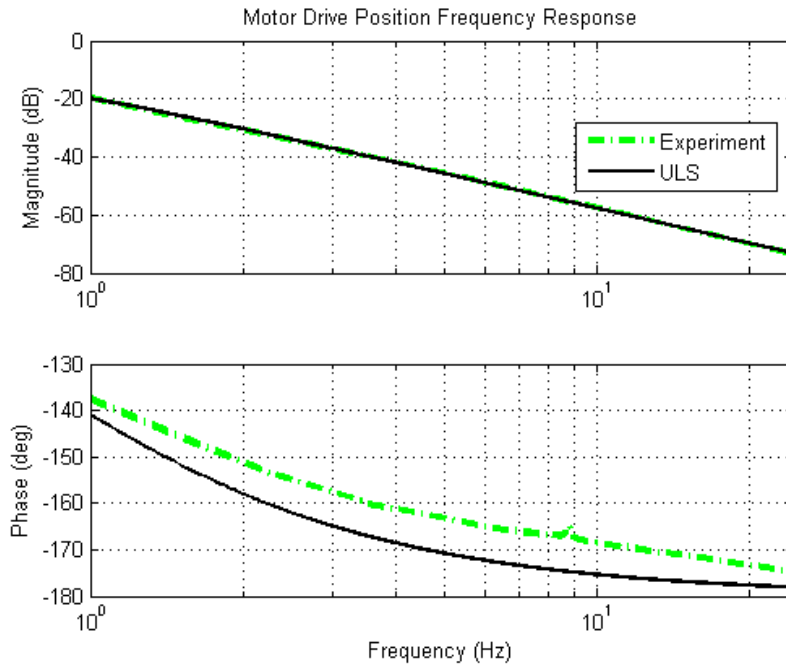
Figure 4.21: Motor Position Frequency Response by ULS Technique
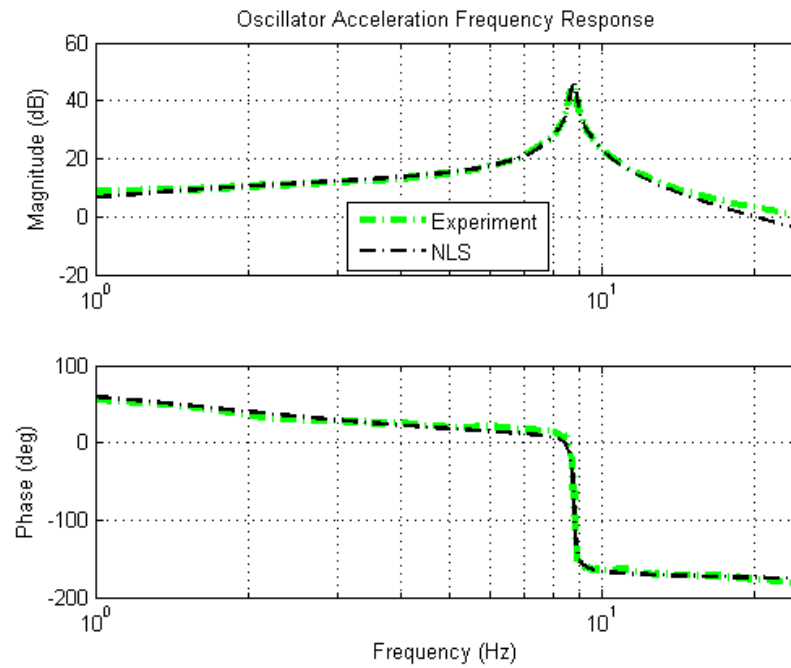
Figure 4.22: Oscillator Acceleration Frequency Response by Sine Sweep Technique with

NLS Optimization

Chapter 5.   Digital Control of Feed Drives

5.1   Chapter Overview

Two types of control strategies are presented in this chapter. The first strategy is the positioning control of a rigid body feed drive. The positioning controller and state observer design are shown in Section 5.2. The second strategy is the active vibration control of a flexible feed drive. The active controller design and implementation modifications are presented in Section 5.3. Both types of controlled system performance are validated through simulations and experiments.

5.2   State Space Position Control

The feed drive positioning performance is usually specified by the system overshoot percentage, settling time, and/or peak time. In this section, the focus is to design and implement a state space pole placement position controller to achieve the specified performance. The pole placement control strategy assigns the desired poles to the closed loop system to meet the system performance criteria.

5.2.1   State Space Pole Placement Controller with Integrator Design

The system characteristic equation defines the system poles which govern the performance and stability of the system. The idea of pole placement control strategy is to design a controller that manipulates the closed loop poles of the system in order to achieve the desired performance. The continuous time characteristic equation of a closed loop position control system is commonly presented as a second order system as shown in Eq.(5.1).

$$CE(s) = \ s^2 + 2 \cdot \zeta \cdot \omega_n \cdot s + {\omega_n}^2 = 0 \qquad\qquad (5.1)$$

In Eq.(5.1), the system characteristic equation is written in terms of damping ratio, ζ, and natural frequency, ω_n. Then it is convenient to express the damping ratio and natural frequency in the characteristic equation as functions of the desired performance criteria, such as percentage of overshoot, settling time and/or peak time.

The following equations provide the analytical expressions between performance criteria, and damping ratio, ζ, and/or natural frequency, ω_n [7].

$$OS\% = e^{-\left(\frac{\pi \cdot \zeta}{\sqrt{1-\zeta^2}}\right)} \times 100 \tag{5.2}$$

$$T_{set} = \frac{-\ln\left(0.02 \cdot \sqrt{1-\zeta^2}\right)}{\zeta \cdot \omega_n} \tag{5.3}$$

$$T_{peak} = \frac{\pi}{\omega_n \cdot \sqrt{1-\zeta^2}} \tag{5.4}$$

where $OS\%$ is the percentage of overshoot, T_{set} is the settling time in seconds, and T_{peak} is the peak time in seconds.

The system desired characteristic equation in continuous time domain, $CE_{sd}(s)$, is expressed in a general form as shown in Eq.(5.5).

$$CE_{sd}(s) = s^2 + 2 \cdot \zeta_{sd} \cdot \omega_{sd} \cdot s + \omega_{sd}^2 = 0 \tag{5.5}$$

where ω_{sd} is the desired natural frequency and ζ_{sd} is the desired damping ratio.

Recall the derived motor equation of motion in Chapter 4. The system is rewritten in the continuous time state space model form shown in Eq.(5.6) and Eq.(5.7).

$$\dot{X}_1(t) = A_{1s} \cdot X_1(t) + B_{1s} \cdot u(t) \tag{5.6}$$

$$y_1(t) = C_{1s} \cdot X_1(t) + D_{1s} \cdot u(t) \tag{5.7}$$

where,

$$\dot{X}_1(t) = \begin{Bmatrix} \ddot{x}_1(t) \\ \dot{x}_1(t) \end{Bmatrix} \quad X_1(t) = \begin{Bmatrix} \dot{x}_1(t) \\ x_1(t) \end{Bmatrix} \quad u(t) = V_{in}(t) \quad y_1(t) = \{x_1(t)\}$$

$$A_{1s} = \begin{bmatrix} -\dfrac{b_1}{m_t} & 0 \\ 1 & 0 \end{bmatrix} \quad B_{1s} = \begin{bmatrix} \dfrac{K_a \cdot K_t}{m_t} \\ 0 \end{bmatrix} \quad C_{1s} = \begin{bmatrix} 0 & 1 \end{bmatrix} \quad D_{1s} = 0$$

Since the command signal is digitised through the analog to digital converter, the continuous time state space model should be discretised.

The discrete equivalent state space model as shown in Figure 5.1 includes the open loop system dynamics equation, Eq.(5.8), and output equation, Eq.(5.9). The detail discretisation calculation is available in Appendix A.

$$X_1(k + 1) = A_{1z} \cdot X_1(k) + B_{1z} \cdot u(k) \tag{5.8}$$

$$y_1(k) = C_{1z} \cdot X_1(k) \tag{5.9}$$
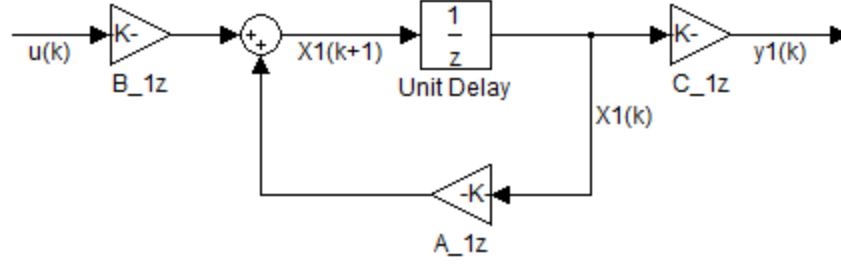
Figure 5.1: Open Loop System State Space Model

$X_1(k)$: States (Motor Velocity and Position)

$y_1(k)$: Measured Output (Motor Position)

For the controller design, it is desired that the controlled system output, $y_1(k)$, tracks the reference input signal, $r(k)$, with zero steady state error. The first step is to define a new state $x_{1i}(k)$ that is the integral of the error between the reference and the output of the system as shown in Eq.(5.10).

$$x_{1i}(k + 1) = x_{1i}(k) + T_s \cdot \big(r(k) - y_1(k)\big) \tag{5.10}$$

It is important that the integration state, $x_{1i}(k)$, reaches steady state when the input signal to the integrator goes to zero.

Now, there is an extra dynamics equation describing the error in the system. Augment the integration state from Eq.(5.10) into the original dynamics equation to form the new open loop state space model as shown in Eq.(5.11) and Eq.(5.12).

$$X_{1_n}(k + 1) = A_{1z_n} \cdot X_{1_n}(k) + B_{1z_n} \cdot u(k) + E_{1z_n} \cdot r(k) \tag{5.11}$$

$$y_1(k) = C_{1z_n} \cdot X_{1_n}(k) \tag{5.12}$$

where,

$$X_{1_n}(k) = \begin{bmatrix} X_1(k) \\ x_{1i}(k) \end{bmatrix} \quad A_{1zn} = \begin{bmatrix} A_z & 0 \\ -T_s \cdot C_z & 1 \end{bmatrix} \quad B_{1zn} = \begin{bmatrix} B_z \\ 0 \end{bmatrix}$$

$$E_{1zn} = \begin{bmatrix} 0 \\ T \end{bmatrix} \quad C_{1zn} = [C_z \quad 0]$$

The new open loop state space model, including an integral state, can be stabilized through performing a full state feedback control since both velocity and position state are accessible from measurement in this experimental setup. The control law is defined as shown in Eq.(5.13).

$$u(k) = -K_n \cdot X_{1_n}(k) = -[K \quad K_i] \begin{bmatrix} X_1(k) \\ x_{1i}(k) \end{bmatrix} \tag{5.13}$$

where K is the controller gain and K_i is the integrator gain.

In the presence of the system controller, the closed loop dynamics equation is rewritten in Eq.(5.14).

$$X_{1_n}(k + 1) = \left[A_{1zn} - B_{1zn} \cdot K_n\right] \cdot X_{1_n}(k) + E_{1zn} \cdot r(k) \tag{5.14}$$

The new discrete time state matrix, A_{1zn}, and the new discrete time input matrix, B_{1zn}, are fixed system parameters, and the controller, K_n, is the only adjustable parameter. The controller parameter, K_n, is adjusted to manipulate the new system characteristic equation, $CE_{is}(z)$, to match with the new system desired characteristic equation,

$CE_{isd}(z)$, which contains all the system desired closed loop poles including the integrator pole as shown in Eq.(5.15).

$$\det\left(z \cdot I - \left(A_{1z_n} - B_{1z_n} \cdot K_n\right)\right) = CE_{is} = CE_{isd}(z) = 0 \qquad (5.15)$$

This new system desired characteristic equation, $CE_{isd}(z)$, is simply the discretised form of the pre-defined continuous time system desired characteristic equation, $CE_{sd}(s)$ together with the integrator characteristics. The new system desired characteristic equation, $CE_{isd}(z)$, has a general form as shown in Eq.(5.16).

$$CE_{isd}(z) = z^3 + \alpha_{s1} \cdot z^2 + \alpha_{s2} \cdot z + \alpha_{s3} = 0 \qquad (5.16)$$

The second step to ensure the system output, $y_1(k)$, is equal to the reference input, $r(k)$, at steady state, a reference gain, N_r, is introduced to scale the reference input [7]. The controlled input, $u(k)$, with the reference gain, N_r, is shown in Eq.(5.17).

$$u(k) = -K_n \cdot X_{1_n}(k) + N_r \cdot r(k) \qquad (5.17)$$

Then choose N_r with its zero lines on the closed loop integrator pole to reduce the effect of the integrator dynamics in the closed loop system. This ensures the integrator to have slow dynamics because the integrator is meant to have influence at steady state response for reducing the steady state error.

The complete closed loop state space model including the pole placement controller with integrator is shown in Eq.(5.18) and Eq.(5.19).

$$X_{1_n}(k+1) = \left(A_{1z_n} - B_{1z_n} \cdot K_n\right) \cdot X_{1_n}(k) + \left(B_{1z_n} \cdot N_r + E_{1z_n}\right) \cdot r(k) \qquad (5.18)$$

$$y(k) = C_{1z_n} \cdot X_{1_n}(k) \qquad (5.19)$$

5.2.2   Observer Design

The presented full state feedback pole placement controller in the previous section is only feasible when all the states are accessible for feedback control. However, if not all states are available or some of the state measurements have high noise content or poor accuracy, the measurements become unavailable or unreliable for feedback control. In this case, an observer is used to estimate the states for feedback. In this section, the two types of observer, time update (TU) and measurement update (MU), are discussed.

The idea behind the observer is to place the system model in parallel with the actual system and to drive them both with the same input. When the model and actual system both have the same initial state vector, the state estimate generated by the model should track the actual state vector. Nevertheless, there are always uncertainties in the actual system and in practice, without feedback, the state estimate would diverge from the true state. The solution is to use the measurement output, $y_1(k)$, and to compare it with the model's estimated measurement output, $\hat{y}_1(k)$. The difference between the two is then used to correct the state estimate.

5.2.2.1 Time Update Observer

Time update observer acts like a predictor which provides the estimate states at the next sampling instance, $k+1$. According to the TU observer diagram in Figure 5.2, the time update observer equation is obtained as in Eq.(5.20).

Figure 5.2: Time Update Observer Diagram

$y_1(k)$: Measured Output (Motor Position)

$y_{1est}(k)$: TU Estimated Output (Motor Position) $\hat{y}_{1t}$

$X_{1est}(k)$: TU Estimated States $\hat{X}_{1t}$

$$\hat{X}_{1t}(k+1) = A_{1z} \cdot \hat{X}_{1t}(k) + B_{1z} \cdot u(k) + L_p \cdot \left(y_1(k) - C_{1z} \cdot \hat{X}_{1t}(k) \right) \qquad (5.20)$$

where $\hat{X}_{1t}(k)$ is the TU estimated state vector and L_p is the TU observer feedback gain. The TU state estimate error, $\tilde{X}_{1t}(k)$, is defined as in Eq.(5.21). Now, the TU state estimate error dynamics is defined at Eq.(5.22).

$$\tilde{X}_{1t}(k) = X_1(k) - \hat{X}_{1t}(k) \qquad (5.21)$$

$$\tilde{X}_{1t}(k+1) = A_{1z} \cdot \left(X_1(k) - \hat{X}_{1t}(k)\right) - L_p \cdot C_{1z} \cdot \left(X_1(k) - \hat{X}_{1t}(k)\right) \quad (5.22)$$

$$\tilde{X}_{1t}(k+1) = \left(A_{1z} - L_p \cdot C_{1z}\right) \cdot \tilde{X}_{1t}(k) \quad (5.23)$$

Eq.(5.23) describes the state estimate error dynamics as the difference between the actual and estimated state vectors changes over time. Ideally, this error should decay to zero as fast as possible. Thus the poles of the error dynamics system matrix should be set to fast and stable.

Define the desired error dynamics poles, $CE_{od}(z)$ as Eq.(5.24).

$$CE_{od}(z) = z^2 + \alpha_{o1} \cdot z + \alpha_{o2} = 0 \quad (5.24)$$

The actual observer error dynamics poles are stated in the observer characteristic equation, CE_o, which is obtained by Eq.(5.25).

$$\det\left(z \cdot I - \left(A_{1z} - L_p \cdot C_{1z}\right)\right) = CE_o = 0 \quad (5.25)$$

Then the observer characteristic equation, CE_o, should be adjusted to equate with the desired observer characteristic equation, CE_{od}, by selecting an appropriate observer feedback gain, L_p.

$$\det\left(z \cdot I - \left(A_{1z} - L_p \cdot C_{1z}\right)\right) = CE_o = CE_{od}(z) \quad (5.26)$$

Note that L_p has many elements as there are error dynamics poles which means that the poles can be placed anywhere as long as the system is observable through the output, $y_1(k)$. This can be verified by checking the determinant of the observability matrix, Eq.(5.27), does not equal zero. For better observer performance, the observer poles are set to have a faster dynamics than the closed loop system.

$$
O = \begin{bmatrix} C_{1z} \\ C_{1z} \cdot A_{1z} \\ \vdots \\ C_{1z} \cdot A_{1z}{}^{n-1} \end{bmatrix}
\tag{5.27}
$$

5.2.2.2 *Measurement Update Observer*

The measurement update (MU) observer works like a corrector. It provides a state vector estimate at the current sampling instance, k, based on the measurement at k. This type of observer is expected to achieve a better estimate for feedback purpose since it minimizes the delay in the system.

The MU observer design strategy is similar to TU observer design approach. At the current sampling instance, k, the MU observer updates the estimate state using measurement $y_1(k)$ as shown in Eq.(5.28).

$$
\hat{X}_{1m}(k) = \hat{X}_{1t}(k) + L_c \cdot \left(y_1(k) - C_{1z} \cdot \hat{X}_{1t}(k) \right)
\tag{5.28}
$$

where $\hat{X}_{1m}(k)$ is the estimated state vector at k using measurements up to k and L_c is the MU observer feedback gain. To generate the state vector at the next sampling instance, $k + 1$, the whole process goes through the system dynamics equation as shown in Eq.(5.29).

$$\hat{X}_{1t}(k + 1) = A_{1z} \cdot \hat{X}_{1m}(k) + B_{1z} \cdot u(k) \tag{5.29}$$

Note that Eq.(5.29) is similar to the TU observer equation, Eq. (5.20), since the next sampling instance, $k + 1$, estimate is based on measurements up to k only. By substituting the MU estimated state vector, $\hat{X}_{1m}(k)$ from Eq.(5.28) into Eq.(5.29), it becomes obvious in how to relate the current estimator gain, L_c, with the predictive estimator gain, L_p.

$$\hat{X}_{1t}(k + 1) = A_{1z} \cdot \hat{X}_{1t}(k) + B_{1z} \cdot u(k) + A_{1z} \cdot L_c \cdot \left(y_1(k) - C_{1z} \cdot \hat{X}_{1t}(k)\right) \tag{5.30}$$

$$L_p = A_{1z} \cdot L_c \tag{5.31}$$

$$L_c = A_{1z}^{-1} \cdot L_p \tag{5.32}$$

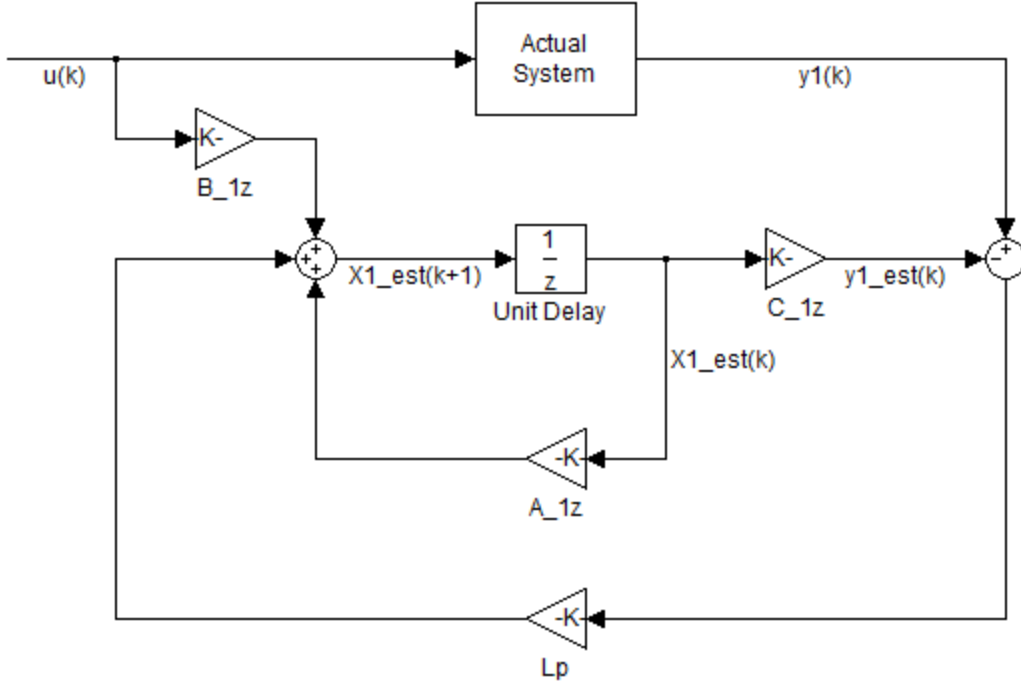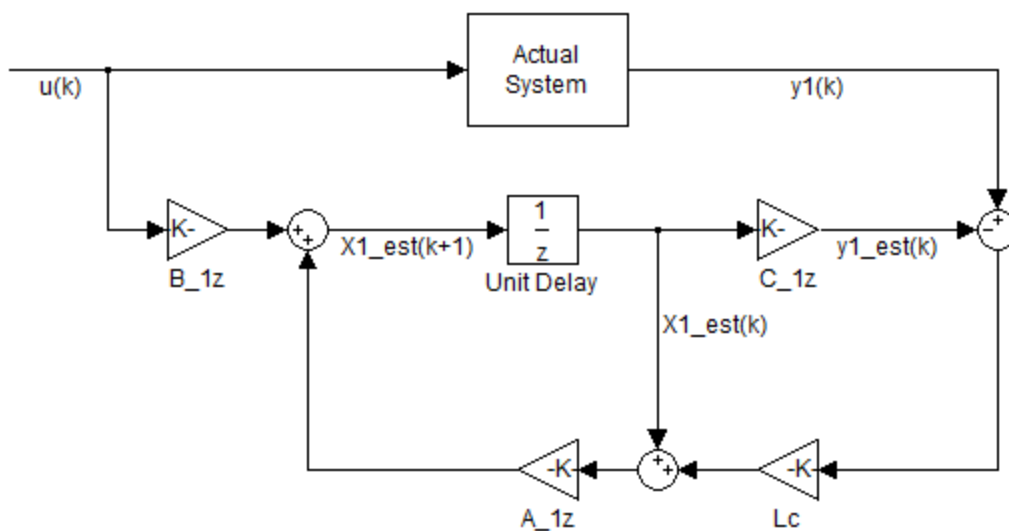Figure 5.3: Measurement Update Observer Diagram

$y_1(k)$: Measured Output (Motor Position)

$y_{1est}(k)$: MU Estimated Output (Motor Position) $\hat{y}_{1m}$

$X_{1est}(k)$: MU Estimated States $\hat{X}_{1m}$

Then the pole placement controller with integrator and measurement update observer are combined as shown in Figure 5.4.

Figure 5.4: Pole Placement Controller with Integrator and Measurement Update Observer

$y_1(k)$: Measured Output (Motor Position)

$y_{1est}(k)$: MU Estimated Output (Motor Position) $\hat{y}_{1m}$

$X_{1est}(k)$: MU Estimated States $\hat{X}_{1m}$

5.2.3   Simulation and Experiment Result

The pole placement controller with integrator is implemented to the linear motor drive. The performance of the positioning control is validated through experiments and simulations. In the experiment, the feedback states to the controller are estimated through the measurement update observer. In the simulation, the average Coulomb

friction identified through the ULS technique and uniformly distributed random noises of ±5 micron from the linear encoder are considered as the system disturbance.
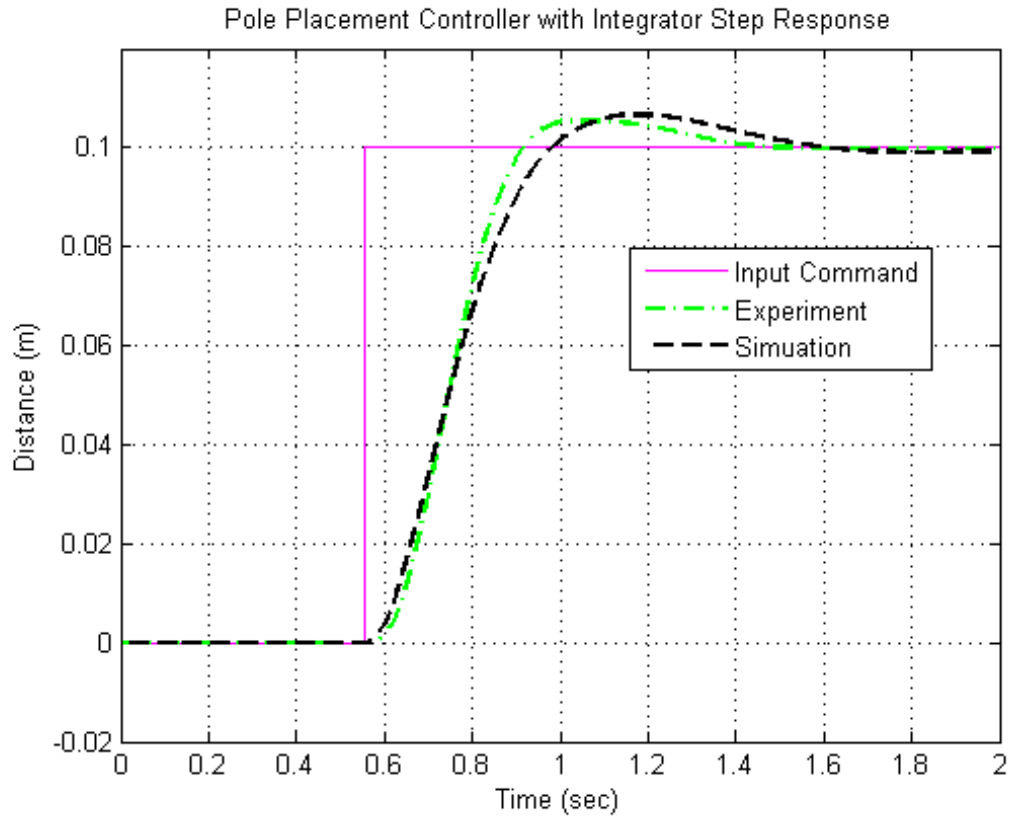
Figure 5.5: Motor Position of Experimental and Simulated Step Response for Motor Position Control System using Pole Placement Controller with Integrator

	Desired	Experiment	Simulation
Overshoot (%)	5.0	5.4	6.7
Setting Time (sec)	0.75	0.77	0.91

Table 5.1: Motor Position of Experimental and Simulated Step Response for Motor Position Control System using Pole Placement Controller with Integrator Summary

The position command step input response experimental and simulated result of the pole placement controller with integrator have been compared. As shown in Figure 5.5, neither of the result meets the desired controller performance criteria because of a number of reasons which are explained as follows. The pole placement controller is designed based on the desired system overshoot percentage and settling time as corresponds with a specified system natural frequency and damping ratio. Then the designed controller manipulates the system poles to obtain the specified system natural frequency and damping ratio in order to meet the design criteria. However, this design approach does not put any disturbance in consideration. Therefore, the addition of disturbance, such as friction force and noise, in the experiment and simulation alters the system performance from the designed model. For better positioning performance, a feedforward controller is recommended for compensating some of the disturbances.

The system model uncertainty is also a contributing factor that causes the experimental and simulated result to be different from the design model. For that same reason, it can be seen that the experimental result does not match with simulated result as well. The experimental result moves much gradually compared to the simulated result. This may be an indication that the Coulomb friction model is not accurate. From Chapter 4, the identified system only considers the linear friction and discards the effect of the nonlinear friction behaviour, which that may underestimate the actual friction in the system. The experimental result shows that the actual system reaches steady state before the simulated system. The reason may be either the actual motor mass is less than the identified motor mass such that the motor is easier to slow down or the actual viscous friction is higher than the model such that the friction force slows down motion of the motor quicker. To improve the simulation accuracy, a more extensive system model should be included in the simulation.

During the experiment, the oscillator acceleration measurement is also captured. The oscillator vibrations continue even after the motor position reaches steady state as shown in Figure 5.6. This vibration is a representation of the machine tool vibration when vibration control is not considered in the controller design. Thus, this causes poor

surface on a machined part. Therefore, this issue leads to the study for vibration control in feed drive system.
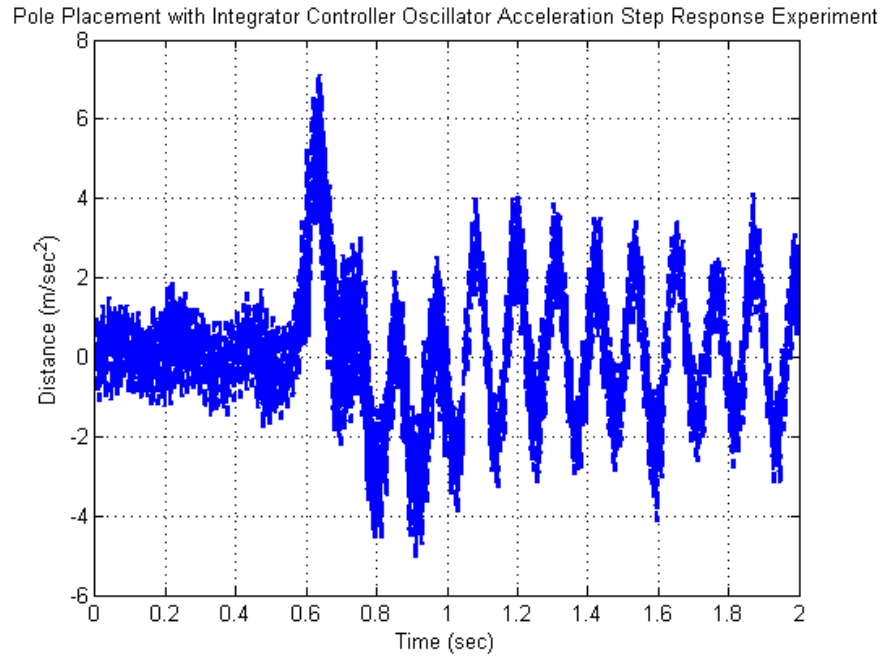
Figure 5.6: Oscillator Acceleration of Experimental Step Response for Motor Position Control System using Pole Placement Controller with Integrator

5.3   Active Vibration Control

In the system without active vibration control, translating the motor position induces vibrations onto the SDOF oscillator which the vibrations persist for a long period of time as shown in the positioning controller experimental result in the previous section. The continuous vibrations deteriorate the accuracy and precision of the machine tool. Therefore, the presented active vibration control is intended to suppress the vibrations at the SDOF oscillator while the motor drive tracks the reference position command accurately.

The presented active vibration control is in a classic cascade control structure where it is divided into the velocity and position loop as shown in Figure 5.7. The velocity loop is designed to minimize the vibrations at the oscillator through the use of a phase compensator. Then a cascaded position controller is applied to track the motor position to its reference command.
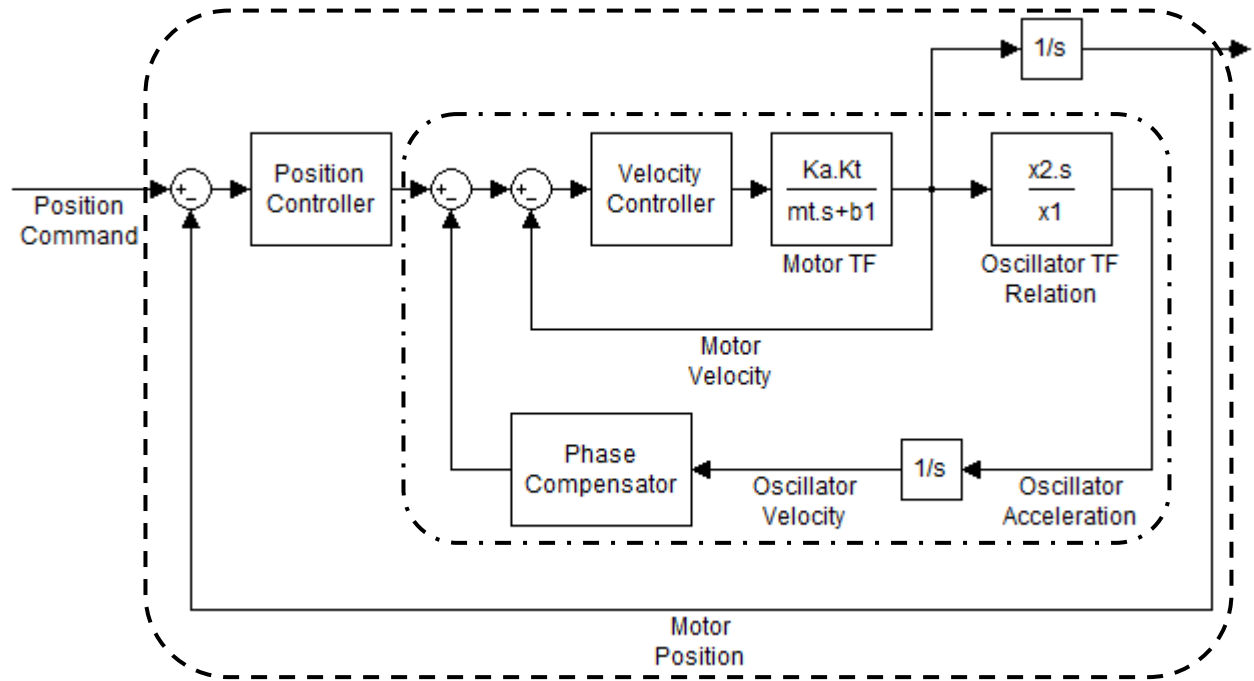
Figure 5.7: Active Vibration Controller with Phase Compensator Design

Velocity Loop (Dash Dot)

Position Loop (Dash)

5.3.1   Velocity Loop Design

To begin the velocity loop design, consider the open loop system in Figure 5.8 and the motor and oscillator velocity frequency response in Figure 5.9 which are derived from the identified transfer functions in Chapter 4.
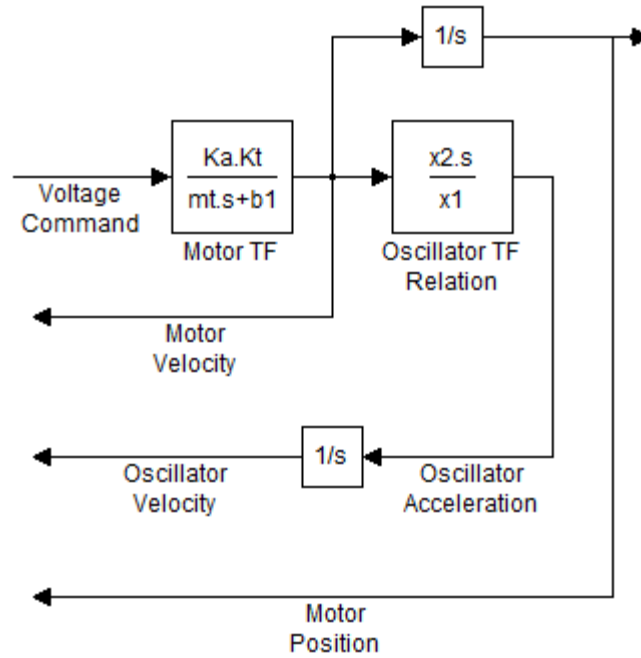
Figure 5.8: Open Loop System
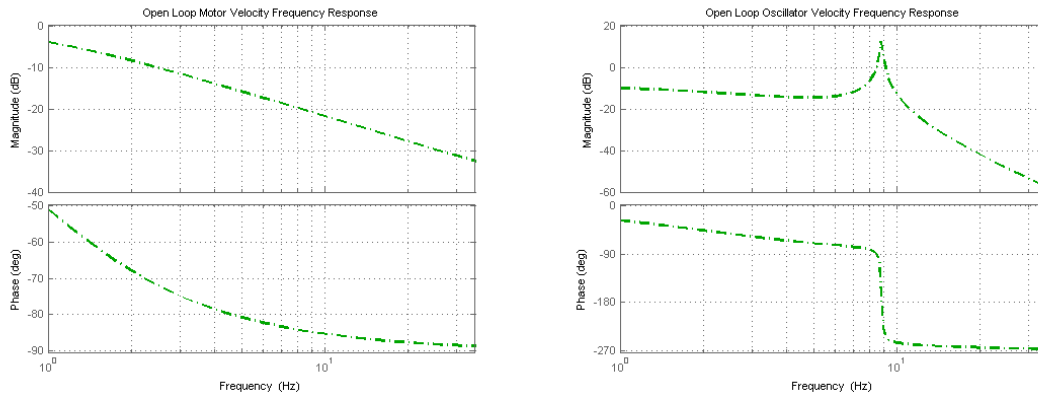
Figure 5.9: Open Loop Motor Velocity (Left) and Oscillator Velocity (Right) Simulated

Frequency Response

In the velocity loop, both motor and oscillator velocity output are used as feedback signals. When only the motor velocity output is used as the feedback, this is known as the indirect velocity loop as shown in Figure 5.10. When both motor velocity and oscillator velocity output are used as the feedback, this is known as the direct velocity

loop. Here, a proportional integral (PI) velocity controller is used to ensure a fast system response with no steady state error in tracking the velocity command.

Proportional Integral (PI) Velocity Controller Parameters	
Proportional Gain: 41.8	Integral Gain: 130.0

Table 5.2: Proportional Integral Velocity Controller Parameters
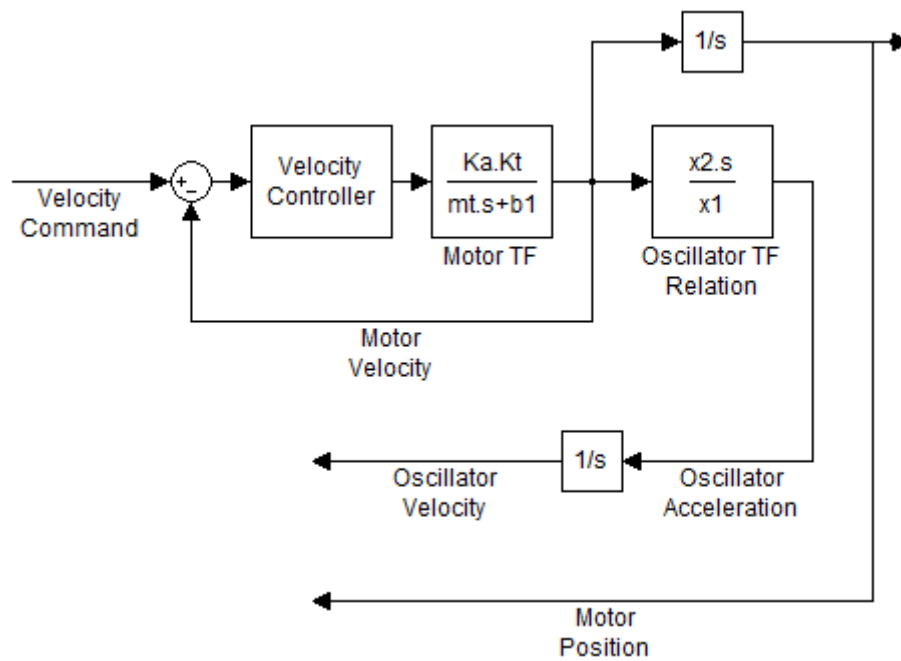
Figure 5.10: Indirect Velocity Loop System
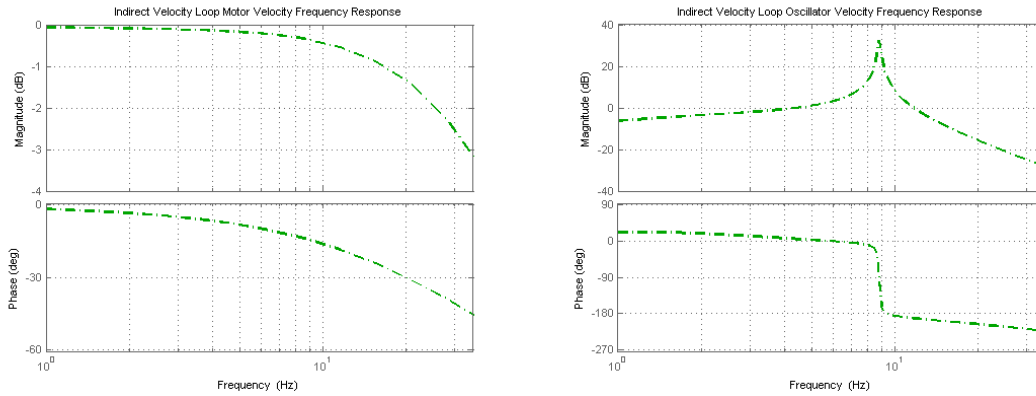
Figure 5.11: Indirect Velocity Loop Motor Velocity (Left) and Oscillator Velocity (Right)

Simulated Frequency Response

The indirect velocity loop oscillator velocity frequency response simulation shown in Figure 5.11 indicates that there is a phase delay of 90 deg at the oscillator resonance. To minimize the oscillator resonant response, a +90 deg phase shift is needed in the direct velocity feedback loop. Therefore, the phase compensator for the direct velocity feedback loop is required to be at unity gain and +90 deg when it crosses the resonance frequency. Then this compensator can be designed in two methods.

The first method is to use a combination of an all pass filter and band pass filter. The band pass filter limits the actuation of the phase compensator to be within the resonant frequency range. Then the all pass filter is a unity filter with a varying phase which is tuned such that the phase of the compensator reaches +90 deg at the oscillator resonant frequency, ω_0.

The second method is the use of the s transfer function with a phase compensator gain of $1/\omega_0$. This method provides the +90 deg phase shift at all frequencies and the constant gain of $1/\omega_0$ ensures the unity gain at the oscillator resonant frequency.

The main issue with the first method is the tuning of the band pass filter and the all pass filter. Since the expected motor positioning operating range is up to 35 Hz, the band pass filter should have a narrow passband which is difficult to achieve with a low order

band pass filter. Then using a high order band pass filter is possible to create a narrow passband but the phase delay of a high order band pass changes quickly across the passband frequency range. Thus, when a slight variation in the resonant frequency occurs, the feedback phase is not guaranteed to be accurate. The feedback without an accurate phase at the resonant reduces the active vibration control performance and defeats the purpose of this phase compensation active control approach.

The second method turns out to be easier to implement. However, there is a minor drawback in this method since the use of s transfer function and the constant phase compensator gain of $1/\omega_0$ can only ensure the unity gain at the resonant frequency, ω_0. This means that when the system operates at frequency range below the resonant frequency, the phase compensator gain is less than unity, and at frequency range above the resonant frequency, the phase compensator gain is greater than unity. Thus, when the system operates at frequency range away from the resonant frequency, the active control may perform worse than the system without active control since the phase compensator gain is either less or greater than unity.

Nonetheless, as shown in simulations, the second method provides a decent active vibration control performance. It is because given the expected operating frequency range up to 35 Hz, the operating range remains close to the natural frequency range. At low frequency operating range as below the resonant frequency, the excitation of the oscillator is relatively low. Thus, the vibrations on flexible structure should be negligible. Then the phase compensator for active vibration control is not crucial. At high frequency operating range as above the resonant frequency, the magnitude of the constant phase compensator gain, $1/\omega_0$, is greater than unity. The feedback signal becomes overly amplified and can cause overshoot in the system. The overly amplified signal can be amended by restraining the maximum feedback signal using a saturation block at the direct velocity feedback loop. Through simulations as shown in Figure 5.13, even without limiting the maximum feedback signal in the direct velocity loop, the overly amplified feedback signal only increases the oscillation velocity frequency response magnitude no more than a couple of decibels compared to the indirect velocity

feedback system at high frequency range. To summarize the earlier discussion, as long as the system operating frequency range is close to the resonance frequency range of the oscillator, the constant compensator gain is reasonable to apply in the active vibration control system.

The result of indirect and directive velocity loop with phase compensator velocity frequency response simulation is compared in Figure 5.13.
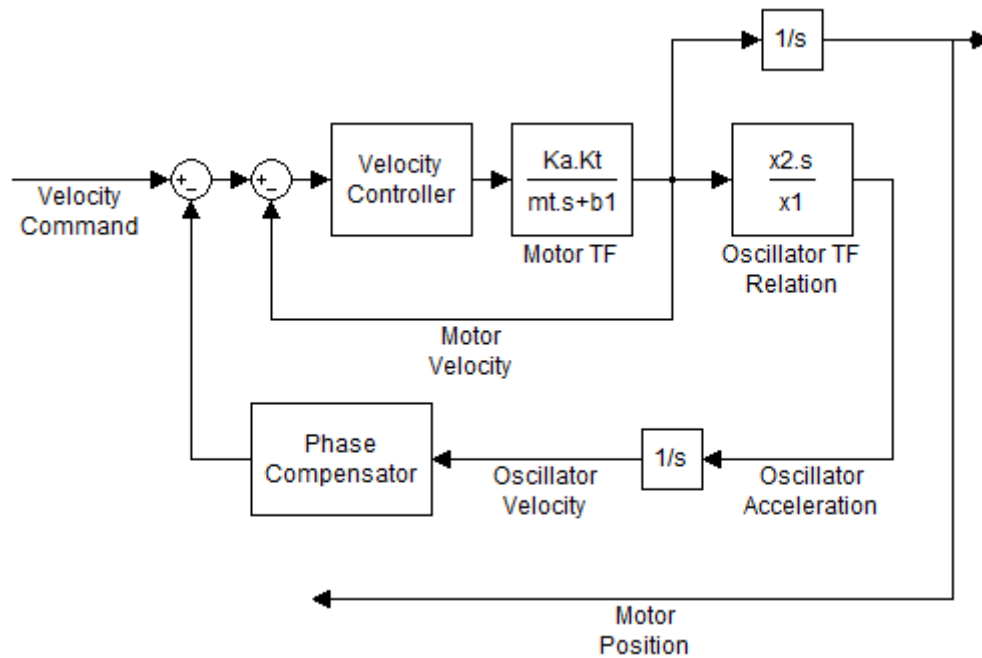
Figure 5.12: Direct Velocity Loop System with Phase Compensator
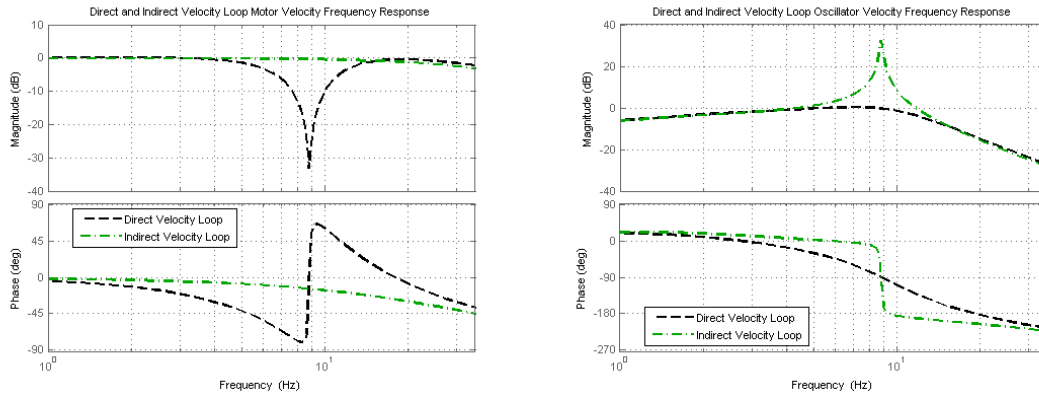
Figure 5.13: Direct and Indirect Velocity Loop Motor Velocity (Left) and Oscillator Velocity (Right) Simulated Frequency Response

Since the motor and oscillator velocity are not direct measurable quantities in this experimental setup, it is much useful to look at the motor position and oscillator acceleration frequency response as shown in Figure 5.14.
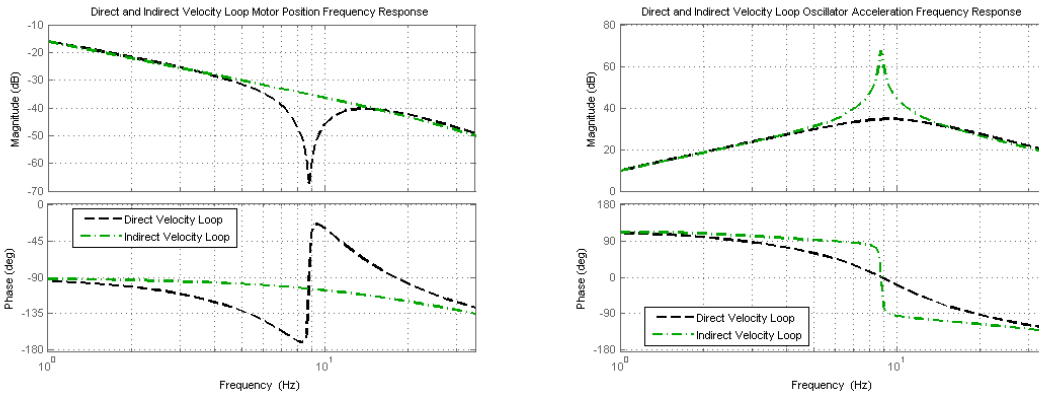
Figure 5.14: Direct and Indirect Velocity Loop Motor Position (Left) and Oscillator Acceleration (Right) Simulated Frequency Response

It should also be noted that when the system has multiple modes, the use of band pass filter at the resonant frequency, ω_0, ensures that the phase compensation is being

active only around the vibration mode at ω_0 and decouples the control effort to other vibration modes [19]. The band pass filter implementation is also useful to minimize the drawback of using a constant phase compensator gain as previously described. It is because when the system is operating away from the resonant frequency, the effect of the improper amplified feedback signal is limited. For this experimental setup, since only the first resonance mode is considered for active vibration control, the use of band pass filter is not necessary.

5.3.2   Position Loop Design

With the completion of the velocity loop design, a cascaded position controller is implemented to close the position loop as shown in Figure 5.15. The motor position negative loop transmission (NLT) frequency response simulation shown in Figure 5.16 indicates that the anti-resonant introduced by oscillator dynamic response may impose challenges to the position controller design.
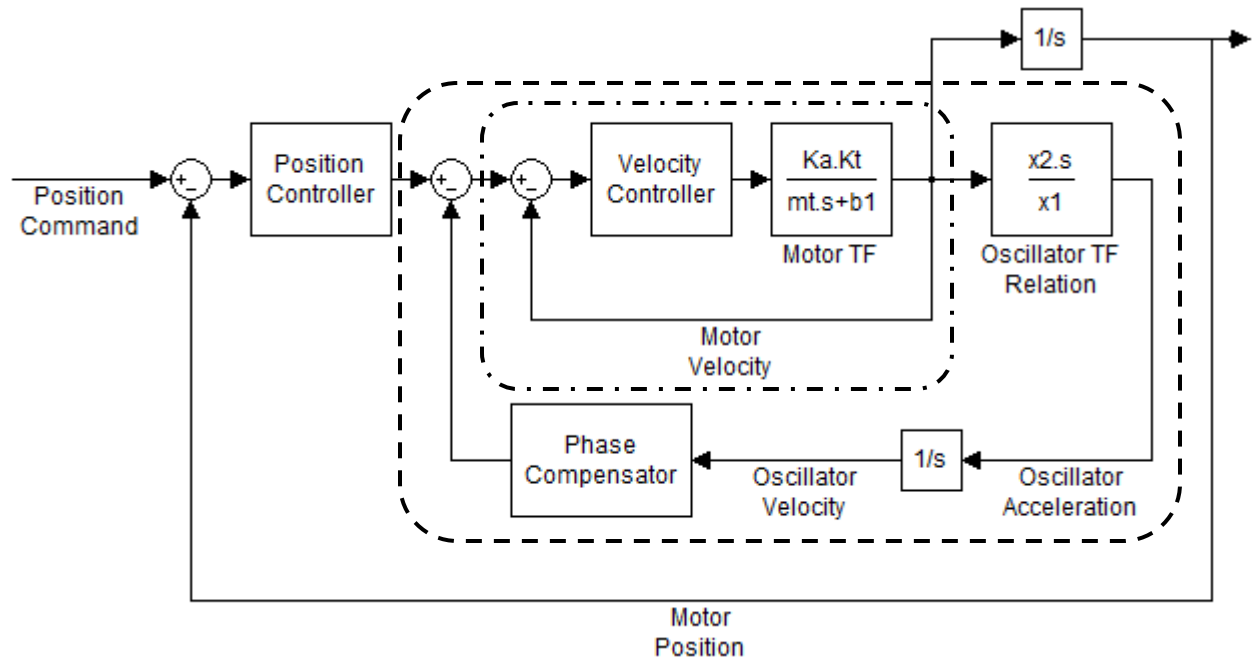
Figure 5.15: Cascaded Position Loop with Velocity Loop

Indirect Velocity Loop (Dash Dot)

Direct Velocity Loop (Dash)
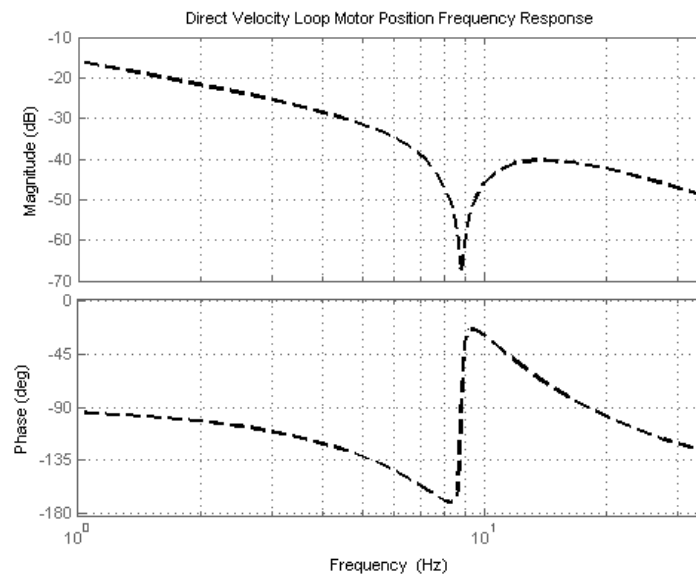
Figure 5.16: Direct Velocity Loop Motor Position Simulated Frequency Response

At first, a loop shaping controller is designed to set the motor positioning bandwidth above the anti-resonant frequency and increase the phase margin to be at least 60 deg to ensure stability. This is not possible due to the rapid phase change between the two phase extrema across the anti-resonant frequency. The minimum phase must be increased to -120 deg in order to satisfy the +60 deg of phase margin. However, this leads to the loop shaping controller shifting the maximum phase above 0 deg, where the system becomes unstable.

Instead, a proportional position controller is applied. In theory, a high proportional gain position controller can increase the motor positioning bandwidth above the anti-resonant frequency. However, the phase margin is less than 60 deg near the anti-resonant frequency, which the system can easily become unstable. Therefore, it is best to avoid extending the motor positioning bandwidth above the anti-resonant frequency. Now, the system bandwidth is limited by the anti-resonant behaviour since the motor position frequency response drops rapidly at that frequency range.

In practice, another limitation must put into consideration which is the motor drive saturation. Thus, an appropriate proportional gain position controller is implemented to obey the motor drive saturation requirement.

The motor position and oscillator acceleration frequency response simulation in closed position loop are shown in Figure 5.17. The system with direct velocity loop is denoted as an active control system and the system with only indirect velocity loop, equivalently as without direct velocity loop, is denoted as a non active control system.

Figure 5.17: Motor Position (Left) and Oscillator Acceleration (Right) Simulated

Frequency Response for Active and Non Active Vibration Control System

The disturbance force, which considered as Coulomb friction and external applied force, are included in the active control system as shown in Figure 5.18. The Coulomb friction is working against the motor force, and the external applied force is applied at the flexible oscillator. An addition feed forward controller can be used to compensate for the Coulomb friction, since it has been identified in the parameter identification process. The disturbance frequency responses are derived as shown in Figure 5.19. For the non active control system, it is assumed that motor position is not affected by the excitation applied at the oscillator. Thus, the disturbance frequency response has zero magnitude and does not appear on the motor position disturbance frequency response.
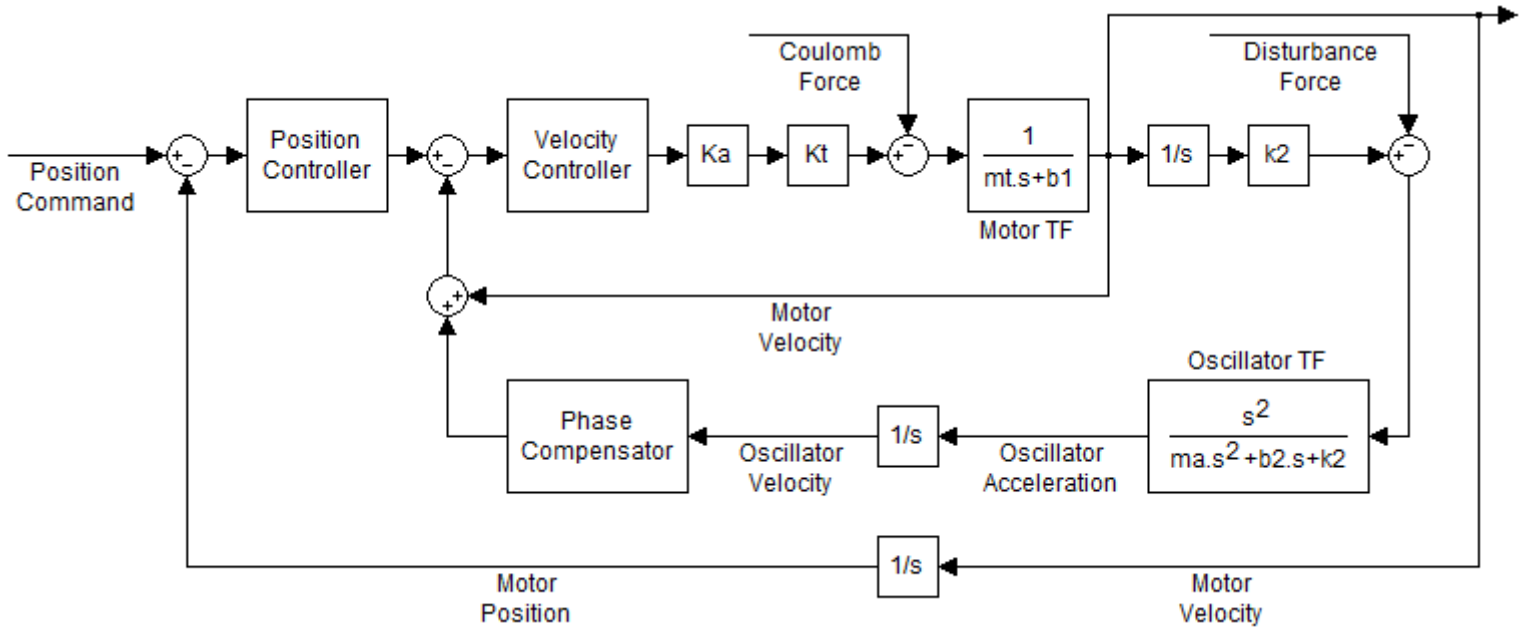
Figure 5.18: Active Control System with Disturbance Input
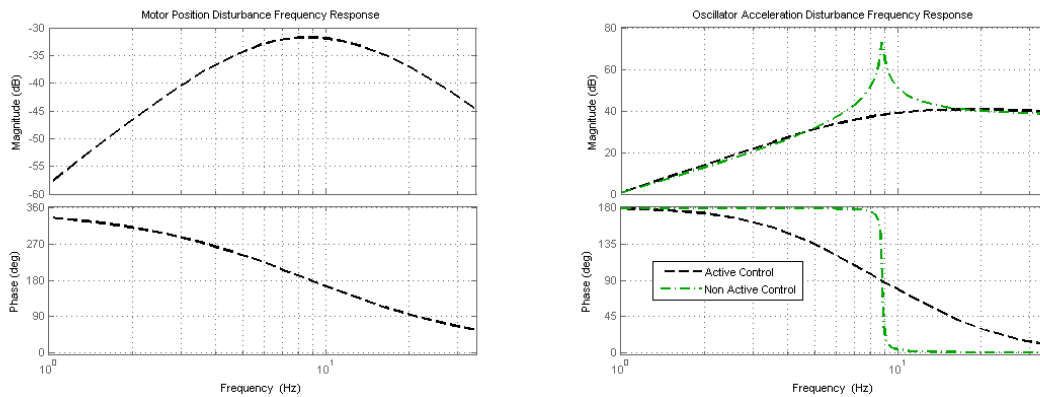
Figure 5.19: Motor Position (Left) and Oscillator Acceleration (Right) Simulated
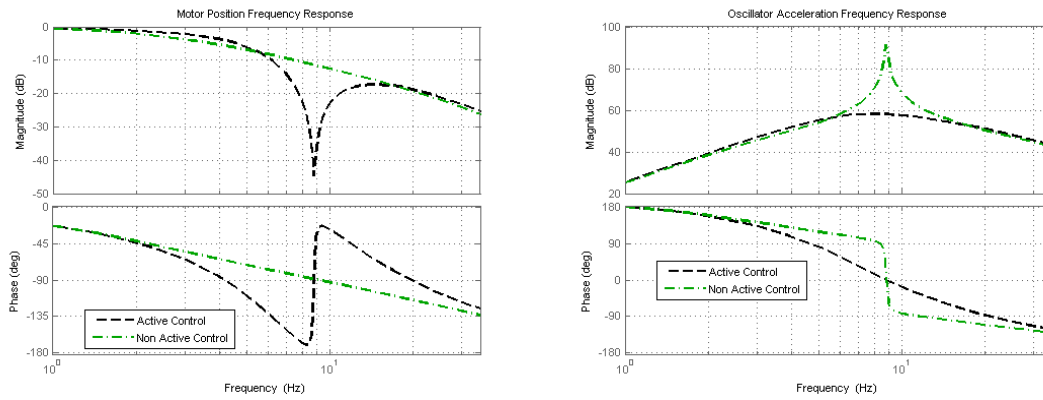
Disturbance Frequency Response for Active and Non Active Vibration Control System

5.3.3   Modification in Experimental Implementation

Two types of sensor used to measure the system feedback: linear encoder for motor

position, and accelerometer for oscillator acceleration. Since the linear encoder is a high

accuracy sensor, the velocity measurement obtained by taking the difference in positions per sampling time is reliable as a feedback signal in the indirect velocity loop. On the other hand, the accelerometer's high noise and DC offset cause the accelerometer measurement to be undesirable as a feedback signal in the direct velocity loop. The accelerometer noisy feedback is amplified through velocity controller which constantly saturates the motor drive power. Because the oscillator velocity cannot be measured directly, the accelerometer measurement must be numerically integrated to obtain the velocity measurement. The problem comes in when taking the numerical integration of the accelerometer signal with a DC offset, this causes the derived oscillator velocity signal to drift. Thus, the derived oscillator velocity signal becomes unsuitable as a feedback signal in the direct velocity feedback loop. For these reasons, modifications are made to overcome the two implementation challenges.

5.3.3.1 Feedback Simplification

The accelerometer must be fastened securely at the tip of the SDOF oscillator. However, the holding force of the senor may have transmitted to the sensor itself. Thus, the accelerometer picks up a small offset signal. By taking the numerical integration of the accelerometer DC offset signal introduces a drift into the derived oscillator velocity signal. The solution to overcome this challenge is to avoid taking numerical integration of the accelerometer signal. The reason for numerically integrating the acceleration signal is to convert the acceleration signal to velocity signal used in the direct velocity loop feedback. It is because the direct velocity feedback signal needs to go through a +90 deg phase shift by an s transfer function at the phase compensator. This phase shift processed by an s transfer function is equivalent to processing the signal by a differentiation operation. Now, this can be seen that these two processes are actually redundant operations which cancel each other. Therefore, modification can be made by cancelling the numerical integration with the phase shift operation, and simply scaling the acceleration signal with the phase compensator gain of $1/\omega_0$ as the phase

compensated direct velocity feedback signal. Then the accelerometer sensor's DC offset no longer causes the feedback signal to drift. For comparison, the original and modified direct velocity loop are shown in Figure 5.20 and Figure 5.21, respectively.
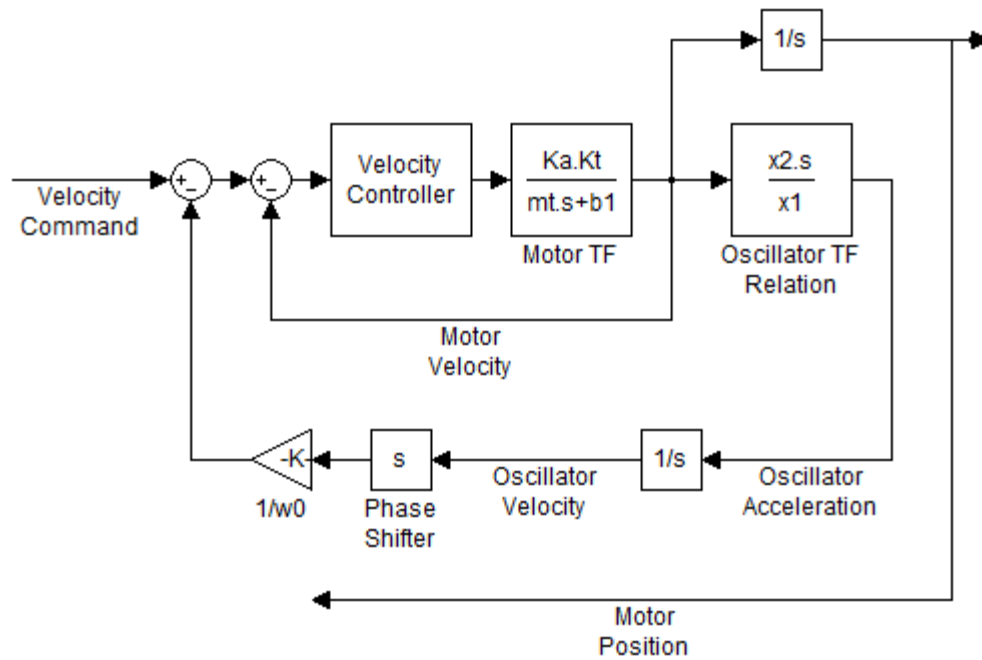
Figure 5.20: Original Direct Velocity Loop
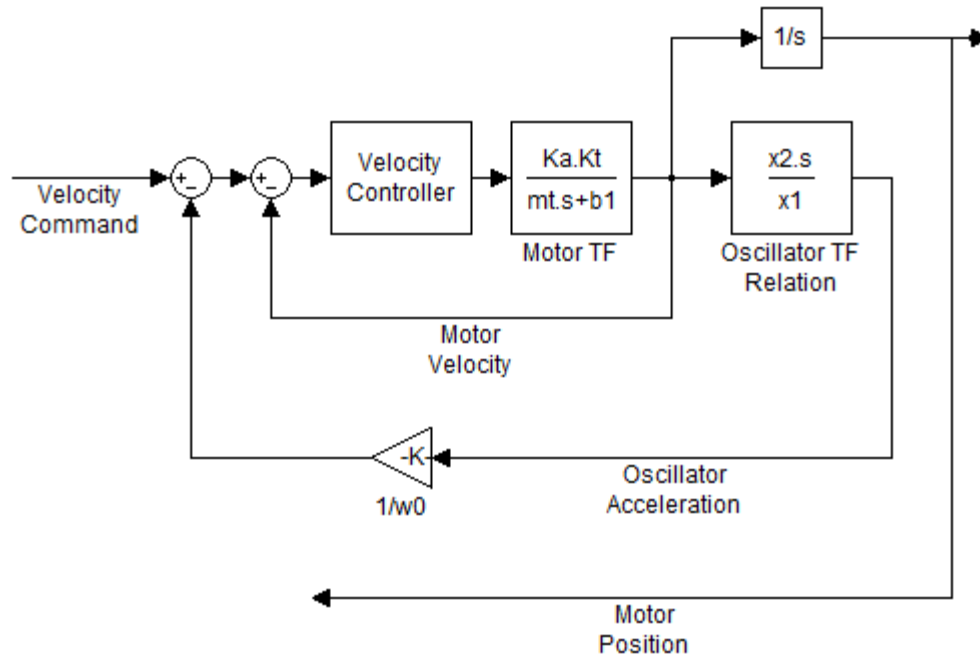
Figure 5.21: Modified Direct Velocity Loop

5.3.3.2 Kalman Filter

Another implementation issue is due to the accelerometer noisy measurement signal used in the direct velocity feedback loop. The amplified noisy measurement signal can easily saturate the motor drive power which causes the motor to overheat. The initial attempt is by applying a low pass filter to remove the high frequency measurement noise. However, using a high cut off frequency low pass filter cannot remove most of the noise, but using a low cut off frequency low pass filter introduces an undesirable phase delay at the feedback signal. The feedback signal with the addition phase delay deteriorates the active vibration control performance. To remove the noise at the accelerometer signal without scarifying the active vibration control performance, the Kalman filter is implemented.

The Kalman Filter algorithm developed by R. Kalman is a recursive filter using measurements containing sensor noise and other inaccuracies to estimate the states of a linear system in time domain. The filter is applied to the states of a discretised system

to estimate the new states at each discrete time increment. The two independent types of noise considered are measurement noise and process noise. Measurement noise is introduced at the system output and caused by poor measurement sensors. The process noise is introduced at the system input and caused by model uncertainty. Through the Kalman filter algorithm, the filter produces a priori state estimate at sampling instance k given knowledge of the process prior to sampling instance k, and a posteriori state estimate at sampling instance k given measurement at sampling instance k with weighted average, and computes the uncertainty of the estimates. The weight of the weighted average is distributed between the estimate value through the time update process and measurement update process. More weight is given to the value with lesser uncertainty. The estimate produced by the filter tends to be more accurate than the original measurements because the weighted average value has a better estimated uncertainty than either of the values that went into the weighted average.

The Kalman filter estimates a process by using a form of feedback control. The filter estimates the process state at each sampling instance and then obtains feedback in the form of noisy measurements. As such, the Kalman filter algorithm is categorised into two processes, time update and measurement update. The time update process is responsible for projecting forward the current state and error covariance estimates to obtain the a priori estimates for the next sampling instance, $k + 1$. The measurement update process is responsible for the feedback for incorporating a new measurement into the a priori estimate to obtain an improved a posteriori estimate. The time update equations can also be thought of as predictor equations, while the measurement update equations can be thought of as corrector equations.

The motor position and oscillator acceleration transfer function are converted into discrete time state space system with the consideration of the process noise, R_w, and measurement noise, R_v. The detail calculation of converting the transfer functions into discrete time state space system is given in Appendix A. The discrete time state space system model is represented by the dynamics and output equation as shown in Eq.(5.33) and Eq.(5.34), respectively.

$$X(k + 1) = A_z \cdot X(k) + B_z \cdot u(k) + R_w(k) \tag{5.33}$$

$$y(k) = C_z \cdot X(k) + R_v(k) \tag{5.34}$$

The process and measurement noise are assumed to be zero mean Gaussian white noise. The noise matrices are defined as the expected values of the corresponding noise vectors described mathematically by Eq.(5.35) and Eq.(5.36).

$$Q = E[R_w \cdot R_w{}^T] \tag{5.35}$$

$$R = E[R_v \cdot R_v{}^T] \tag{5.36}$$

where Q and R are the covariance matrices of the process and measurement noise, respectively. Note that R_w and R_v are mutually independent, then the expected value of R_w and R_v is zero.

$$0 = E[R_w \cdot R_v{}^T] \tag{5.37}$$

The Kalman filter performs the estimation in a predictor-corrector approach with time and measurement update. With the given system model, the a priori state estimate vector, $\hat{X}_{k+1|k}(k + 1)$, at the next sampling instance is computed based on the a posteriori state estimate, $\hat{X}_{k|k}(k)$, at the current sampling instance through the time update equation as show in Eq.(5.38).

$$\hat{X}_{k+1|k}(k+1) = A_z \cdot \hat{X}_{k|k}(k) + B_z \cdot u(k) \tag{5.38}$$

where $u(k)$ is the known system input.

The residual, R_{res}, is defined as the difference between the sensor measurement, $y(k)$, and a priori output estimate, $C_z \cdot \hat{X}_{k|k-1}(k)$, as shown in Eq.(5.39). The residual reflects the discrepancy between the a priori output estimate and the actual output measurement. When the residual, R_{res}, reaches zero, the output estimate equals to the actual output.

$$R_{res}(k) = y(k) - C_z \cdot \hat{X}_{k|k-1}(k) \tag{5.39}$$

The measurement update equation uses the a priori state estimate, $\hat{X}_{k|k-1}(k)$, at the current sampling instance k obtained at the previous sampling instance, $k-1$, and with the weighted average residual as a correction term to compute the a posteriori state estimate, $\hat{X}_{k|k}(k)$ as shown in Eq.(5.40).

$$\hat{X}_{k|k}(k) = \hat{X}_{k|k-1}(k) + K_k \cdot R_{res}(k) \tag{5.40}$$

where K_k is the weighted average Kalman gain.

The Kalman gain is defined for minimizing the a posteriori estimate error covariance and thus an accurate estimation of the system states can be achieved. The a priori and a posteriori estimate error are defined as in Eq.(5.41) and Eq.(5.42), respectively.

$$e_{k|k-1} \equiv X - \hat{X}_{k|k-1} \tag{5.41}$$

$$e_{k|k} \equiv X - \hat{X}_{k|k} \tag{5.42}$$

Then the a priori and a posteriori estimate error covariance are as shown in Eq.(5.43) and Eq.(5.44).

$$P_{k+1|k} = E\left[e_{k+1|k} \cdot e_{k+1|k}{}^T\right] \tag{5.43}$$

$$P_{k|k} = E\left[e_{k|k} \cdot e_{k|k}{}^T\right] \tag{5.44}$$

Referring to [12], the resulting function for the Kalman gain is as show in Eq.(5.45).

$$K_k = P_{k|k-1} \cdot C_z{}^T \cdot \left(C_z \cdot P_{k|k-1} \cdot C_z{}^T + R\right)^{-1} \tag{5.45}$$

At Eq.(5.45), as the measurement error covariance, R, approaches zero, the Kalman gain, K_k, weights the residual more heavily as shown in Eq.(5.46).

$$\lim_{R \to 0} K_k = C_z{}^{-1} \tag{5.46}$$

On the other hand, as the a priori estimate error covariance, $P_{k+1|k}$, approaches zero, the Kalman gain, K_k, weights the residual less heavily as shown in Eq.(5.47).

$$\lim_{P_{k+1|k} \to 0} K_k = 0 \tag{5.47}$$

Another way of thinking about the weighting by the Kalman gain, K_k, is that as the measurement error covariance, R, approaches zero, the actual output measurement, $y(k)$, is trusted more, while the a priori output estimate, $C_z \cdot \hat{X}_{k|k-1}(k)$, is trusted less. In contrary, as the a priori estimate error covariance, $P_{k|k-1}$, approaches zero the actual output measurement, $y(k)$, is trusted less, while the a priori output estimate, $C_z \cdot \hat{X}_{k|k-1}(k)$, is trusted more.

The minimized a priori estimate error covariance is as shown in Eq.(5.48),

$$P_{k+1|k} = A_z \cdot P_{k|k} \cdot A_z{}^T + Q \tag{5.48}$$

and the minimized a posteriori estimate error covariance is as shown in Eq.(5.49).

$$P_{k|k} = (I - K_k \cdot C_z) \cdot P_{k-1|k} \tag{5.49}$$

Figure 5.22 provides an overview of the Kalman filter operation cycle. At first, the initial state and error covariance are predefined in the filter. Then the time update projects the current state estimate ahead in time. The measurement update adjusts the projected estimate by an actual measurement at that time. The cycle repeats with time update process and follows again with measurement update process.
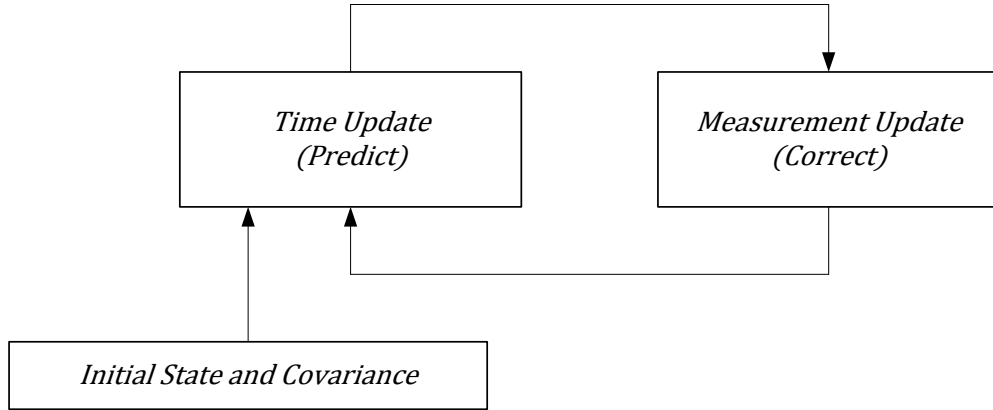
Figure 5.22: Kalman Filter Operation Cycle

Time Update (Predict) Process	
Project the state ahead	$\hat{X}_{k+1\|k}(k+1) = A_z \cdot \hat{X}_{k\|k}(k) + B_z \cdot u(k)$
Project the error covariance ahead	$P_{k+1\|k} = A_z \cdot P_{k\|k} \cdot A_z{}^T + Q$

Table 5.3: Kalman Filter Time Update Process Equations

Measurement Update (Correct) Process	
Compute the Kalman gain	$K_k = P_{k\|k-1} \cdot C_z{}^T \cdot \left(C_z \cdot P_{k\|k-1} \cdot C_z{}^T + R\right)^{-1}$
Update estimate with measurement	$\hat{X}_{k\|k}(k) = \hat{X}_{k\|k-1}(k) + K_k \cdot \left(y(k) - C_z \cdot \hat{X}_{k\|k-1}(k)\right)$
Update the error covariance	$P_{k\|k} = (I - K_k \cdot C_z) \cdot P_{k-1\|k}$

Table 5.4: Kalman Filter Measurement Update Process Equations

The noise level during measurement and the accuracy of sensors together with the modelling uncertainties are essential to the derivation of the noise covariance matrices. In the actual implementation of the filter, the measurement noise covariance, R, is measured prior to operation of the filter. To determine the measurement error

covariance, R, is generally straightforward since it can be done by taking some offline senor measurement.

The determination of the process noise covariance, Q, is more difficult because typically it is not possible to directly observe the estimate process. Nevertheless, a relatively poor process model can still produce an acceptable result if higher uncertainty is injected into the process via the selection of Q.

In general, whether or not a rational approach is possible for determining the noise covariance parameters, strong filter performance statically speaking can be achieved by tuning the filter parameters Q and R.

Thus, for this experimental setup, the measurement noise covariance, R, is set by computing the covariance of the offline accelerometer signal recordings. The process noise covariance, Q, is tuned until the Kalman filter output coincides well with system excitation by input command and exogenous disturbance. When Q is set to too low, the filter output is unable to track exogenous disturbance, and when Q is set to too high, the filter is unable to reduce the sensor noise. The tuned noise covariance parameters are listed in Table 5.5. The accelerometer and Kalman filter measurement update output measurements and comparison summary are shown in Figure 5.23 and Table 5.6, respectively.

R Measurement Noise Covariance $(m/s^2)^2$	Q Process Noise Covariance $(m/s^2)^2$
0.0453	0.0500

Table 5.5: Noise Covariance Parameters
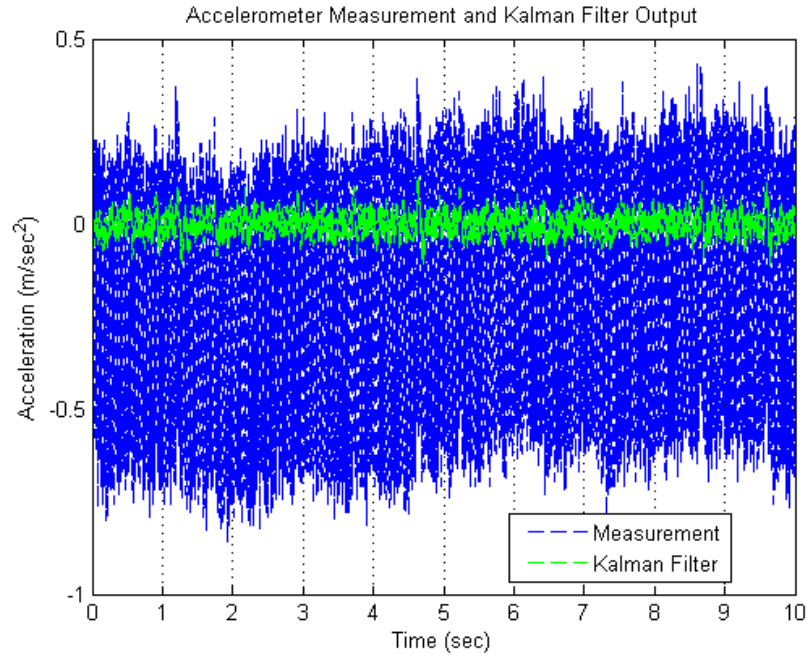
Figure 5.23: Accelerometer Measurement and Kalman Filter Output

Oscillator Acceleration	Accelerometer Measurement	Kalman Filter
Mean (m/s^2)	-0.214	0.000205
Covariance (m/s^2)^2	0.0453	0.00102

Table 5.6: Acceleration Measurement and Kalman Filter Output Summary

The use of Kalman filter has successfully reduced the offset and the covariance of the acceleration signal. With the implementation modifications of feedback simplification and Kalman filter, the active vibration control system has been implemented and operated properly. The accelerometer signal offset and noise no more causes feedback signal drift and saturation to the amplifier.

The complete control system structure with the modifications is shown in Figure 5.24.
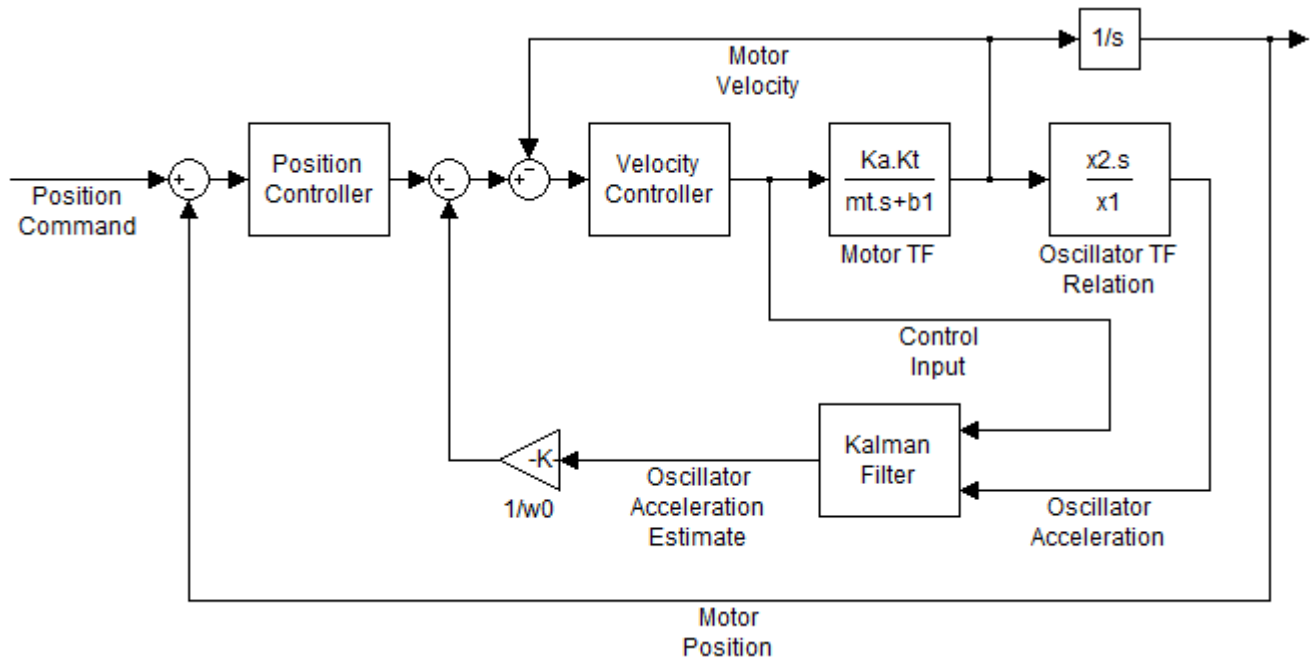
Figure 5.24: Modified Position Loop with Kalman Filter and Feedback Simplification

5.3.4 Simulation and Experiment Result

5.3.4.1 Frequency Response Simulation

Simulations are conducted to compare the motor position and oscillator acceleration frequency response of the active vibration control system with different proportional position controller. The proportional gain magnitudes include 10, 15, 20 and 30 which are denoted by P10, P15, P20 and P30, respectively.
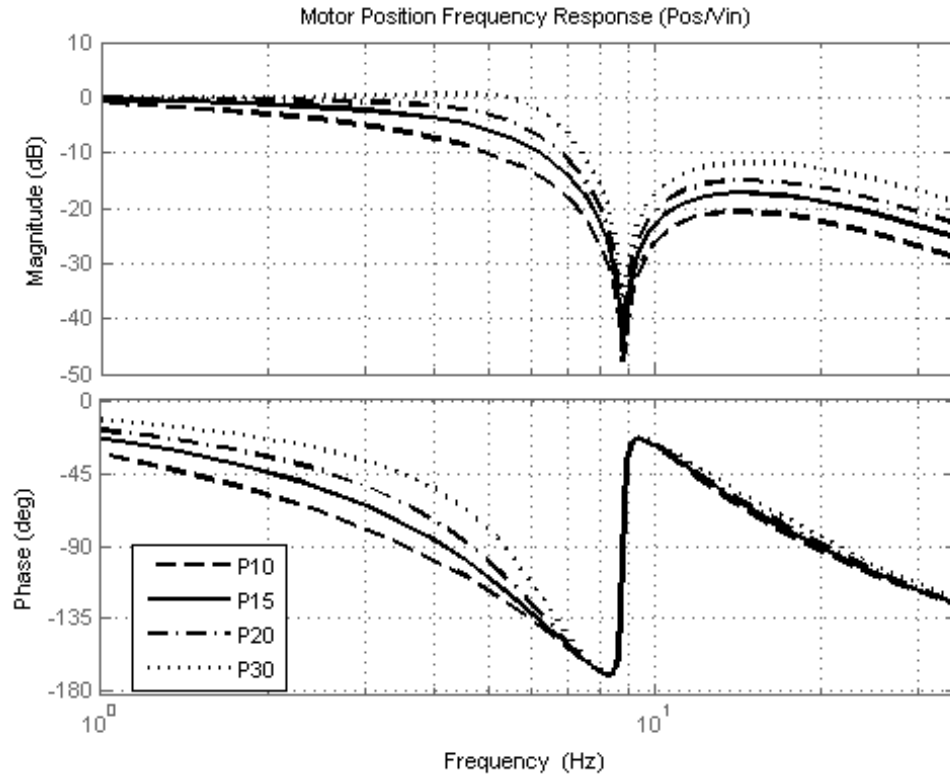
Figure 5.25: Simulated Frequency Response from Motor Position Input Command to Motor Position for Active Vibration Control System with Different Position Controller Proportional Gains

Position Controller Gain	P10	P15	P20	P30
Bandwidth (Hz)	2.0	3.6	5.0	6.4

Table 5.7: Simulated Frequency Response from Motor Position Input Command to Motor Position for Active Vibration Control System in Different Position Controller Proportional Gains Summary

Figure 5.26: Simulated Frequency Response from Motor Position Input Command to Oscillator Acceleration for Active Vibration Control System with Different Position Controller Proportional Gains

Position Controller Gain	P10	P15	P20	P30
Maximum Magnitude (dB)	54.6	58.2	61.2	65.7

Table 5.8: Simulated Frequency Response from Motor Position Input Command to Oscillator Acceleration for Active Vibration Control System with Different Position Controller Proportional Gains Summary

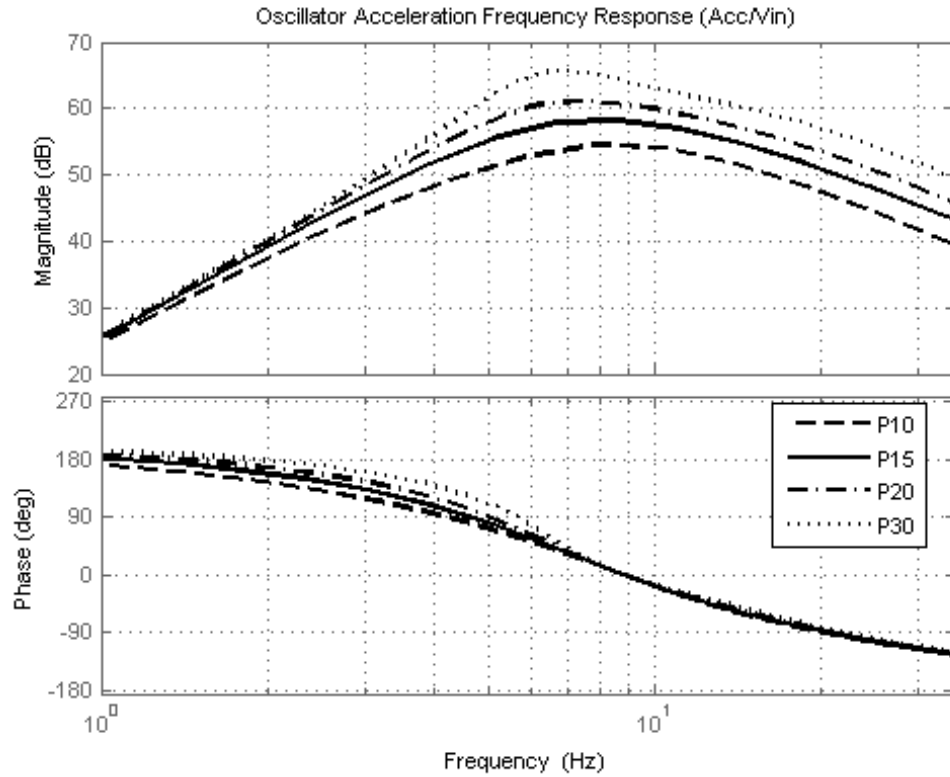With the flexible oscillator dynamics in the direct velocity feedback system, an anti-resonant effect is introduced into the motor position frequency response at the oscillator resonant frequency. The anti-resonant frequency region imposes a great

limitation in extending the motor positioning bandwidth since the motor position frequency response magnitude drops to as much as -50 dB. The anti-resonant effect at the motor position frequency response occurs because the negative oscillator acceleration feedback signal cancels with the position command signal. Thus, there is no control input signal directing into the motor.

For position controller tuning, the motor position frequency response simulation shown in Figure 5.25 indicates that further increase of the proportional gain of the position controller can only provide marginal improvement to the motor positioning bandwidth but at the cost of reducing the active vibration control performance. It is because with a higher proportional gain position controller, the magnitude of the oscillator acceleration frequency response increases as shown in Figure 5.26.

5.3.4.2 Step Response Experiment

The intent of the step response experiment is to replicate the induced vibrations on the machine flexible structure when the machine position is translated. During the experiment, both the motor position and SDOF oscillator acceleration response are measured. Two sets of step response experiment are conducted. The first experiment is comparing the 0.1 m position command step input response of the active vibration control system with different proportional position controllers. The second experiment is comparing the 0.1 m position command step input response of the system with and without active vibration control.

Figure 5.27: Motor Position of Experimental Step Response for Active Vibration Control System

Input: Motor Position Step Input Command

Output: Motor Position

Position Controller Gain	P10	P15	P20	P30
Overshoot (%)	0.3	2.3	11.5	23.5

Table 5.9: Motor Position of Experimental Step Response for Active Vibration Control System Summary

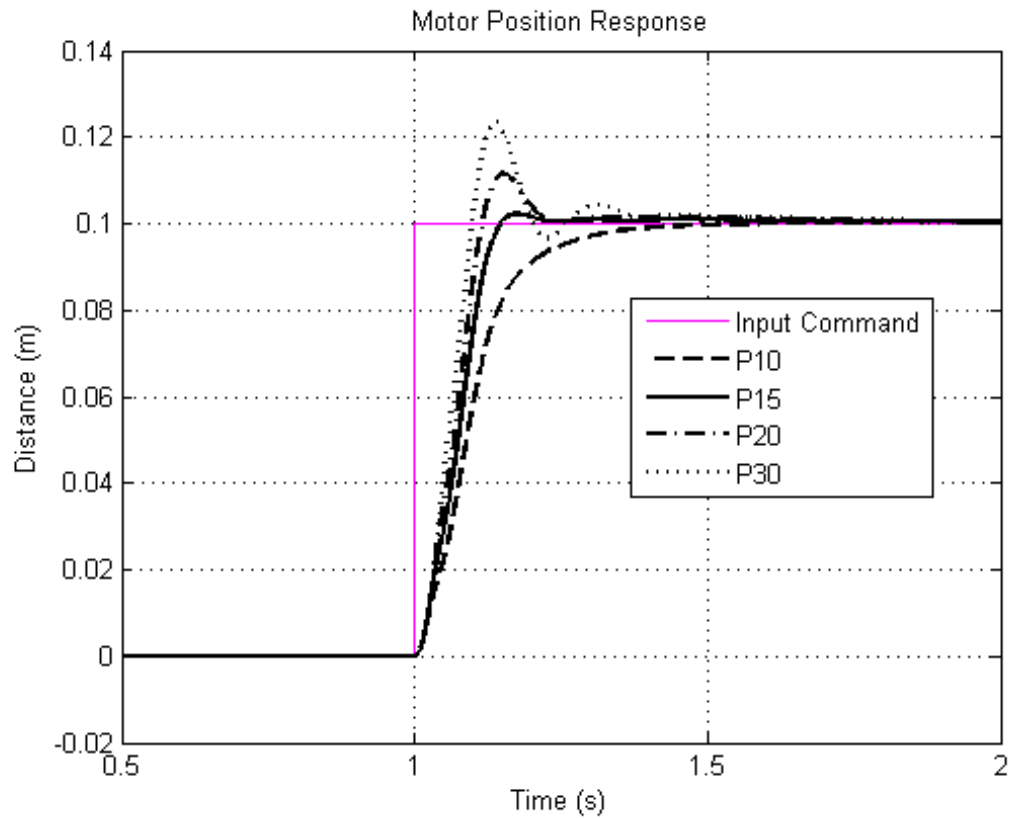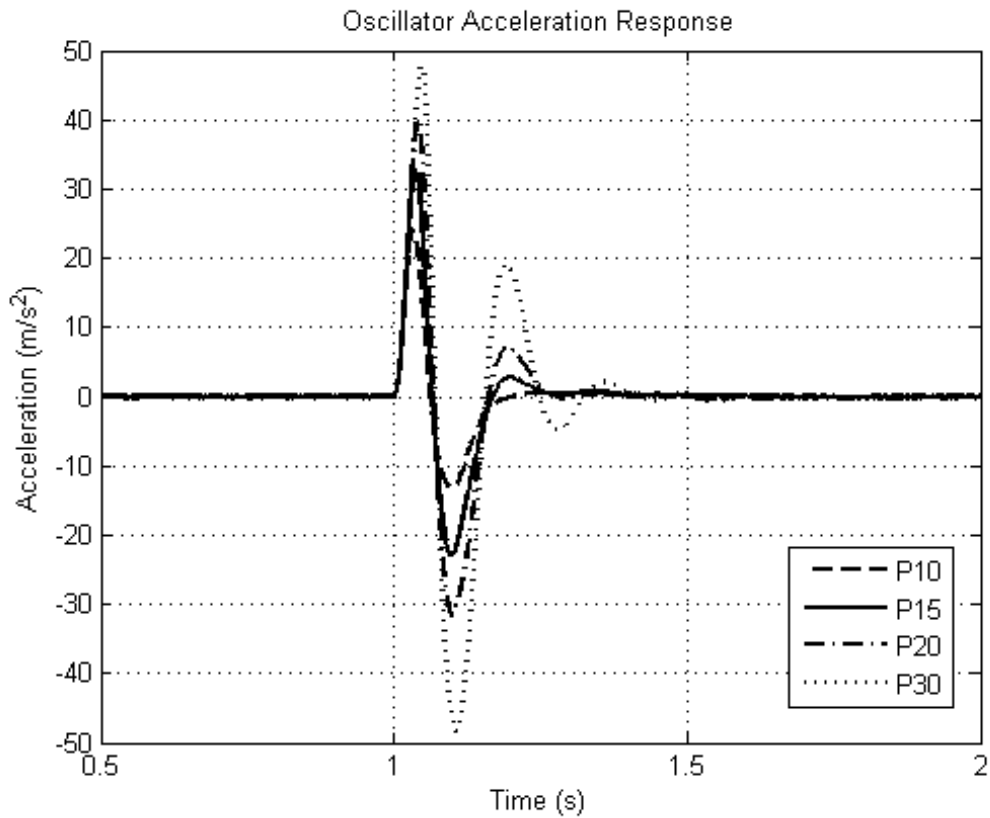Figure 5.28: Oscillator Acceleration of Experimental Step Response for Active Vibration

Control System

Input: Motor Position Step Input Command

Output: Oscillator Acceleration

Position Controller Gain	P10	P15	P20	P30
Max Acceleration Magnitude (m/s^2)	24.2	32.9	40.1	47.8

Table 5.10: Oscillator Acceleration of Experimental Step Response for Active Vibration

Control System Summary

As listed in Table 5.9 and Table 5.10 experiment summary, P15 position controller should be the most suitable controller for this active control system. The system response to the step input is 2.3% of motor position overshoot and 32.9 m/sec^2 of maximum oscillator acceleration.

The experimental result agrees with the simulated result that setting motor positioning bandwidth below the oscillator resonant frequency ensures system stability. It should be noted that for demonstration purpose, this particular flexible oscillator is used to ensure that the oscillator vibrations can be easily identified. The oscillator has a low resonant frequency at 8 Hz which greatly limits the motor positioning bandwidth. In practice, the machine tool is much stiffer, corresponded to a higher resonant frequency, than the flexible oscillator in this experimental setup. Thus, a much higher motor positioning bandwidth is achievable in the actual machine.

In Figure 5.29, the highlighted component is the phase compensator gain. When the gain is set to zero, the active vibration control is disabled. The system performance with and without active vibration control are compared. The motor position and oscillator acceleration step input response are shown in Figure 5.30 and Figure 5.31, respectively. Experimental result has verified with the simulation that the active control system increases the motor position overshoot compared to the system without active control. The oscillator acceleration response in the active control system reaches steady state after half free oscillation cycle and the maximum oscillator acceleration is also reduced. Note that the first oscillation cycle captured at the oscillator acceleration measurement is due to the acceleration and deceleration of positioning the motor. Thus, the oscillator also experiences a similar magnitude of acceleration and deceleration. In comparison, for the system without active control, denoted as the non active control system, the oscillator continues to vibrate even after the motor position reaches steady state. The control input comparison shown in Figure 5.32 indicates that the active control system requires a higher control input to control the motor position since the motor needs to suppress the vibrations on the oscillator at the same time.
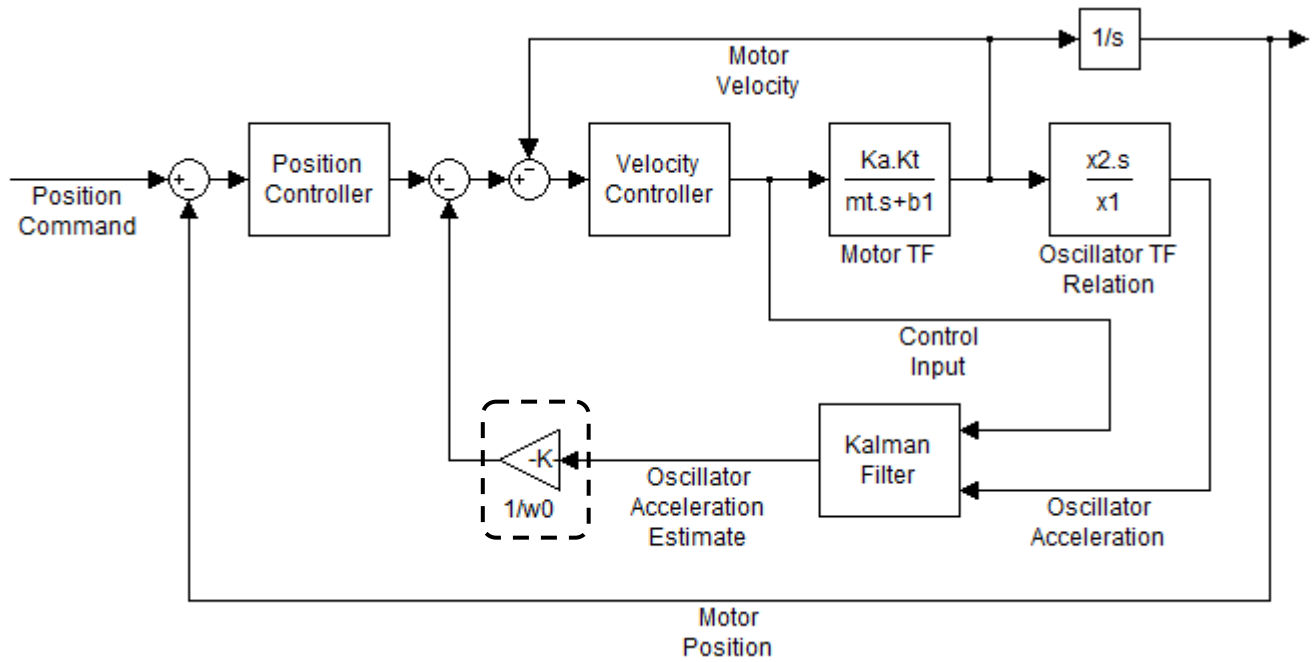
Figure 5.29: Position Loop for Active Vibration Control System

Phase Compensator Gain (Dash)

Figure 5.30: Motor Position of Experimental Step Response for Active and Non Active

Vibration Control System

Input: Motor Position Step Input Command

Output: Motor Position

Position Controller P15	Active Control	Non Active Control
Overshoot (%)	2.3	1.5

Table 5.11: Motor Position of Experimental Step Response for Active and Non Active

Vibration Control System Summary

Figure 5.31: Oscillator Acceleration of Experimental Step Response for Active and Non

Active Vibration Control System

Input: Motor Position Step Input Command

Output: Oscillator Acceleration

Position Controller P15	Active Control	Non Active Control
Max Acceleration Magnitude (m/s^2)	32.9	63.5

Table 5.12: Oscillator Acceleration of Experimental Step Response for Active and Non
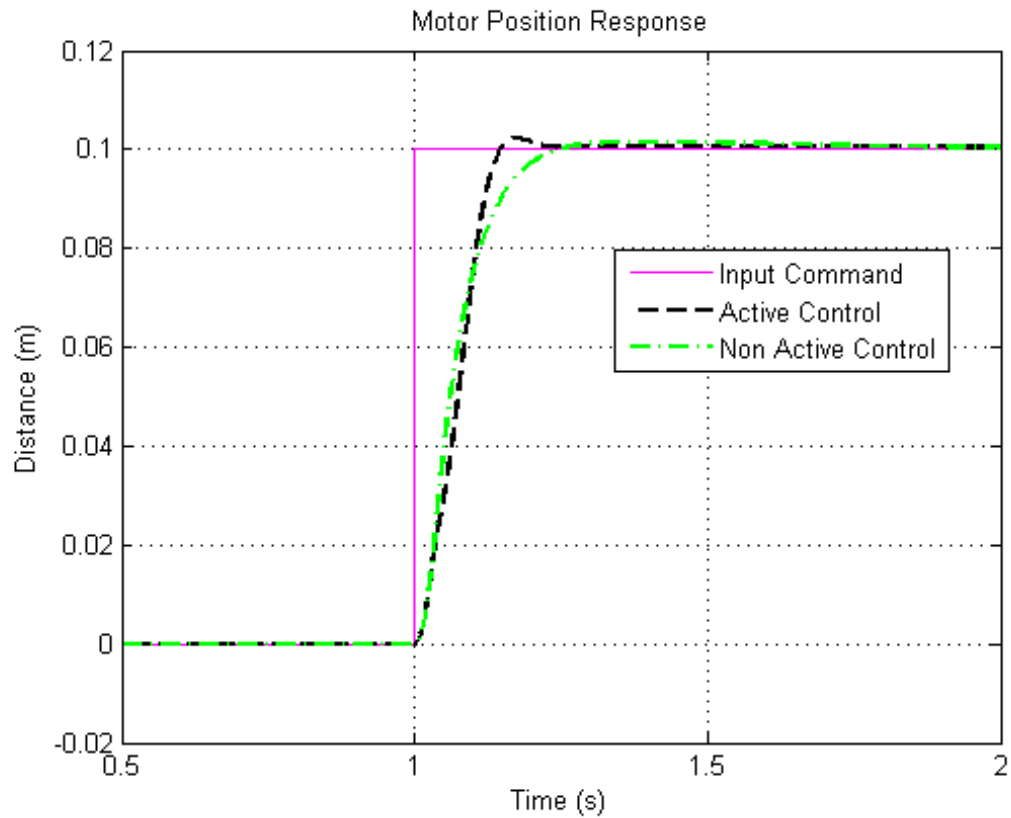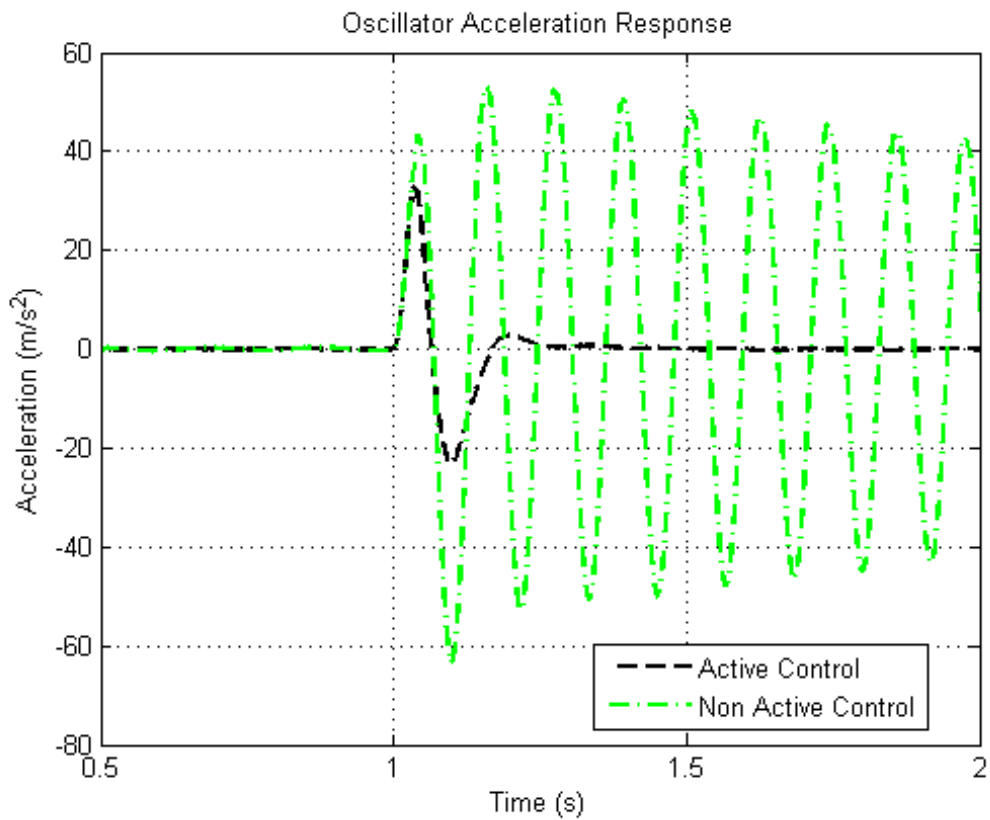
Active Vibration Control System Summary
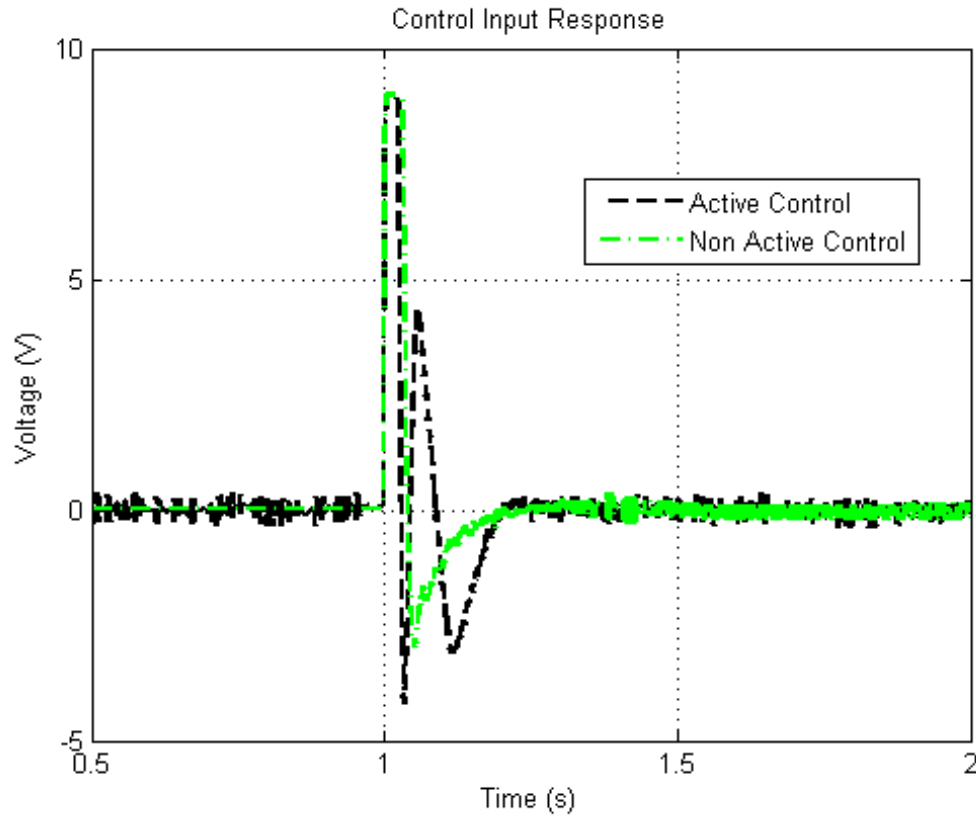
Figure 5.32: Control Input of Experimental Step Response for Active and Non Active

Vibration Control

Input: Motor Position Step Input Command

Output: Control Input

5.3.4.3 Disturbance Rejection Experiment

The intent of the disturbance rejection experiment is to replicate the vibrations at the machine flexible structure when it comes in contact with a workpiece during operation. The disturbance rejection performance is conducted to compare the capacity of the active and non active control system to withstand external disturbance. Exogenous disturbance force is applied at the oscillator by tapping the tip of the oscillator. The active and non active control system response of the motor position response, oscillator

acceleration response and control input are captured and compared as shown in Figure 5.33, Figure 5.34 and Figure 5.35, respectively.

Figure 5.33: Motor Position of Experimental Disturbance Rejection Response for Active and Non Active Vibration Control

Input: Exogenous Disturbance Force

Output: Motor Position

The active control system has small back and forth translation as a compensational effort to reduce the oscillator vibrations. In comparison, the non active control system remains stationary, such that no compensational control effort is available.

Figure 5.34: Oscillator Acceleration of Experimental Disturbance Rejection Response for Active and Non Active Vibration Control

Input: Exogenous Disturbance Force

Output: Oscillator Acceleration

At Figure 5.34, the initial negative oscillator acceleration spike is due to the exogenous disturbance force applied at the oscillator tip. Even though the disturbance applied to the active vibration control system is higher than the non active vibration control system, the oscillator vibrations in the active control system have been suppressed immediately. The oscillator vibrations at the non active control system continue for a much longer time.

The comparison between the two system control inputs is shown in Figure 5.35. There is no control input going into the non active control system. The non active control system

is not aware of the vibration at the oscillator because no accelerometer signal is fed back into the control loop. Since there is some noise in the accelerometer feedback signal which gets amplified through the controller, the active control system voltage input does not reach zero even at steady state.
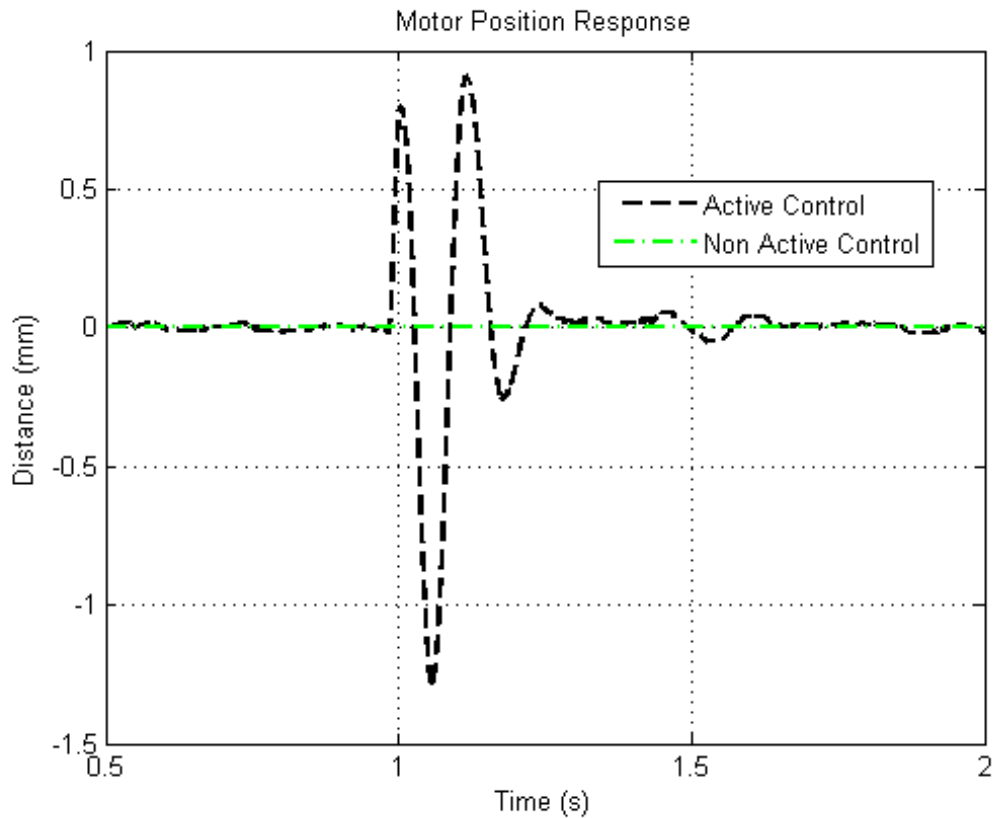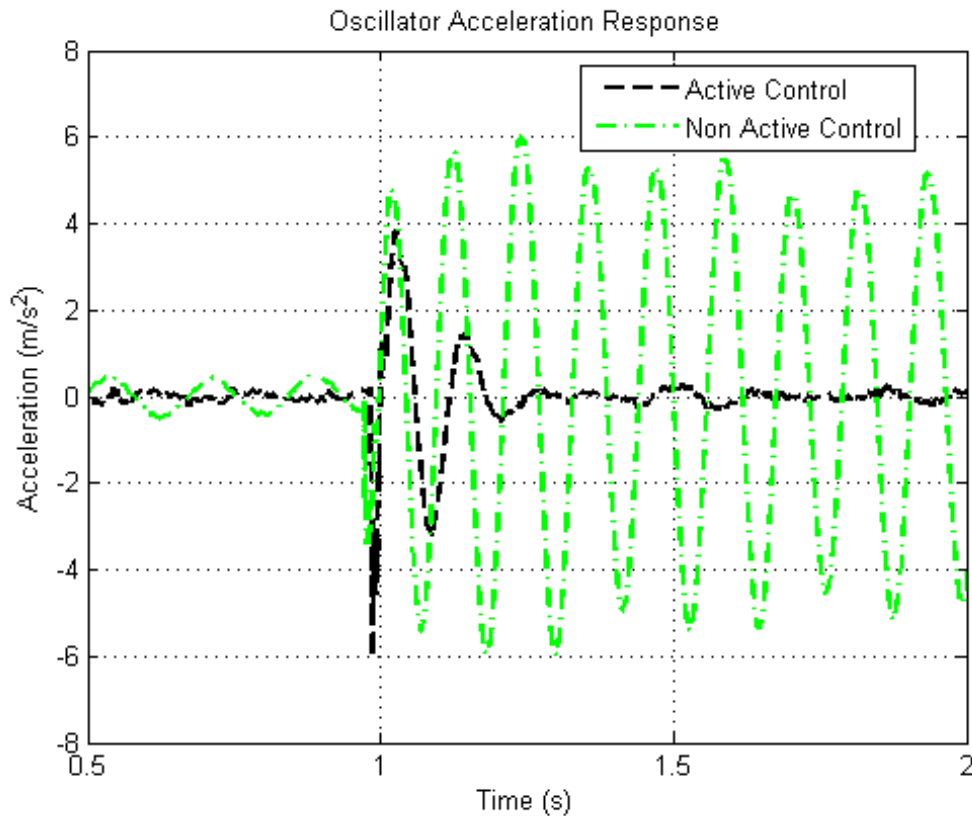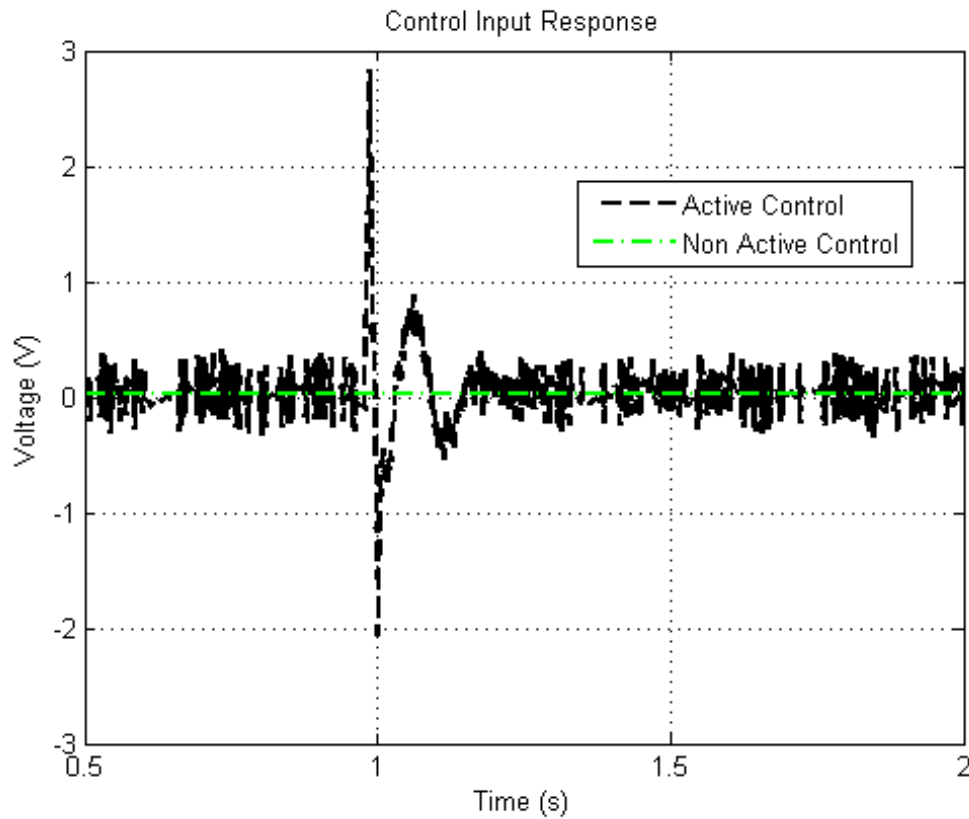

Figure 5.35: Control Input of Experimental Disturbance Rejection Response for Active and Non Active Vibration Control

Input: Exogenous Disturbance Force

Output: Control Input

5.3.4.4 Position Input Command Frequency Response Experiment

The comparison is made between the simulated and experimental result with position input command frequency responses for the system with and without active control. The experiment is conducted by taking a sine sweep experiment from 1 Hz to 35 Hz, and the motor position and oscillator acceleration frequency responses are captured. As shown in Figure 5.36, Figure 5.37, Figure 5.38 and Figure 5.39, the simulated result matches well against the experimental result up until the higher frequency range above 20 Hz. The reason for this frequency response mismatch is due to the unmodelled system dynamics at the higher frequency.

The experimental result shows that the implemented active control system limits motor positioning bandwidth up to the oscillator resonant frequency region as shown in Figure 5.40, and reduces the oscillator acceleration magnitude from 80 dB to 60 dB at resonant frequency as shown in Figure 5.41.

Position Controller P15	Active Control	Non Active Control
Bandwidth (Hz)	3.6	2.5

Table 5.13: Frequency Response from Motor Position Input Command to Motor Position for Active and Non Active Vibration Control System Summary

Figure 5.36: Experimental and Simulated Frequency Response from Motor Position

Input Command to Motor Position for Non Active Vibration Control System

Figure 5.37: Experimental and Simulated Frequency Response from Motor Position

Input Command to Oscillator Acceleration for Non Active Vibration Control System

Figure 5.38: Experimental and Simulated Frequency Response from Motor Position

Input Command to Motor Position for Active Vibration Control System

Figure 5.39: Experimental and Simulated Frequency Response from Motor Position

Input Command to Oscillator Acceleration for Active Vibration Control System

Figure 5.40: Experimental Frequency Response from Motor Position Input Command to Motor Position for Active and Non Active Vibration Control System
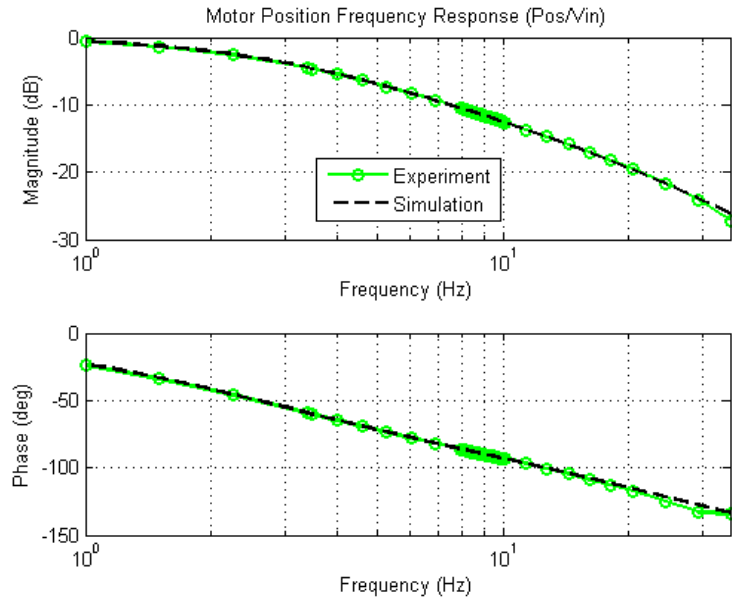

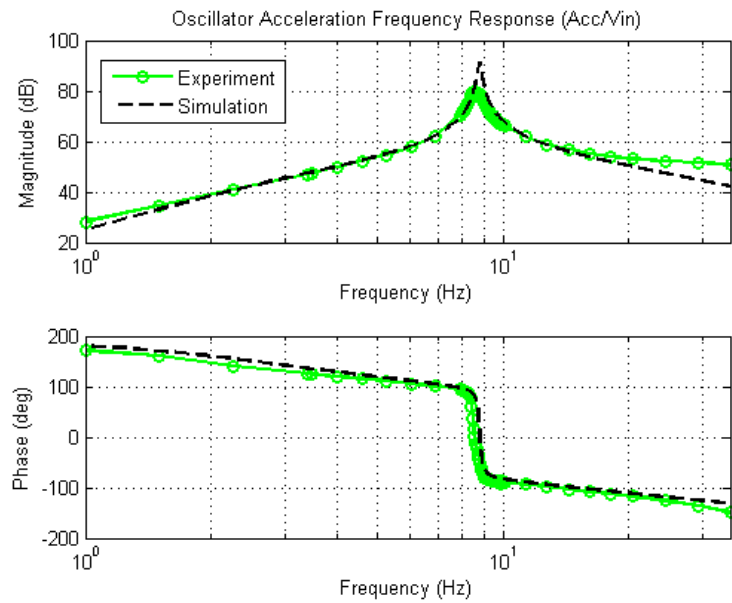
Figure 5.41: Experimental Frequency Response from Motor Position Input Command to Oscillator Acceleration for Active and Non Active Vibration Control System
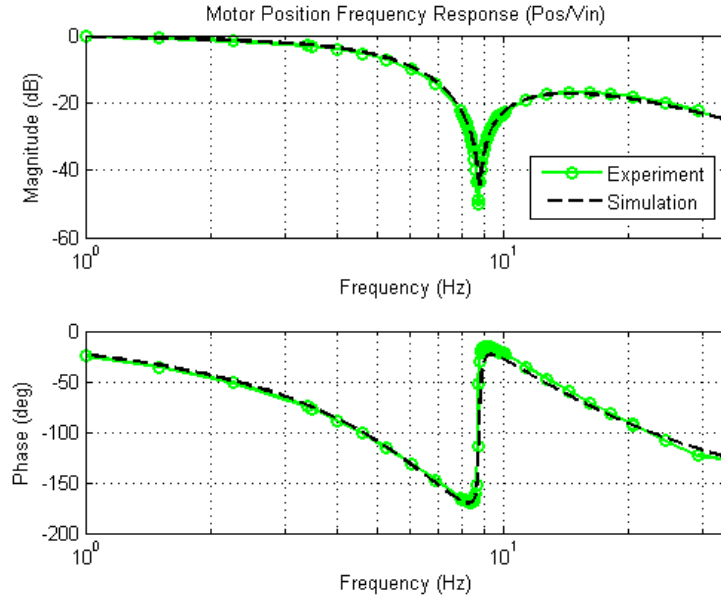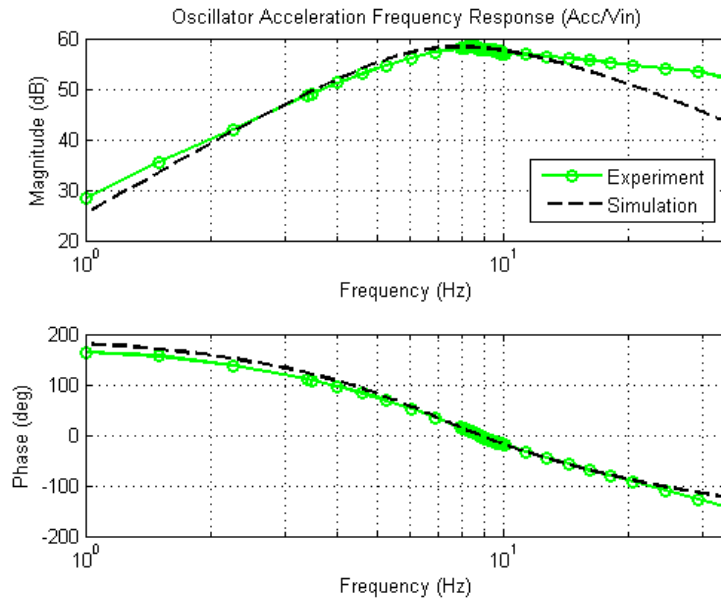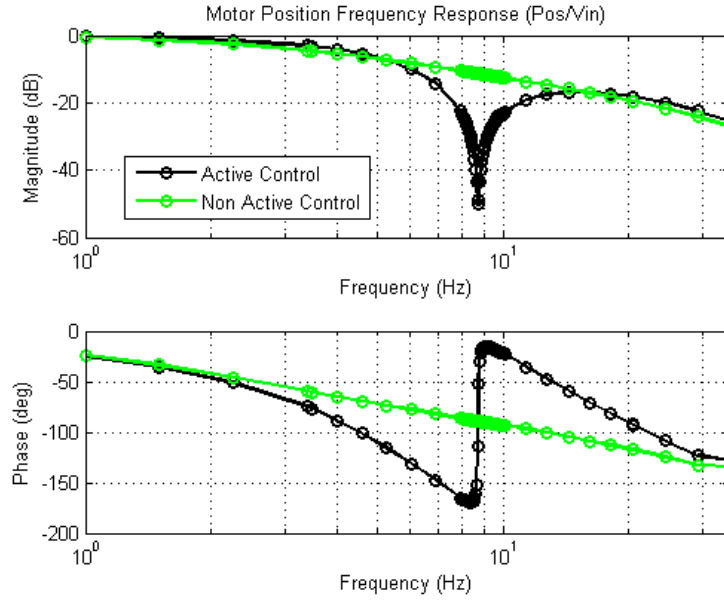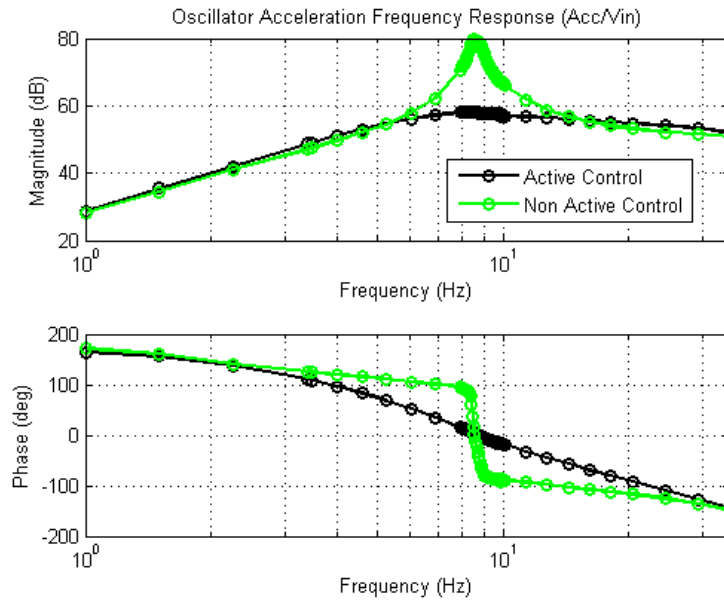
5.3.4.5 Disturbance Frequency Response Experiment

The simulated and experimental disturbance to output frequency responses at the motor position and oscillator acceleration are captured and compared. The external impact force disturbance is applied at flexible oscillator with an impact force hammer. The impact force and time responses of motor position and oscillator acceleration are measured and processed through the fast Fourier transform algorithm to obtain the system disturbance frequency responses. Simulated and Experimental results for the system without active control system are compared and shown in Figure 5.42 and Figure 5.43. Since the simulated result is based on the assumption that the motor position is not affected by the excitation at the oscillator, the simulated motor position disturbance frequency response is at zero magnitude. For this reason, the simulated motor position disturbance frequency response does not appear on the logarithmic scale magnitude graph in Figure 5.42. For the system with active control disturbance, the simulated and experimental frequency responses are compared and shown in Figure 5.44 and Figure 5.45. The system with and without active control disturbance frequency responses experimental comparisons are shown in Figure 5.46 and Figure 5.47. In Figure 5.46, the active control system motor position shows a higher motor position magnitude response than the non active control system because the active control system provides compensational effort driving the motor to suppress the vibrations induced by the disturbance force. In Figure 5.47, the oscillator acceleration disturbance frequency response has been suppressed with the active control system from 70 dB to 40 dB at resonance frequency.

It should be noted that the oscillator acceleration is measured with an accelerometer, which the measured signal is noisy and has a DC offset. This drawback becomes an issue because the poor measured signal remains as the predominated signal in the lower frequency range for below 5 Hz. Therefore, the experimental result captured at the low frequency range is unreliable and deviates from the simulated result. Nonetheless the experimental results show a strong agreement with the simulated results in the higher frequency range.

Figure 5.42: Experimental Frequency Response from Disturbance Force at the Oscillator to Motor Position for Non Active Control System

Figure 5.43: Experimental and Simulated Frequency Response from Disturbance Force at the Oscillator to Oscillator Acceleration for Non Active Vibration Control System

Figure 5.44: Experimental and Simulated Frequency Response from Disturbance Force at the Oscillator to Motor Position for Active Vibration Control System

Figure 5.45: Experimental and Simulated Frequency Response from Disturbance Force at the Oscillator to Oscillator Acceleration for Active Vibration Control System
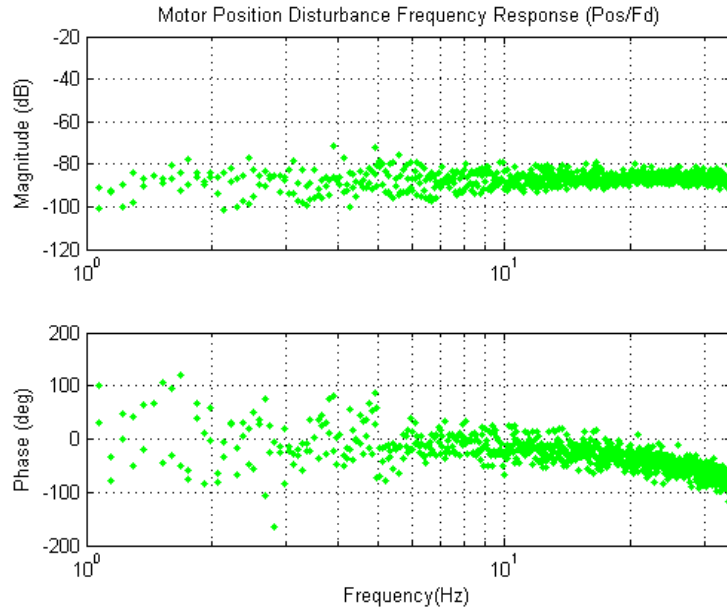
Figure 5.46: Experimental Frequency Response from Disturbance Force at the Oscillator
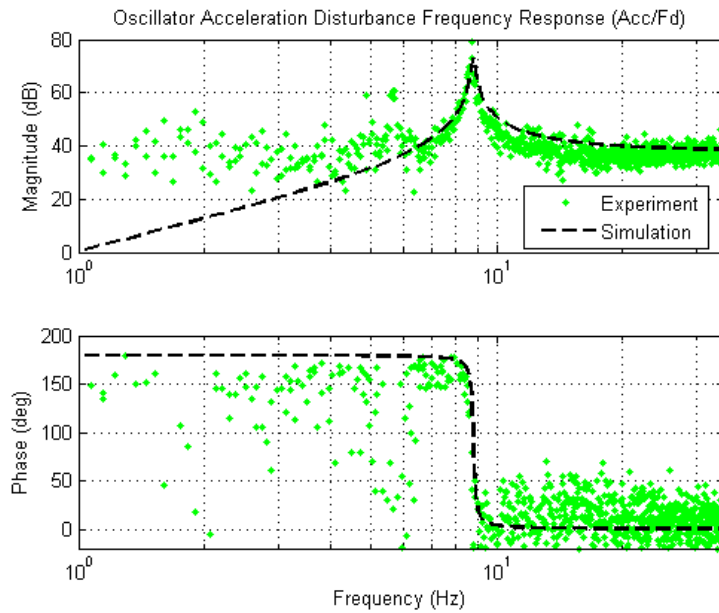to Motor Position for Active and Non Active Vibration Control System

Figure 5.47: Experimental Frequency Response from Disturbance Force at the Oscillator
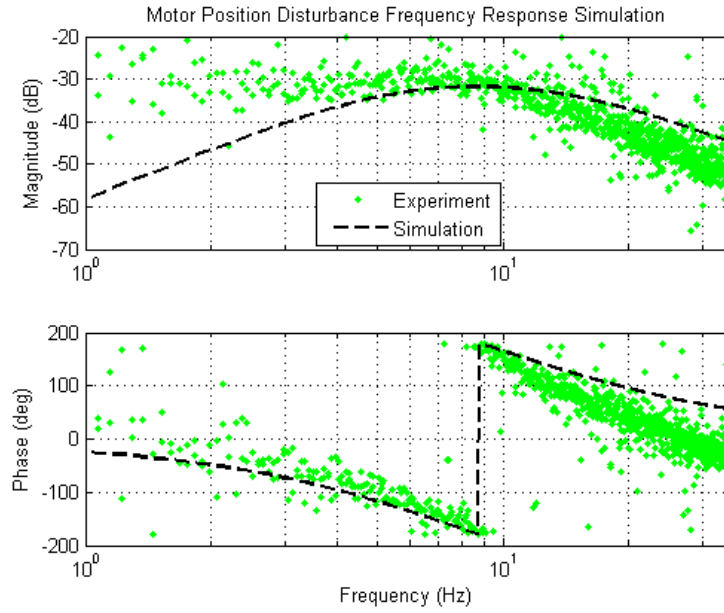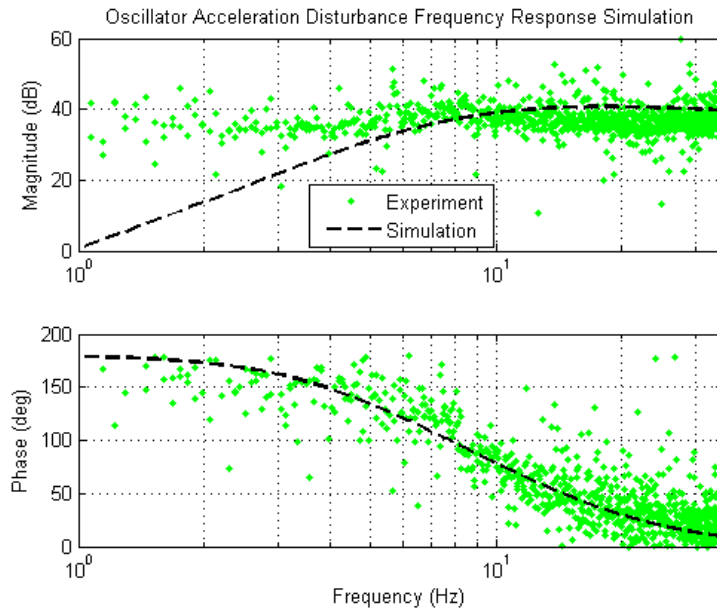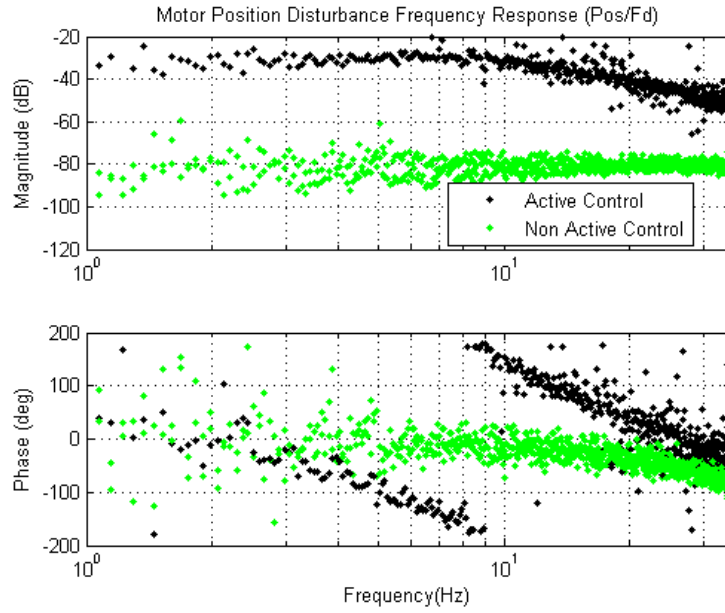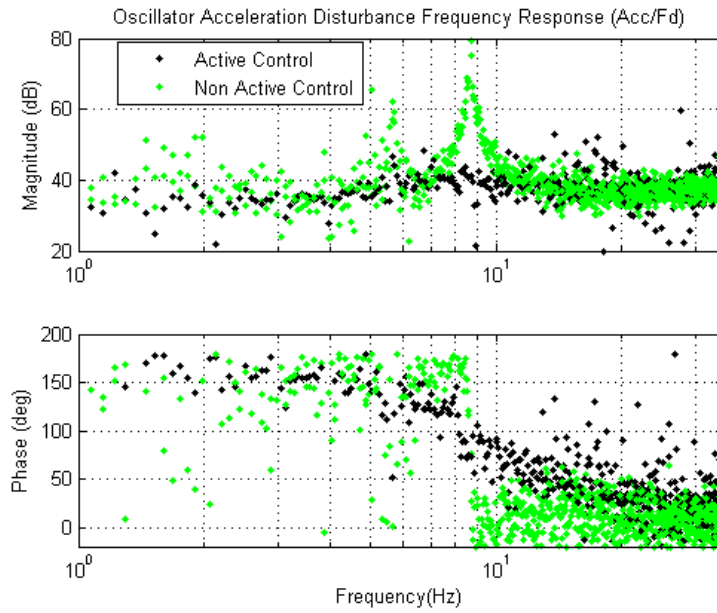to Oscillator Acceleration for Active and Non Active Vibration Control System

5.4   Summary

In this chapter, the positioning and active vibration controller implementation strategies are presented. In Section 5.2, the state space pole placement controller with integrator and the observer design are discussed. Simulations and experiments have been conducted to validate the system performance. The presented pole placement controller design approach does not consider the effect of disturbance. When the disturbance effects, such as Coulomb friction and noise, are included, the control system can no longer perform as expected. Therefore, neither the simulated nor experimental result achieves the desired system performance. The modelling uncertainty is the main reason that the simulated result differs from the experimental result. Through simulations and experiments, the rigid body feed drive control approach possesses a major drawback in ensuring an accurate positioning of the SDOF oscillator because vibration control on the SDOF oscillator is not possible.

In Section 5.3, the active vibration controller is implemented. It is designed for suppressing the SDOF oscillator vibrations at the feed drive. This active controller works in a cascaded structure which includes the velocity loop and position loop. In the velocity loop, a phase compensator is used to compensate the phase delay of the oscillator at resonant which effectively increases the damping of the oscillator. Two implementation modifications are proposed for this active vibration controller for this experimental setup. The first modification is the simplification at the phase compensator to minimize the drift effect at the feedback signal. The second modification is the use of a Kalman filter to improve the sensor measurement accuracy and reduce the measurement noise.

In Section 5.3.4, experimental and simulated result are presented and compared to validate the active vibration control performance. A trade-off between oscillator vibration suppression and motor positioning control performance is required. For a higher motor positioning bandwidth, the oscillator vibration suppression performance is reduced. The active vibration control system is capable of rejecting exogenous

disturbance at the oscillator while the non active vibration control system is sensitive to such disturbance as shown experimentally. The implemented active vibration control system reduces the oscillator acceleration by 20 dB and 30 dB at resonant compared to the system without active vibration control for input command frequency response and disturbance frequency response, respectively. For this experimental setup, the motor positioning bandwidth is relatively low because it is limited by the natural frequency of the flexible structure. In practice, the system is capable of achieving higher motor positioning bandwidths since the natural frequency of the flexible structure should be much higher.

Chapter 6.   Conclusion

6.1   Summary

Vibrations reduce the positioning accuracy of machine tools; hence, their suppression by active control methods is important. In this thesis, a classical control method for active damping of machine tool drive is demonstrated on a high speed linear drive system.

This thesis has presented the detail work of system modelling, system identification and active vibration controller design implementation. In system modelling, a theoretical model of a two degree of freedom system is used to model the flexible feed drive system. Different experimental identification methods are applied to find a suitable identified model for controller design.

A pole placement position controller with integrator and observer are designed for a rigid feed drive. The presented pole placement controller has not considered the system disturbance in the design process. Thus, the experimental and simulated result validate that this positioning controller is unable to achieve the desired performance when there is disturbance presented in the system. Moreover, this type of positioning controller for rigid feed drive design approach does not have any control measure to minimize the flexible structure vibrations. It is shown experimentally that the flexible structure vibration continues even after the motor position reaches steady state.

An active vibration damping controller is implemented using a phase compensation approach. The position tracking and disturbance rejection performance of the controllers are investigated through simulations and experiments. The results indicate that there is a trade-off between active vibration control and high positioning bandwidth. The achievable positioning bandwidth of the active vibration control system is limited by the flexible structure natural frequency. This is because when the flexible structure dynamics becomes a part of the control system, the flexible structure dynamics introduces an anti-resonant effect at the motor position frequency response.

To have the active controller implemented on the experimental setup for this research, design modifications are made to improve the sensor signal. This requires the use of

Kalman filter in the control system, which it has significantly enhanced the quality of accelerometer measurement for the flexible structure vibration.

6.2   Future Work

Vibration control is an active research field in terms of both theoretical problems and practical implementation challenges. In the future, this work can be extended in the following directions for further improvements in active damping:

- Introduce a more detailed system model which includes an accurate model of the friction force.
- Extend the active vibration control to a multimode flexible drive system.
- Use gain scheduled active vibration control to compensate for the changes in the natural frequency of the flexible drive systems.
- Implement the same active vibration control strategy to an indirect drive system and investigate the performance.
- Develop new algorithms to extend the system bandwidth beyond the resonance mode.

Bibliography

[1] Altintas, Y., 2000, "Manufacturing Automation," Cambridge University Press.

[2] Erkorkmaz, K., and Altintas, Y., 2000, "High Speed CNC System Design. Part II: Modelling and Identification of Feed Drives," International Journal of Machine Tools & Manufacture 41 (2001), page 1487-1509.

[3] Mancini, R., 2002, "Op Amps For Everyone," Advanced Analog Products Design Reference, SLOD006B, Texas Instrument.

[4] Alexander, C., and Sadiku, M., 2004, "Fundamentals of Electric Circuits," Mc Graw Hill.

[5] Lampaert, V., Al-Bender, F., and Swevers, J., 2003, "A Generalized Maxwell-Slip Friction Model appropriate for Control Purposes," Proceeding PHYSCON 03 Proceedings of the 2003 International Conference on Physics and Control – Volume 4, pages 1170-1177.

[6] Symen, W., Van Brussel, H., and Swevens, J., 2004, "Gain-scheduling control of machine tools with varying structural flexibility," CIRP Annuals – Manufacturing Technology Volume 53, Issue 1, pages 321-324.

[7] Nise, N. S., 2004, "Control Systems Engineering," John Wiley & Sons, Inc.

[8] de Silva, C. W., 2005, "Mechatronics An Integrated Approach," CRC Press.

[9] Al-Bender, F., Lampaert, V., and Swevers, J., 2005, "The Generalized Maxwell-Slip Model: A Novel Model Friction simulation and Compensation," IEEE Transactions on Automatic Control, Volume 50, No. 11, pages 1883-1887.

[10] Verscheure, D., Paijmans, B., Van Brussel, H., and Swevers, J., 2006, "Vibration and Motion Control Design and Trade-off for High-performance Mechatronic Systems," Proceedings of the 2006 IEEE International Conference on Control Applications, pages 115-1120.

[11] Li, H. Z., Gong, Z., Lin, W., and Lippa. T., 2006, "A New Motion Control Approach for Jerk and Transient Vibration Suppression," Industrial Informatics, 2006 IEEE International Conference, page 676-681.

[12] Welch, G., and Bishop, G., 2006, "An Introduction to the Kalman Filter," UNC-Chapel Hill, TR 95-041.

[13] Simon, D., 2006, "Optimal State Estimator: Kalman, H Infinity, and Nonlinear Approaches," Wiley-Interscience.

[14] Sepasi, M., 2007, "Fault Monitoring in Hydraulic Systems using Unscented Kalman Filter," Master of Applied Science Thesis, CEL, UBC.

[15] Kataoka, H., Tungpataratanawong, S., Ohishi, K., Katsura, S., and Miyazaki, T., 2007, "Motion Control of Industrial Robot Using New Notch Filtering System for Vibration Suppression and Little Phase Error," Mechatronics, ICM2007 4th IEEE International Conference, page 1-6.

[16] Kataoka, H., Ohishi, K., Miyazaki, T., Katsura, S., and Takuma, H., 2008, "Motion Control Strategy of Industrial Robot for Vibration Suppression and Little Positioning Phase Error," Advanced Motion Control, 2008 10th IEEE International Workshop.

[17] Mahmood, I., A., Reza Moheimani, S., O., and Bhikkaji, B., 2008, "Precise Tip Positioning of a Flexible manipulator Using Resonant Control," IEEE/ASME Transcations on Mechantronics, Volume 13, No.2.

[18] Huang, L., Qu, D., and Xu, F., 2010, "Motion Control Strategy of Industrial Direct Drive Robot for Vibration Suppression," Proceedings of the 8th World Congress on Intelligent Control and Automation, page 2430-2433.

[19] Dietmair, A., and Verl, A., 2009, "Drive Based Vibration Reduction for Production Machines," Modern Machinery Science Journal, page 130-134.

[20] Khalil, I. S. M., and Sabanovic, A., 2010, "Action Reaction based Motion and Vibration Control of Multi-degree-of Freedom Flexible Systems," The 11th IEEE International Workshop on Advanced Motion Control, page 577-582.

[21] Naemi, A., 2010, "Instrumentation and Integration of Siemens Linear Motor and SIMODRIVE 611U Module," Master of Engineering Project Report, MAL, UBC.

Appendix A. Calculations

A.1   Unbiased Least Square

The detail derivation of the unbiased least square (ULS) is presented in this section.

$$x_1 = \frac{K_t \cdot K_a \cdot V_{in} - \mu_k}{m_t \cdot s^2 + b_1 \cdot s} \tag{A.1}$$

$$\mu_k = K_t \cdot K_a \cdot d_f \tag{A.2}$$

$$x_1 = \frac{K_t \cdot K_a}{m_t \cdot s^2 + b_1 \cdot s} \cdot \left(V_{in} - d_f \right) = \frac{K_t \cdot K_a}{m_t \cdot s^2 + b_1 \cdot s} \cdot u \tag{A.3}$$

$$\frac{x_1}{u} = \frac{K_t \cdot K_a}{m_t \cdot s^2 + b_1 \cdot s} \tag{A.4}$$

Then the motor position transfer function can be rewritten as voltage input with disturbance to motor velocity transfer function.

$$G_t(s) = \frac{\dot{x}_1}{u} = \frac{K_t \cdot K_a}{m_t \cdot s + b_1} = \frac{\dfrac{K_t \cdot K_a}{m_t}}{s + \dfrac{b_1}{m_t}} = \frac{K_v}{s + (-P_v)} \tag{A.5}$$

Discretise the transfer function by a zero order hold transform.

$$G_t(z) = (1 - z^{-1}) \cdot Z \left[\frac{G_t(s)}{s} \right] \tag{A.6}$$

$$\frac{G_t(s)}{s} = \frac{1}{s} \cdot \frac{K_v}{s + (-P_v)} = \frac{C_1}{s} + \frac{C_2}{s + (-P_v)} \tag{A.7}$$

C_1 and C_2 can be obtained by partial fraction technique.

$$C_1 = \lim_{s \to 0} \frac{1}{s} \cdot \frac{K_v}{s + (-P_v)} \cdot s = \frac{-K_v}{P_v} \tag{A.8}$$

$$C_2 = \lim_{s \to P_v} \frac{1}{s} \cdot \frac{K_v}{s + (-P_v)} \cdot (s + (-P_v)) = \frac{K_v}{P_v} \tag{A.9}$$

Take Z transform of the argument.

$$G_t(z) = (1 - z^{-1}) \cdot Z \left[\frac{-K_v}{P_v \cdot s} + \frac{K_v}{P_v \cdot (s + (-P_v))} \right] \tag{A.10}$$

$$G_t(z) = \frac{K_v}{P_v} \cdot (1 - z^{-1}) \cdot Z \left[\frac{-1}{s} + \frac{1}{s + (-P_v)} \right] \tag{A.11}$$

$$G_t(z) = \frac{K_v}{-P_v} \cdot (1 - z^{-1}) \cdot \left(\frac{1}{1 - z^{-1}} - \frac{1}{1 - e^{P_v \cdot T_s} \cdot z^{-1}} \right) \tag{A.12}$$

$$G_t(z) = \frac{K_v}{-P_v} \cdot \left(\frac{1 - e^{P_v \cdot T_s}}{z - e^{P_v \cdot T_s}} \right) = \frac{K_{vd}}{z - P_{vd}} \tag{A.13}$$

$$K_{vd} = \frac{K_v}{-P_v} \cdot (1 - e^{P_v \cdot T_s}) \quad P_{vd} = e^{P_v \cdot T_s}$$

$$\frac{\dot{x}_1(z)}{u(z)} = G_t(z) = \frac{K_{vd}}{z - P_{vd}} \tag{A.14}$$

$$\dot{x}_1(z + 1) = P_{vd}\dot{x}_1(z) + K_{vd} \cdot u(z) \tag{A.15}$$

A.2   State Space Pole Placement Controller Design

The detail calculation of the state space model discretisation is presented in this section. The discretised state space model is used in the pole placement controller. Eq.(A.16) allows computing the state vector at time t given the state vector at the starting t_0 and the control input signal between t_0 and t. The first term of the equation is the homogenous solution and the second term is the particular solution.

For the discrete equivalent of the continuous state space model, it finds the state vector at the next sampling instance given the state vector and input at the current sampling instance. Then t_0 can be represented by $k \cdot T_s$ at current sampling instance and the next sampling instance at T_s seconds later.

$$X(t) = e^{A_s \cdot (t - t_0)} \cdot X(t_0) + \int_{t_0}^{t} e^{A_s \cdot (t - \tau)} \cdot B_s \cdot u(\tau) d\tau \tag{A.16}$$

Since a zero order hold circuit holds the control constant over the entire sampling period, the control input u(tau) and the input matrix B_s can be move out of the integration. Changing integration variables and simplifying the equation, the equation is shown in Eq.(A.17).

$$X(k \cdot T_s + T_s) = e^{A_s \cdot T_s} \cdot X(k \cdot T_s) + \int_{k \cdot T_s}^{k \cdot T_s + T_s} e^{A_s \cdot (k \cdot T_s + T_s - \tau)} \cdot B_s \cdot u(\tau) d\tau \qquad \text{(A.17)}$$

For simplicity, $k \cdot T_s$ is replaced with k.

$$X(k + 1) = e^{A_s \cdot T_s} \cdot X(k) + \int_0^{T_s} e^{A_s \cdot \eta} \, d\eta \cdot B_s \cdot u(k) \qquad \text{(A.18)}$$

$$X(k + 1) = A_z \cdot X(k) + B_z \cdot u(k) \qquad \text{(A.19)}$$

$$A_z = e^{A_s \cdot T_s} = I + A_s \cdot T_s + \frac{(A_s \cdot T_s)^2}{2!} + \frac{(A_s \cdot T_s)^3}{3!} + \cdots \qquad \text{(A.20)}$$

$$A_z = I + A_s \cdot T_s \cdot \Psi \qquad \text{(A.21)}$$

$$\Psi = I + \frac{(A_s \cdot T_s)}{2!} + \frac{(A_s \cdot T_s)^2}{3!} + \frac{(A_s \cdot T_s)^3}{4!} + \cdots \qquad \text{(A.22)}$$

$$B_z = \int_0^{T_s} e^{A_s \cdot \eta} \, d\eta \cdot B_s \qquad \text{(A.23)}$$

$$B_z = \int_0^{T_s} e^{A_s \cdot \eta} \, d\eta \cdot B_s = A_s^{-1} \cdot (A_z - I) \cdot B_s = T_s \cdot \Psi \cdot B_s \qquad \text{(A.24)}$$

Then apply Eq.(A.20) and Eq.(A.24) to obtain the motor drive discrete equivalent state space model, which includes the motor dynamics and output equation as shown in Eq.(A.25) and Eq.(A.26), respectively.

$$X_1(k+1) = A_{1z} \cdot X_1(k) + B_{1z} \cdot u(k) \qquad \text{(A.25)}$$

$$y(k) = C_{1z} \cdot X_1(k) \qquad \text{(A.26)}$$

$$\Psi = I + \frac{(A_{1s} \cdot T_s)}{2!} + \frac{(A_{1s} \cdot T_s)^2}{3!} + \frac{(A_{1s} \cdot T_s)^3}{4!} + \cdots \qquad \text{(A.27)}$$

$$A_{1z} = I + A_{1s} \cdot T_s \cdot \Psi_1 \qquad \text{(A.28)}$$

$$B_{1z} = T_s \cdot \Psi_1 \cdot B_{1s} \qquad \text{(A.29)}$$

$$C_{1z} = C_{1s} \qquad \text{(A.30)}$$

$$D_{1z} = D_{1s} = 0 \qquad \text{(A.31)}$$

120

A.3   State Space Pole Placement Controller with Integrator Design

From Figure 5.4, the close loop system has a zero according to Eq.(A.5).

$$z_i = 1 + \frac{T_s \cdot K_i}{N_r} \tag{A.32}$$

Then the reference gain, N_r, can be calculated as shown in Eq.(A.33).

$$N_r = \frac{T_s \cdot K_i}{z_i - 1} \tag{A.33}$$

A.4   Kalman Filter

The detail calculation of the discretised state space model used for Kalman filter design is presented in this section. Eq.(A.34) is the continuous state space dynamics equation that includes the motor and oscillator dynamics. The first two rows are the same dynamics parameters used in pole placement controller design. The last three rows are addition parameters that describe the oscillator dynamics. Eq.(A.35) is the continuous state space output equation that includes the motor position and oscillator acceleration as output.

$$\dot{X}(t) = A_s \cdot X(t) + B_s \cdot u(t) \tag{A.34}$$

$$y(t) = C_s \cdot X(t) + D_s \cdot u(t) \tag{A.35}$$

$$X(t) = \begin{Bmatrix} \dot{x}_1(t) \\ x_1(t) \\ x'''_2(t) \\ \ddot{x}_2(t) \\ \dot{x}_2(t) \end{Bmatrix} \quad u(t) = V_{in}(t) \quad y(t) = \begin{Bmatrix} x_1(t) \\ \ddot{x}_2(t) \end{Bmatrix}$$

$$A_s = \begin{bmatrix} -\dfrac{b_1}{m_t} & 0 & 0 & 0 & 0 \\ 1 & 0 & 0 & 0 & 0 \\ 0 & 0 & -\dfrac{b_1 \cdot m_a + m_t \cdot b_2}{m_t \cdot m_a} & -\dfrac{b_1 \cdot b_2 + m_t \cdot k_2}{m_t \cdot m_a} & -\dfrac{b_1 \cdot k_2}{m_t \cdot m_a} \\ 0 & 0 & 1 & 0 & 0 \\ 0 & 0 & 0 & 1 & 0 \end{bmatrix}$$

$$B_s = \begin{bmatrix} \dfrac{K_t \cdot K_a}{m_t} \\ 0 \\ \dfrac{K_t \cdot K_a \cdot k_2}{m_t \cdot m_a} \\ 0 \\ 0 \end{bmatrix} \quad C_s = \begin{bmatrix} 0 & 0 & 0 & 0 & 0 \\ 0 & 0 & 0 & 1 & 0 \end{bmatrix} \quad D_s = \begin{bmatrix} 0 & 0 \\ 0 & 0 \end{bmatrix}$$

Same rules from Appendix A.3 are applied to discretise the continuous state space model. Then the discretised state space model with the motor and oscillator dynamics can be obtained.

$$X(k + 1) = A_z \cdot X(k) + B_z \cdot u(k) \tag{A.36}$$

$$y(k) = C_z \cdot X(k) \tag{A.37}$$

$$A_z = I + A_s \cdot T_s \cdot \Psi \tag{A.38}$$

$$B_z = T_s \cdot \Psi \cdot B_s \qquad\qquad (A.39)$$

$$C_z = C_s \qquad\qquad (A.40)$$

$$D_z = D_s = 0 \qquad\qquad (A.41)$$

$$B_z = T_s \cdot \Psi \cdot B_s$$

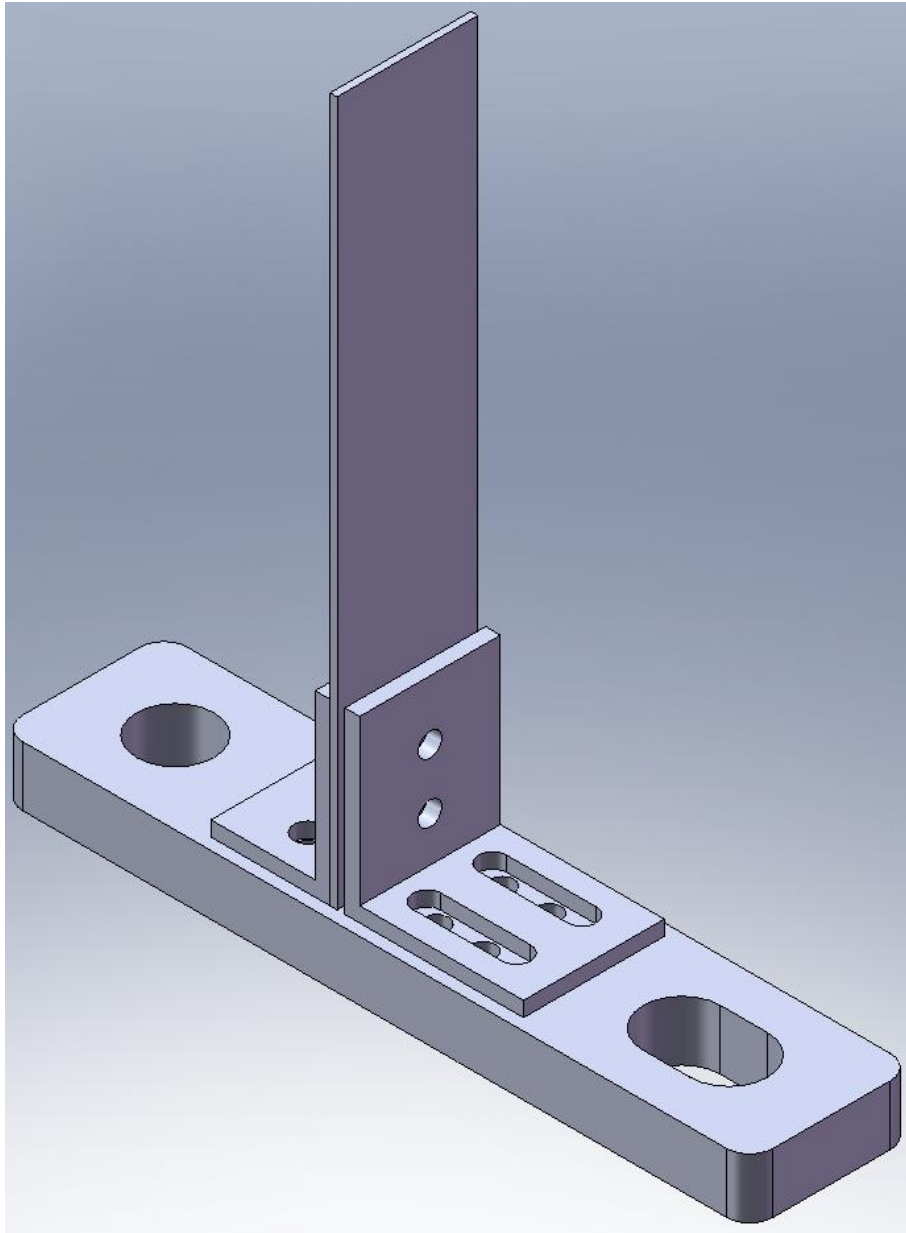# Appendix B. Oscillator Brackets
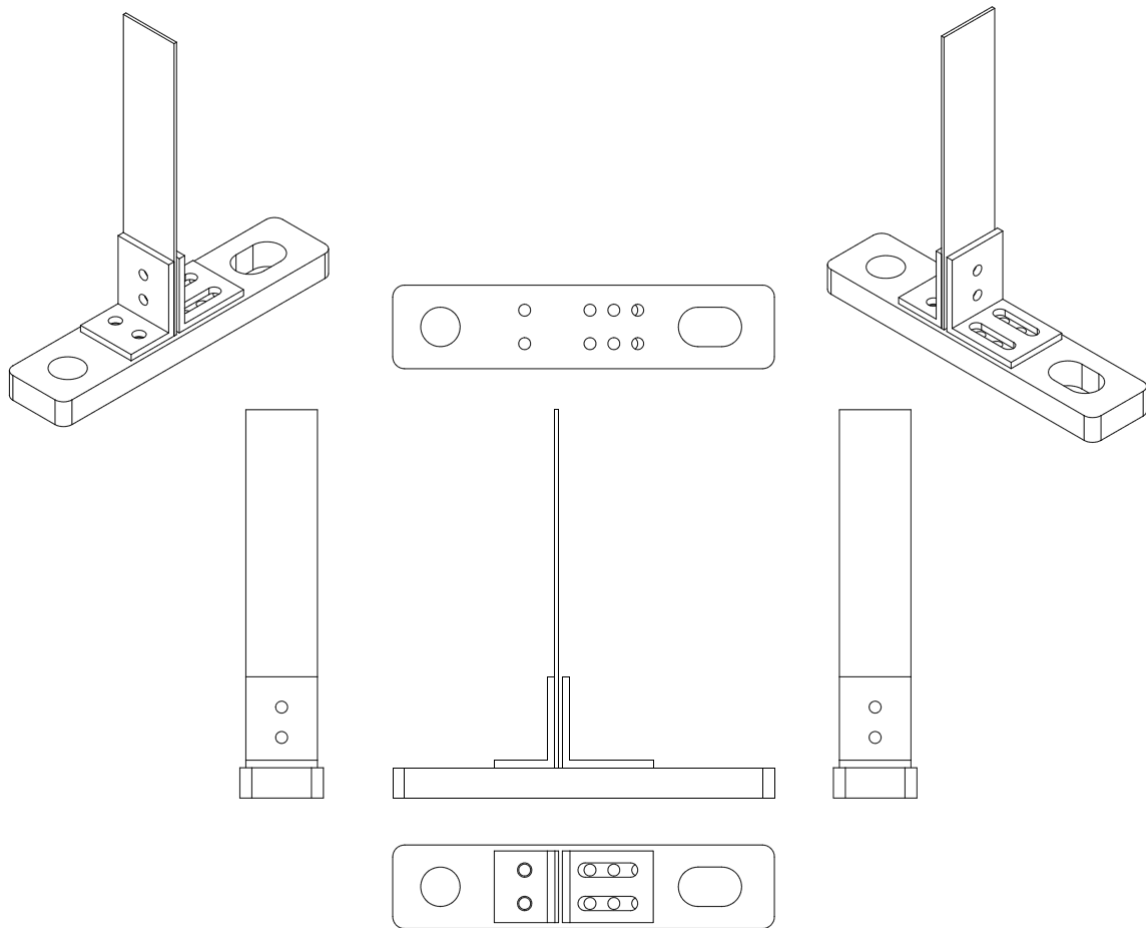

Figure B.1: Oscillator Brackets Model

Figure B.2: Oscillator Brackets Drawing

Note: The flexible bar used in the experiment is longer than as shown in the figure.
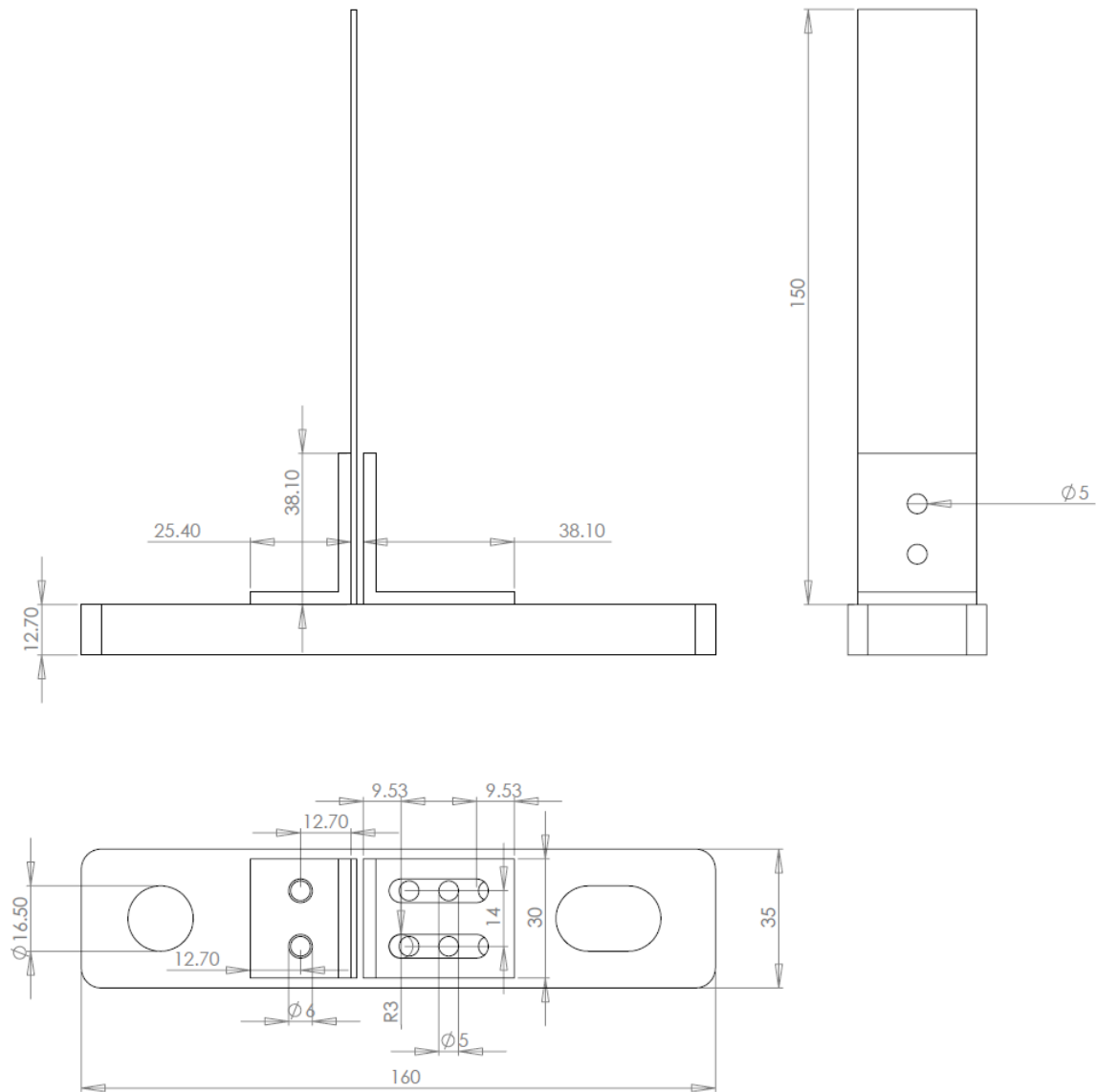
Figure B.3: Oscillator Brackets Measurements

Units: Millimetres (mm)

Note: The flexible bar used in the experiment is longer than as shown in the figure.

Appendix C. System Parameters

The following table presents the parameters applied in the control system.

Proportional Integral (PI) Velocity Controller	
P: 41.8	I: 130.0

Proportional (P) Position Controller
P: 15

Compensator Gain
$\omega_0 = 55.2 \, rad/sec$

Motor Position Transfer Function	Oscillator Acceleration Transfer Function
$\dfrac{x_1}{V_{in}} = \dfrac{157.9}{30.7 \cdot s^2 + 156.1 \cdot s}$	$\dfrac{\ddot{x}_2}{V_{in}} = \dfrac{1281.2 \cdot s}{s^3 + 13.1 \cdot s^2 + 3060.6 \cdot s + 36962.1}$

Note: The above oscillator acceleration transfer function does not consider the dynamics coupling between the motor and oscillator. It is obtained by applying the NLS optimization only on the oscillator acceleration frequency response result.